Automating Mammalian Cell Electroporation using Digital Microfluidics

Ziuwin Leung

A Thesis

in

The Department

of

Electrical and Computer Engineering

Presented in Partial Fulfillment of the Requirements

For the Degree of Master of Applied Science (Electrical and Computer Engineering) at

Concordia University

Montreal, Québec, Canada

January 2023

CONCORDIA UNIVERSITY

School of Graduate Studies

This is to certify that the thesis is prepared

By: Ziuwin Leung

Entitled: Automating Mammalian Cell Electroporation using Digital Microfluidics

and submitted in partial fulfilment of the requirements for the degree of

Master of Applied Science (Electrical and Computer Engineering)

complies with the regulations of the University and meets the accepted standards with respect to originality and quality.

Signed by the final Examining Committee:

_____ Internal Examiner
Dr. Nawwaf Kharma

_____ External Examiner
Dr. Deniz Meneksedag Erol

_____ Supervisor
Dr. Steve Shih

Approved by: _____

Dr. M. Zahangir Kabir
Graduate Program Director
Department of Electrical and Computer Engineering

Date_____2023 _____

Dr. Mourad Debbabi. Dean,
Faculty of Engineering and Computer Science

Automating Mammalian Cell Electroporation using Digital Microfluidics

Ziuwin Leung

Master's in Applied Science – Electrical and Computer Engineering

Department of Electrical and Computer Engineering
Concordia University

2023

Abstract

To examine a wide range of unique genetic edits, especially for cellular immunotherapy, techniques for automating mammalian cell engineering is needed while working with cell types that are rare and/or difficult to culture and expand. Herein, we introduce a miniaturized digital microfluidic module for electroporation of minimal number of mammalian cells (~40,000) at a time, potentially allowing for genetic engineering on a scalable and automated platform. The system functions by first merging three droplets together to form a continuous droplet chain. We call this the triDrop structure where the outer droplets contain high conductive liquids which are in contact with gold electrodes, while the middle droplet consists of low conductivity liquid containing the cells and target delivery molecule. This effectively creates a liquid cuvette where by applying a voltage, an effective electric field is generated within the triDrop structure with field focusing across the middle droplet. This allows for transient pore formation and insertion

of biological payloads into cells without compromising long-term health by isolating cells from harmful electroporation effects. We show the proof-of-concept by successful delivery of a range of biological payloads (plasmid, mRNA, and Cas9 RNP) into adherent and suspension cells, including primary T cells. The flexibility and versatility of the triDrop, a digital microfluidic (DMF) electroporation module, suggests that our platform can be integrated with other DMF devices to allow for end-to-end automation of mammalian cell engineering. Additionally, this platform can potentially be used for the automation of large-scale genetic screens while using a single patient sample and low cell and reagent consumption.

"This thesis is dedicated to my grandfather, a constant inspiration with his persistent thirst for learning and challenging the status quo"

Acknowledgements

I would like to express my deepest appreciation to all those who have supported me during the research and writing of this thesis.

First and foremost, I would like to express my deepest gratitude to my research supervisor, Dr. Steve Shih, for agreeing to take me on as a Master's student and for this opportunity to follow my passion, do research, and develop myself as an individual and aspiring researcher. Your invaluable insights, continuous encouragement, and patience throughout my journey have been instrumental in helping me complete this work.

Next, I would like to thank all my friends and research colleagues in our lab for creating a welcoming environment. Their willingness, and eagerness, to guide, brainstorm, and troubleshoot problems played a huge role in getting comfortable in the lab and made understanding complex ideas more straightforward. Working with you guys was a great pleasure for me and I learned a lot. A special thanks to Samuel R. Little for being my lab and brainstorming partner throughout my journey, without whom my project would not be completed at this date. I am truly grateful for the positive and supportive environment you have created that made our time together always fun and exciting since day one. You have been a friend ever since we began to collaborate and hope we will have the opportunity to work even closer together in the future.

I would also like to thank the ECE department for their FRS funding and Natural Sciences and Engineering Research Council (NSERC) for their SynBioApps CREATE program fellowship acceptance. Their funding and support provided the resources needed to complete my research which created a space for me to learn and gain experience. I also thank Angela Quach from the

Genome BioFoundry for her training and continuous support with the flow cytometry machine. I also thank Javier Felipe Perez and Dr. Laurent Potvin-Trottier for their permission and assistance in using their microscope. I would also like to thank Dr. Scott McComb for your insightful advice which has played a big role in the direction of this project, and Dr. Peter Darlington and his students, Mehri Hajiaghayi and Fatemeh Gholizadeh, for their support and expertise in blood handling and primary immune cell isolation. I also thank the Centre for Applied Synthetic Biology for their resources and making the working environment so pleasant, and the Sacher Lab for sharing their tissue culture lab space and accommodating our research needs.

I am also grateful to the members of my committee, Dr. Nawwaf Kharma and Dr. Deniz Meneksedag Erol, for their valuable feedback and suggestions, and for accommodating my thesis.

Finally, I would like to thank all my family and friends. My biggest and sincerest appreciation to my parents for believing in me and inspiring me to follow my dreams. Your unconditional love and unwavering support in my decisions and in anything I undertake have been my biggest source of strength. Also, to my grandparents and brothers, thank you for always being there no matter what. To the rest of my family and friends, thank you for all the memories and support throughout this journey.

This work would not have been possible without the help and support of all of these individuals. I am truly grateful to each and every one of them.

Overview of Chapters

This thesis describes the project I conducted and completed for my Master's in Applied Science in Dr. Steve Shih's research group at Concordia University. In this work, I aimed to develop an electroporation module using the digital microfluidics platform for automating mammalian cell transfection with specific focus on primary immune cells for cellular immunotherapy applications. This thesis provides an introduction to genetic engineering and the different intracellular delivery approaches, a literature review on the microfluidic platform and the different paradigms pros and cons, and finally a commentary on established intracellular delivery microfluidic approaches and its challenges. With special focus on primary human primary T cells transfection, I will then get into the core of my research, stating my thesis objectives and methodology used for the development and validation of the digital microfluidic electroporation module, followed by my results and discussion of the experimental data. Lastly, a conclusion of my overall thesis and future outlook of the project.

Chapter 1 introduces several topics related to the background of my research such as genetic engineering, intracellular delivery techniques, an overview of the microfluidic technology and platform, microfluidic approaches to intracellular delivery, and finally my thesis objectives.

Chapter 2 describes my methodology used in both on the bulk scale and micro-scale side of the biological processes performed and methods for data collection and analysis.

Chapter 3 discusses the experimental data and results from the development of the novel digital microfluidic electroporation module, which we call the triDrop system. First, I will describe the device workflow and validation of the design by numerical simulations, followed by the characterization and optimization of the system for intracellular delivery of target delivery

molecules. As a proof-of-concept, I then describe the triDrop system's ability to deliver a range of biological molecules of different sizes to a range of cell types. Lastly, I demonstrate the successful delivery of biologically relevant payloads into Jurkat cells and human primary T cells showing successful gene knockout, plasmid expression, and post-electroporation viabilities.

Chapter 4 presents a summary and conclusion of my work, the future perspectives for the triDrop system and its application in cellular immunotherapy.

Overview of author contributions

The work presented here was made possible with the help of my colleagues in the Shih Lab and The Clinical Immunology and Molecular Biomarkers Laboratory (CIMBL). Here is a summary of the contributions to my thesis.

The project experimental design was carried out by myself, Samuel R. Little (PhD candidate), and Dr. Steve Shih. The research article relevant to this work was written and edited by myself, Samuel R. Little, and Dr. Steve Shih.

All experiments and data analysis relevant to my thesis were conducted and gathered by myself and Samuel R. Little. The resulting figures were revised and edited by myself, Samuel R. Little, and Dr. Steve Shih.

Biological and microfluidic methods and DMF control software were developed by myself and Samuel R. Little.

Mathematical modeling and simulations were designed and performed by myself.

All device design, fabrication and optimization were conducted by myself and Samuel R. Little.

Electroporation control circuits and software were designed and built by Samuel R. Little.

Fatemeh Gholizadeh, Mehri Hajiaghayi, and Dr. Peter J. Darlington developed the methodology for cell isolation and freezing from fresh blood; Fatemeh Gholizadeh and Mehri Hajiaghayi performed the isolation and freezing protocols with some assistance from myself.

Tissue culture work (cell passaging, maintenance) was performed by myself and Samuel R. Little.

Table of Content

List of Figures

List of Tables

List of Equations

List of Abbreviations

1.	**AC**	Alternating Current
2.	**Au**	Gold
3.	**ANOVA**	Analysis of Variance
4.	**CAD**	Computer Aided Design
5.	**CAR**	Chimeric Antigen Receptor
6.	**CD**	Cluster of Differentiation
7.	**CMV**	Cytomegalovirus
8.	**CO2**	Carbon Dioxide
9.	**Cr**	Chromium
10.	**CRISPR**	Clustered Regularly Interspaced Short Palindromic Repeats
11.	**DAPI**	4′,6-Diamidino-2-Phenylindole
12.	**DC**	Direct Current
13.	**DI**	Distilled
14.	**DMEM**	Dulbecco's Modified Eagle Medium
15.	**DMF**	Digital Microfluidics
16.	**DNA**	Deoxyribonucleic Acid
17.	**EDTA**	Ethylenediaminetetraacetic Acid
18.	**EGFRvIII**	Epidermal Growth Factor Receptor variant 3
19.	**EP**	Electroporation
20.	**EWOD**	Electrowetting On Dielectric
21.	**FACS**	Fluorescence-Activated Cell Sorting
22.	**FBS**	Fetal Bovine Serum
23.	**FC**	Fluorocarbon
24.	**FDA**	Food And Drug Administration
25.	**FITC**	Fluorescein Isothiocyanate
26.	**GFP**	Green Fluorescent Protein
27.	**H_2O**	Water molecule
28.	**HEK293**	Human Embryonic Kidney 293 cells

29. **HEPES** 4-(2-Hydroxyethyl)-1-Piperazineethanesulfonic Acid
30. **HLA** Human Leukocyte Antigen
31. **IL** Interleukin
32. **IPA** Isopropyl Alcohol
33. **iPSC** Induced Pluripotent Stem Cells
34. **ITO** Indium Tin Oxide
35. **IU** International Units
36. **KCl** Potassium chloride
37. **MFI** Mean Fluorescent Intensity
38. **$MgCl_2$** Magnesium chloride
39. **MHC** Major Histocompatibility Complex
40. **PBS** Phosphate Buffered Saline
41. **PCB** Printed Circuit Board
42. **PDMS** Polydimethylsiloxane
43. **PLA** Polylactic Acid
44. **RNA** Ribonucleic Acid
45. **RNP** Ribonucleoprotein
46. **RPMI** Roswell Park Memorial Institute
47. **SEM** Standard Error of Mean
48. **TALEN** Transcription Activator-Like Effector Nucleases
49. **TE** Transfection Efficiency
50. **TIL** Tumor-Infiltrating Lymphocytes
51. **UV** Ultraviolet
52. **V_{DC}** Direct Current Voltage
53. **VR** Viability Ratio
54. **V_{RMS}** Root Mean Square of Applied Voltage
55. **ZFN** Zinc Finger Nuclease

List of co-authored publication

Articles in Preparation for Submission

A tri-droplet liquid structure for high efficiency electroporation of mammalian cells using digital microfluidics

Samuel R. Little*,[1, 2] Ziuwin Leung*,[1, 2] Angela B.V. Quach,[2] Alison Hirukawa,[3] Fatemeh Gholizadeh,[4] Mehri Hajiaghayi,[4] Peter J. Darlington,[4,5] Steve C.C. Shih[1,2,4§]

[1]Department of Electrical and Computer Engineering, Concordia University, Montréal, Québec, Canada
[2]Centre for Applied Synthetic Biology, Concordia University, Montréal, Québec, Canada
[3]DropGenie, Boston, Massachusetts, USA
[4]Department of Biology, Concordia University, Montréal, Québec, Canada
[5]PERFORM Center, Department of Health, Kinesiology and Applied Physiology, Concordia University, Montreal, Québec, Canada

*Both authors contributed equally

[§]Corresponding Author – steve.shih@concordia.ca

Chapter 1 Introduction

In this section, I will introduce genetic engineering and the importance of intracellular delivery, discuss the different established intracellular delivery methods, and a literature review describing the three dominant microfluidic paradigms. Next, I will introduce different microfluidic approaches for intracellular delivery and discuss their challenges, with a special focus on human primary T cell transfection, and, finally, my thesis objectives.

1.1 Genetic engineering and intracellular delivery

Genetic engineering has been a key research tool for modifying the DNA of target organisms and manipulating gene functions. Since its first application in 1973 by Herbert Boyer and Stanley Cohen who successfully inserted DNA from one bacteria into another[1], genetic engineering has impacted various fields across disciplines such as food and agriculture, biomanufacturing, medicine, and biotechnology[2]. This is all achieved by altering cellular functions in a controlled manner through the internalization of specific biological payloads such as DNA, RNA, and proteins. Today, a more recent area of research is the reprogramming of fully matured and differentiated cells which can be achieved by the internalization of pluripotent transcription factors such as Oct4, Sox2, Klf4, and c-Myc into mammalian cells, producing induced Pluripotent Stem Cells (iPSCs). In doing so, iPSCs have paved new ways for treating cancer and degenerative diseases, screening new drugs, and developing diseased models[3,4]. The introduction of Chimeric Antigen Receptors (CAR) transgene into patient T cells to generate CAR-T cells as cellular immunotherapy, which allows for the targeting of cancer cells, has also been an active area of research[5–8]. Its success and effectiveness against haematological malignancies have led to several FDA-approved therapies[9–14]. Although, this has renewed promise to cancer patients, current CAR-T treatment efficacy is not as translatable to solid

tumors as it faces significant challenges and limitations in the design and production of engineered immune cells that still need to be resolved[5–8]. Further research into these limitations could pave way for improved cellular immunotherapies and better patient outcomes. In addition, the internalization of genetic editing tools such as ZFNs, TALENs, and CRISPR/Cas9 systems has enabled scientists to carry out gene knock-in or knock-out experiments, expanding their application in biomedical research and clinical therapies[15–19]. As such, intracellular delivery of biological payloads is a fundamental starting point for biomedical research and novel therapies.

1.2 Intracellular delivery and bulk transfection methods

The intracellular delivery and internalization of biological payloads are essential to effectively manipulate cellular functions for cellular engineering. To achieve this, several transfection methods can be categorized into three main groups illustrated in **Figure 1-1**; (1) biological, (2) chemical, and (3) physical transfection methods.

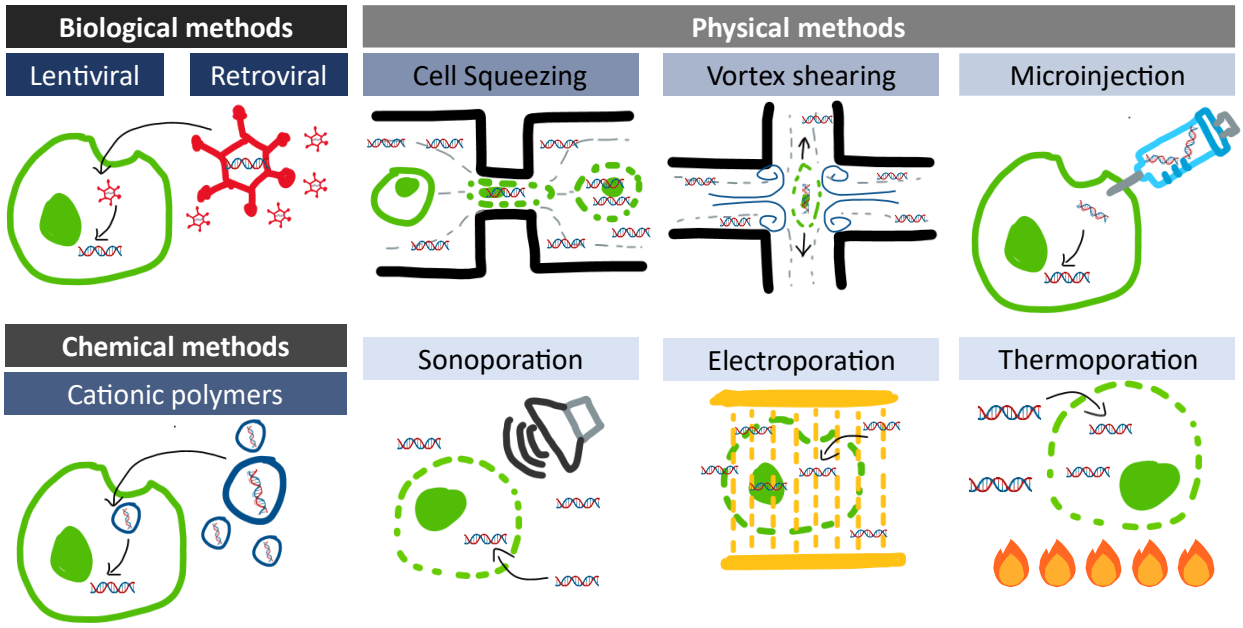

Figure 1-1. Intracellular delivery techniques categorised into three groups; biological, chemical, and physical.

1.2.1 Biological transfection methods

Biological methods are techniques that utilize recombinant viral vectors to deliver DNA or RNA into target cell of interest in a controlled manner by using the natural infection and integration pathways of viruses. This is done by removing the coding regions of the viral genome and replacing them with the gene of interest which either gets integrated into the host genome or expressed transiently through an episomal vector[2]. For example, retroviruses, such as lentivirus are more commonly used for stable transfection, and adenovirus or adeno-associated viruses are more commonly used for the transient expression of genes[20]. This is because adenovirus can only deliver its cargo into the cytoplasm and translocation of DNA into the nucleus is necessary for expression which is a highly selective process[21,22]. Alternatively, DNA can be found in cell nucleus during cell division when nuclear envelope breakdown and reformation occurs, however, expression of DNA delivered via adenovirus to dividing cell lines still remains a challenge. On the other hand, lentivirus can penetrate the nuclear envelope enabling transfection to both dividing and non-dividing cell types which is favorable in some research where stable expression of transgenes is needed. While these methods are effective for DNA delivery, there are several limitations of viral vectors such as its cost, need for extensive labor, and biological safety concerns[23,24]. Additionally, some viral vectors are limited in their ability to in delivering DNA and RNA. For example, lentivirus can deliver DNA and RNA up to a maximum size of 8kb, making large (>8kb) plasmid and protein-based delivery impossible[20,25]. Despite that, lentiviral vectors are the most clinically advanced and widely used method for delivering DNA with several FDA-approved lentiviral generated CAR-T therapies[9–14]. However, viral vectors also have oncogenic potential and immunogenicity concerns which motivate the adoption and advancement of non-viral transfection methods for cellular engineering[24,26–30].

1.2.2 Chemical transfection methods

Similar to viral vectors, the chemical transfection method relies on encapsulating the biological cargo itself to allow for delivery through endocytosis. The encapsulation of payloads is achieved either through cationic lipids or polymers which condense biological payloads into small vesicles. This facilitates attraction of the package to cells, promoting endocytosis, and enabling efficient internalization of particles ranging from 50 to 100nm[2,31]. In addition, these packages also function to protect biological cargo against enzymatic degradation. However, this results in delayed unpacking, delayed expression, and excessive toxicity[32–34]. Chemical transfection methods also lack the ability to deliver payloads into the nucleus and are cargo- and cell-type specific, making it challenging to deliver payloads that are larger than 100nm (ie. 5-10kb uncondensed plasmid[35]). Intracellular delivery is especially difficult against hard-to-transfect cells and non-dividing cell types[36–38]. Despite these shortcomings, chemical transfection methods have proven to be easier to use with more flexibility in the type of biological payload they can deliver and a more cost-effective alternative to viral vectors[39]. For example, Lipofectamine is most commonly used where its delivery package is formed using self-assembling cationic liposomes that encapsulates a range of biological payloads, including CRISPR/Cas9 RNPs[39]. Although chemical transfection methods avoid the use of potentially oncogenic viral vectors, their use in cellular immunotherapy and their transfection efficiency in primary T cells, however, still need improvement[29]. Other forms of chemical transfection reagents include triton X-100[40], digitonin[41], etc[2].

1.2.3 Physical transfection methods

Physical transfection methods rely on applied external forces to compromise the cell membrane integrity resulting in transient pore formation. This transient pore formation in turn allows

payloads to diffuse into cells and, in some cases, actively assist in the delivery itself without extra packaging steps such as used in previously mentioned methods. Unlike biological or chemical transfection methods, physical transfection methods are not limited by their delivery packages and cargo size as they can deliver nearly any cargo to any cell type depending on the size of the transient pores formed. Mechanoporation, sonoporation, hydrodynamic-poration, and microinjection are different types of physical transfection (**Figure 1-1**) methods currently used. Cuvette electroporation is most widely used in laboratories owing to its ease of use[42]. Bio-Rad's cuvette electroporation system has been the most widely used technique for electroporating cells, however, Neon electroporation and Lonza Nucleofector systems are more recent technologies with improved transfection efficiencies, viabilities, and repeatability[43–45]. Nonetheless, finding the balance between opening up the right kind of pores in the plasma membrane to allow for the internalization of biological payloads while avoiding unfavorable irreversible perturbations or membrane damage that results in cell death remains a challenge[2,46,47]. Electroporation requires application of high voltage potentials to achieve the necessary electric fields required for pore formation. When high voltage potentials are applied, several well-known factors[47–53] occur that negatively affect cell health, further described in **Section 1.3.5**. This is particularly unfavourable in the context of electroporating primary cell lines for therapeutic applications, in which cells can suffer from electroporation-induced cell toxicity, low long-term viability and impeded recovery[54–58]. Although electroporation has been used in transfecting various biological payloads into a range of cells including hard-to-transfect cells, such as primary cells and stem cells, it can still cause high cell death[59–61]. Nonetheless, electroporation is still favoured, especially in immune cell engineering, as it proved to be a highly efficient method for delivering payloads, such as Cas9 RNP[18,19]. Physical transfection methods are becoming more of an

attractive tool for cellular engineering as they can deliver nearly any biological payload size into any cell type without any immunogenicity and oncogenic potential.

1.3 Introduction to microfluidics and on-chip transfection

Microfluidics is the science and technology behind the manipulation of small amounts of fluid in a controllable manner. In 1965, Richard Sweet developed a way to controllably generate and charge discrete droplets from a stream of fluid to hit the paper at a specific spot[62–64]. In the following decades, extensive research and advancements in micro- and nano-fabrication techniques, and the synthesis of new materials have pushed the boundaries of microfluidics. Microfluidics technology offers a wide range of advantages over conventional bulk scale technologies. These benefits include (1) reduced consumption of samples and reagents, reducing the overall cost of experiments, (2) whole biological process integration for simplified end-user experience, (3) potentially scalable and automated for high-throughput, multiplexed and highly paralleled assays, (4) faster analyses due to the shorter reactions and/or separation times, (5) accurate measurement and allowing to increase the measurement resolution in given applications[62–64]. Today, microfluidics takes the form of microchannels and electrodes to manipulate small amounts of fluids and perform miniaturized biological analysis and laboratory experiments, earning the term Lab-on-a-chip. Specifically on intracellular delivery, the miniaturization of these previously mentioned transfection methods onto microfluidic devices is particularly appealing to researchers because of the ability to uniformly treat cells, which allows for robust intracellular delivery and improved cell viability outcomes, especially for hard-to-transfect cell lines[2,46,47,65]. In the following sections, I will introduce different types of microfluidic paradigms; channel microfluidics, droplet-in-channel microfluidics, and digital

microfluidics (**Figure 1-2**). Next, I will explore miniaturizing intracellular delivery approaches using the microfluidic platform.

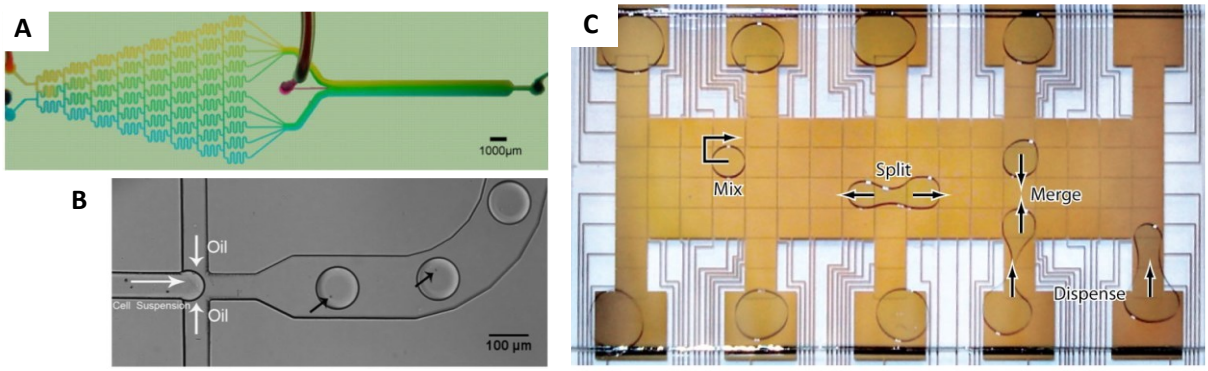

Figure 1-2. The microfluidic platform consists of three main paradigms.
(a) Channel-based[66], (b) Droplet-in-channel[67], and (c) Digital microfluidics[68]. Reproduced with permission from American Society for Microbiology[66], Oxford University Press[67] Annual Reviews, Inc.[68].

1.3.1 Channel microfluidics

Channel based microfluidics is characterized by its micron-sized channels (width and height) that control fluid flow, like a micron-sized pipe. Fabrication of channel-based microfluidic devices is mostly done via soft lithography methods. Briefly, a substrate, typically silicon wafers, is patterned with a SU-8 negative photoresist to create positive molds where polydimethylsiloxane (PDMS) is poured over and cured. Once cured, the PDMS is peeled off and now has a negative trench which forms a closed channel when plasma is bonded to a substrate, typically glass. As a result, the channel geometry, width, and height can all be easily controlled by designing a mask for SU-8 photolithography, making it very appealing and easy for rapid prototyping.

Because of the small dimensions of these microfluidic devices, the fluids within the channels experience a high surface-to-volume ratio which makes macro-scale forces that keep liquids in motion, such as inertial forces, become insignificant. Instead, forces responsible for the resistance of the body of liquid deforming, referred to as viscous forces, become an important force to consider on the micro-scale. Consequently, the dominance of these forces would change

the regime of the flow. To quantify this, the dimensionless Reynolds number (***Re***), which relates the viscous and inertial forces, is used to determine the type of flow regimes to be expected in the system shown in **Equation 1-1.**

Equation 1-1. Reynold's Number.

$$Re = \frac{Net\ Inertial\ Forces}{Net\ Viscous\ Forces} = \frac{\rho v L}{\eta}$$

where ρ is the fluid density (kg/m^3), L for the characteristic length of the system, v for the mean velocity (m/s), and η for the kinematic viscosity (m^2/s). **Figure 1-3** shows the nature of flow for different Reynolds numbers [69].

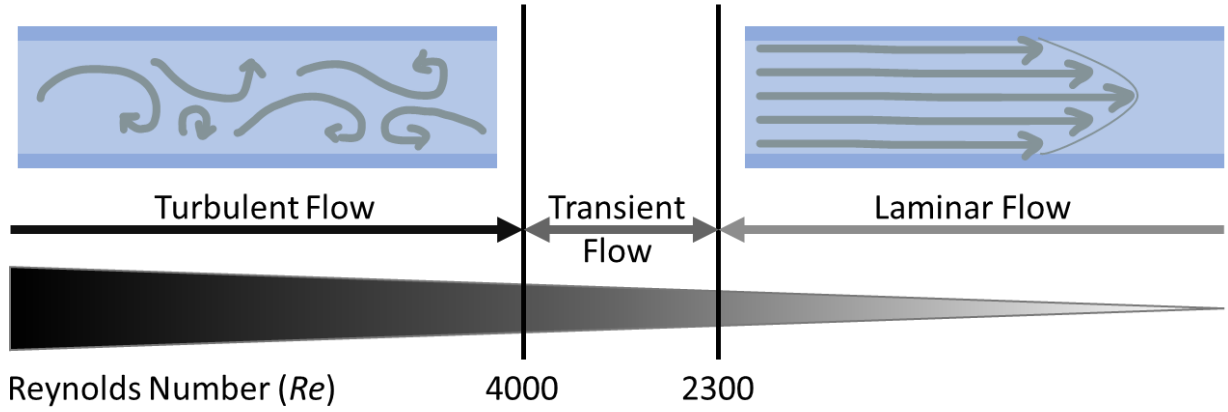

Figure 1-3. Fluid flow regimes based on Reynolds Number.

Fluids in microchannels typically follow a laminar flow profile where mass transport is limited to diffusion only since there are no eddies or whirls which are typically found in turbulent flows. This is unfavorable as mixing is an essential step in most laboratory protocols and homogeneous reagent preparation is required for a variety of biological and chemical assays. To overcome this, several microchannel mixing techniques have been developed which enhance mixing either passively or actively[70,71]. In passive mixing, special channel geometries are designed such as intersecting channels[72], zigzagged channels[73], integrated grooves[74], or 3D

serpentine channels[75,76], where mixing is dependent on the induction of chaotic advection currents. On the other hand, active mixing relies on external energy sources, such as ring valves[77–79], acoustics[80], thermal actuation[81], or dielectrophoresis[82], to create disturbances and speed up the diffusion process.

Figure 1-4 shows some channel-based microfluidic devices designed for passive and active mixing.

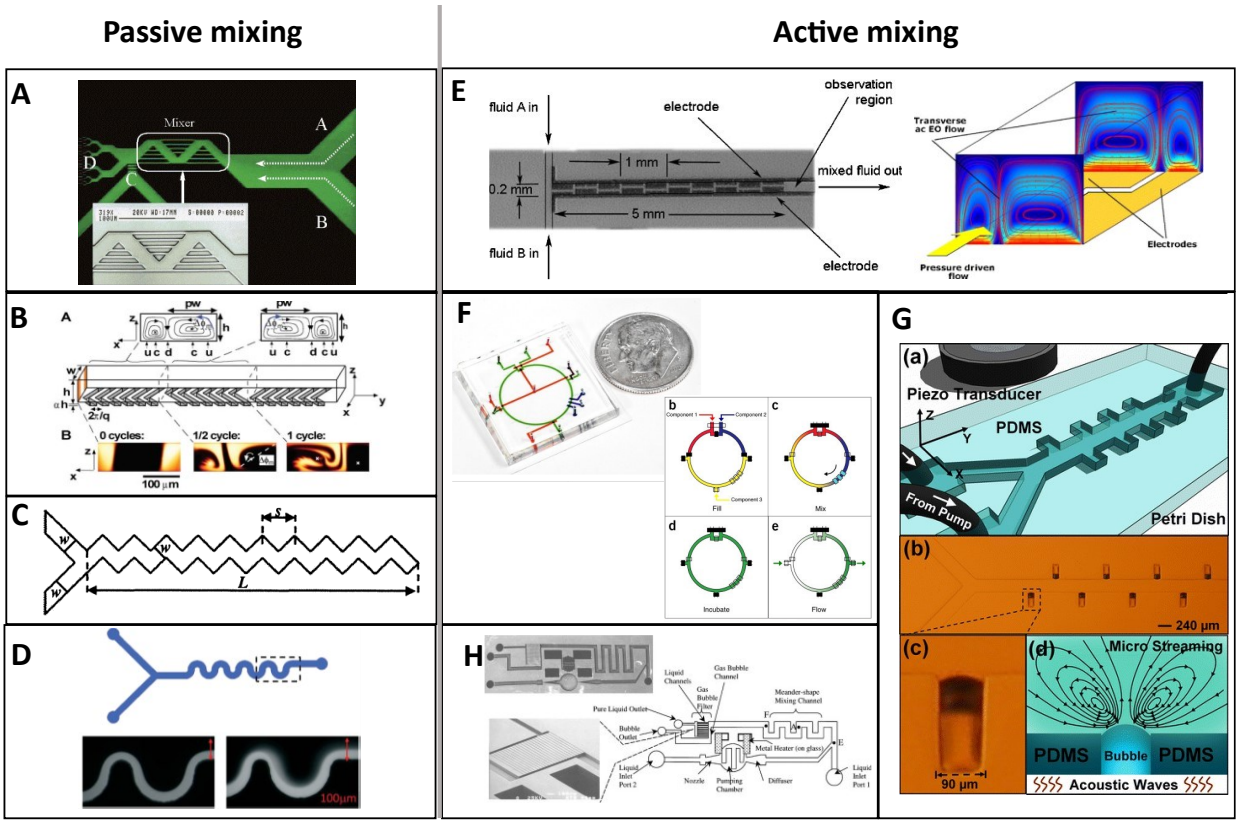

Figure 1-4. Channel microfluidic mixers.
(a) Intersecting channels – Reproduced with permission from American Chemical Society[72]. (b) Integrated herringbone grooves in channels – Reproduced with permission from American Association for The Advancement Of Science[74]. (c) Zigzag channels – Reproduced with permission from American Chemical Society[73]. (d) Serpentine channels – Reproduced with permission from Royal Society Of Chemistry[76]. (e) Dielectrophoretic mixing through micro-electrodes actuation on the substrate layer – Reproduced with permission from Springer[82]. (f) Ring valves mixing: through sequential valve actuations – Reproduced with permission from Springer Nature[79]. (g) Acoustic Mixing: through utilizing piezo transducers – Reproduced with permission from Springer[80]. (h) Thermal mixing: a thermal bubble actuated nozzle-diffuser micro-pump – Reproduced with permission from Elsevier S.A.[81].

Alternatively, the diffusion-only aspect of laminar flow can also be an attractive tool as it allows precise control of molecules leading to the formation of static and dynamic gradients which are needed in many biological applications such as drug screening and biomedical research[83]. For example, coculturing cells on a microfluidic device can create what is known as an organ-on-chip. Because of the diffusion-only mass transport and long-term culture of cells in hydrogels in isolated channels, specific long-range (paracrine) interactions can be studied with ease. In comparison to conventional methods, plate-based culture conditions lack the ability to coculture cells in separation making the differentiation between the effects of long and short-range (juxtracrine) signalling difficult[84]. The use of channel microfluidics is widespread, but several syringe pumps for different reagents, convoluted fabrication techniques for special features (i.e. creating mixing chambers), and integration of microvalves for fluid motion control add complexity to the system which may compel users to exploit other types of microfluidics.

1.3.2 Droplet microfluidics

Droplet microfluidics is best known for its ability to create discrete pico- to nanolitre droplets in multiphase immiscible fluids in microchannels for high-throughput analysis. These devices typically adopt a channel design optimized for fluid shearing, such as T-junction, co-flow, or flow-focusing, and need precise control of flow using syringe pumps or compared air for droplet generation[85] (**Figure 1-5**). Additionally, surfactants are used to help stabilize the droplets to form discrete droplets and prevent them from merging. By using Poisson distribution, researchers can encapsulate single components into droplets with a certain confidence and each droplet can be viewed as an independent reaction chamber, making this platform an attractive tool for high-throughput analysis[86]. Multi-component droplets can also be achieved by co-encapsulation or merging with other substrates such as antibodies[87], DNA beads[88–90], and

detection probes[91] which enables a wide range of studies with several downstream droplet manipulations like mixing[92], sorting[93,94], merging[95,96], and splitting[97,98] (**Figure 1-5**). The main disadvantage droplet microfluidics lies in its dependency on very precise flow control systems that add to the system's complexity, making it difficult for individuals with no background. This platform is also constrained in its ability to address each droplet individually in a controllable manner and is dependent on the Poisson distribution for encapsulating components which generates a large number of empty droplets[93]. Hybrid microfluidic devices, which combine droplet microfluidics and digital microfluidics, have been developed to overcome this limitation and provide a way to precisely control individual droplets[99,100].

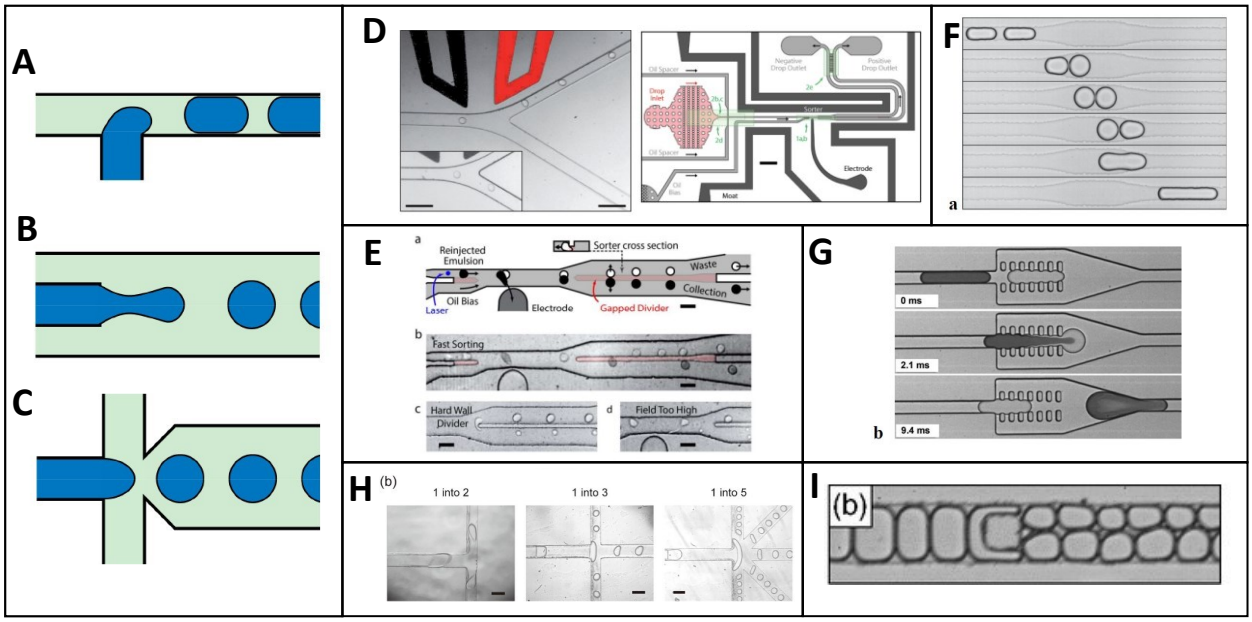

Figure 1-5. Droplet microfluidics.
(a) Cross-flowing streams in a T-shaped junction, (b) co-flowing streams, and (c) flow-focusing streams for generating droplets in channels – Reproduced with permission from American Chemical Society[85]. (d,e) Dielectrophoretic sorting, (f,g) droplet merging, and (h, i) droplet splitting are ways droplets in channels can be manipulated for high-throughput analysis – Reproduced with permission from Royal Society of Chemistry[93,94,96], American Physical Society[95,98], and AIP Publishing[97].

1.3.3 Digital microfluidics

In the last decade, digital microfluidics (DMF) has become more popular due to its potential to automate and make lab-on-chips truly possible. These DMF devices are commonly composed of an array of electrodes to manipulate pico- to microliter droplets in a very precise manner. Through the application of voltages to specific electrodes in a sequential manner, droplet manipulations such as merging, tracking, splitting, mixing, and dispensing from a reservoir can occur (**Figure 1-2c**). The most attractive part of the DMF platform is its droplet addressability without the need for external pumps, valves, and channels, eliminating clogging issues that other microfluidic paradigms require. The ability of DMF platforms to be programmable, reconfigurable, reusable, and scalable has made it an appealing tool. DMF is used in a variety of biomedical applications ranging from laboratory automation, chemical synthesis, cell culture and more[68,70,101].

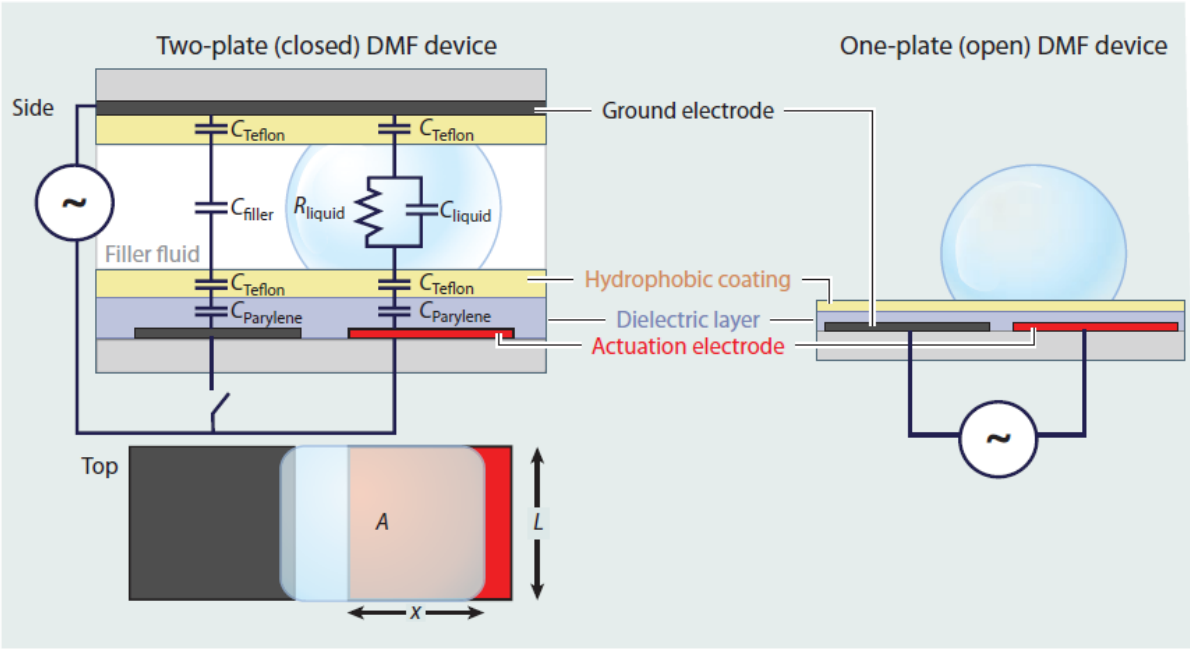

Figure 1-6. Digital microfluidics (DMF).
Two-plate (left) and one-plate (right) DMF system configuration – Reproduced with permission from the Annual Review of Analytical Chemistry[68].

DMF devices can be found in either single-plate or two-plate configurations, depending on the application of the device, as shown in **Figure 1-6.** For a two-plate configuration, the fabrication process can be broken down into two parts: a top-plate and a bottom plate. The top-plate is typically a glass plate coated with a transparent conductive metal called indium tin oxide (ITO) which is essential for providing a continuous grounding electrode for the circuit while providing droplet visibility. The bottom plate is slightly more complex consisting of the actuation electrodes patterned from chromium electrodes on a glass substrate which is then coated with an insulating dielectric layer. (**Figure 1-6**). Both the top and bottom plates are coated with a final hydrophobic layer to reduce the surface tension between the droplets and the substrates. (**Figure 1-6**). Comparatively, the single-plate configuration consists of only the bottom plate where both actuation and grounding electrodes are patterned on the bottom plate. Both types of DMF are widely used for a wide range of applications, however, the single-plate configuration is only capable of simple droplet movements such as mixing and merging due to weaker electric fields generated[68]. The two-plate configuration can generate stronger electric fields and is therefore capable of splitting and dispensing operations, making it more attractive for lab-on-chip applications. Nonetheless, the DMF platform is an attractive tool for miniaturizing and automating laborious protocols in order to save time and cost[12,68,101]. Since its discovery, DMF has been extensively used for cell-based applications and is also a promising platform for large-scale parallelization with simple PCB-based designs capable of handling up to 50 samples in parallel, and more complex designs can handle 1000s of droplets at a time[102]. These recent advances paved the way for more complex experimental protocols to be automated on the DMF platform such as automating gene editing using digital microfluidics to decipher cancer pathways[103], and automating viral generation, packaging, and transduction[104]. The

research described here is based on the idea to automate mammalian transfection to deliver plasmid-based CRISPR-Cas9 machinery into cells for the knockout of a stably expressing reporter gene within the cells as a proof-of-principle. This sets the foundation of this project and the objectives will be discussed in detail in **Chapter 1.4**.

1.3.3.1 Theory of digital microfluidics

There are several theories behind the driving force of droplet movements in DMF. The main driving force of DMF was first attributed to the electrowetting phenomenon where a surface's wettability can be tuned by applying a voltage. First observed by Gabriel Lippmann back in 1875[105], the term "electrowetting on dielectrics" (EWOD) was later used to describe the change in contact angle of a sitting droplet on a substrate when a charge is accumulated on the dielectric layer separating the liquid and the conductive substrate using electric fields[106,107]. By applying an electric potential across a dielectric material via an electrode, the charge is built up across the dielectric layer leading to the generation of electrostatic forces above the actuated electrode. This reduces the contact angle between the droplet and the actuated electrode resulting in asymmetric contact angles across the droplet and build-up of capillary pressure leading to droplet movement[108–110]. The earliest theoretical efforts in estimating the EWOD driving force were proposed to be Young-Lippmann's equation shown in **Equation 1-2.**

Equation 1-2. Driving force using Young-Lippmann's Equation.

$$F = L\gamma\,(\cos\theta - \cos\theta_0) = \frac{\varepsilon_0\varepsilon_r L V^2}{2d}$$

where L is the length of the contact line overlapping the actuated electrode; γ is the liquid/filler media surface tension; θ and θ_0 are the static contact angles with and without applied voltage, respectively; ε_r is the relative permittivity of the dielectric; ε_0 is the permittivity of free space; V

is the applied voltage; and d is the dielectric thickness. This EWOD model describes droplet movement well, however, it is heavily dependent on a change in contact angle to drive droplet movement which fails to explain the liquid-dielectrophoretic force, which is predominant at high frequencies for dielectric liquids, or why some reagents can still move with little to no change in contact angle[111,112]. For example, droplets of toluene and chloroform can still move without a change in their contact angle[111,113]. As such, the EWOD model was found to be insufficient in describing the behaviours of droplet movements on DMF.

Alternatively, DMF forces and droplet movements can also be explained by an electromechanical model. First considering that two hydrostatic effects occur under electrostatic fields where (1) a net force is experienced by the liquid in the presence of a nonuniform electric field, and (2) the contact angle of the liquid changes on a dielectric surface, these hydrostatic effects can be assumed to be electromechanical. Chatterjee *et al.* proposed adopting an electromechanical model where a circuit diagram can be used to estimate the driving forces in DMF[112]. Through this model, the amount of energy, E, (**Equation 1-3)** capacitively stored in the system can be calculated as a function of frequency, f, and droplet position along the x-axis (the direction of droplet propagation), assuming that the cross-sectional area of the drop can be approximated as a square with sides of length L (**Figure 1-6**).

Equation 1-3. Energy equation using electrochemical model.

$$E(f,x) = \frac{L}{2}\left(x\sum_i \frac{\varepsilon_o\, \varepsilon_{ri,liquid}\, V_{i,liquid}^2\, (j2\pi f)}{d_i} + (L-x)\sum_i \frac{\varepsilon_o\, \varepsilon_{ri,filler}\, V_{i,filler}^2\, (j2\pi f)}{d_i} \right)$$

where $\varepsilon_{ri,liquid}$, $V_{i,liquid}$ and $\varepsilon_{ri,filler}$, $V_{i,filler}$ are the relative permittivity and voltage drop for the liquid and filler fluid portions of the electrode, respectively, and d_i is the thickness of layer i

(corresponding to the dielectric, hydrophobic, liquid or filler layers). Differentiating the energy $\boldsymbol{E}$ with respect to $\boldsymbol{x}$ yields the driving force as a function of frequency shown in **Equation 1-4.**

Equation 1-4. Force equation using electrochemical model.

$$\boldsymbol{F(f) = \frac{\partial E(f,x)}{\partial x} = \frac{L}{2}\left(\sum_i \frac{\varepsilon_o\, \varepsilon_{ri,liquid}\, V_{i,liquid}^2\, (j2\pi f)}{d_i} - \sum_i \frac{\varepsilon_o \varepsilon_{\,ri,filler}\, V_{i,filler}^2\, (j2\pi f)}{d_i}\right)}$$

This provides the electromechanical model an advantage in estimating the driving force as it takes into account the frequency of the applied voltage on droplets across each layer of the device, representing the stored energy in the system that is converted to an applied force. The driving force is therefore understood to be a function of the frequency of the applied potential where a critical frequency can be calculated for each device geometry/liquid combination. Below this frequency, the electrostatic EWOD model holds where the driving force at lower frequencies comes from the accumulation of charges near the three-phase contact line (the point of contact between solid, liquid and gas) which pull the droplet towards the actuated electrode electrostatically. In this regime, the capacitive energy stored within the dielectric dictates the magnitude of this force. Above the critical frequency, the liquid insulates, and the droplet movement is dominated by liquid-dielectrophoretic forces generated from the electric field gradient across the droplet. Here, the difference in permittivity of the liquid and filler medium dictates the magnitude of the driving force[68,112]. Either way, both models predict droplet movement in a way that is dependent on several factors such as the permittivity of materials, dielectric thickness, and the applied potential difference. EWOD and electromechanical models are both used to calculate the forces for most DMF systems.

1.4 Microfluidics intracellular delivery

Since the development of genetic engineering, significant progress has been made in microfluidic platforms focusing on the intracellular delivery of biological payloads into cells. As previously mentioned, the miniaturization of the described transfection methods onto microfluidic devices is particularly appealing to researchers because of the ability to uniformly treat cells, overcoming the disadvantages of current bulk scales which suffer from low and inconsistent transfection efficiencies, immunogenicity, loss in cell functions, and complex protocols contributing to operational difficulties, high cost and the need for extensive labor[46,47]. Microfluidics has enabled precise cell manipulation and universal delivery of nearly any biological payload into different cell types with better transfection efficiencies, greater precision and higher throughput than its conventional bulk alternatives[46,47], making it appealing to sensitive cell lines like primary T cells in the context of manufacturing cellular immunotherapy. With the help of micro- and nano-fabrication, this has motivated several microfluidic intracellular delivery approaches mainly employing physical transfection methods such as cell deformation through constrictions[114–116], induced shear stress[117], electroporation[118], and more. To learn more, an overview on the different types on intracellular delivery approaches on a microfluidic perspective can be found in reviews by Hur *et al*.[47] and Morshedi *et al*[46]. For example, Jarrell *et al*. have developed a channel-based microfluidic device for mRNA delivery into primary T cells using hydrodynamic-poration[117] **(Figure 1-7a)**. The authors designed their device to generate turbulent vortex flows to induce high shear stress on cell membranes resulting in transient pore formation where internalization of cargo can occur[117,119,120]. Alternatively, flowing cells through constrictions relative to the size of the cells themselves induces membrane deformation and pore formation. Using this technique, called cell squeezing, DiTommaso *et al*.

demonstrated the delivery of dextran molecules and Cas9 RNPs for gene knockout experiments in human and mouse primary T cells with success comparable to that of conventional electroporation methods[56] **(Figure 1-7b)**. Their device, however, is a silicon-based microfluidic device which requires a more complex fabrication method than PDMS-based microfluidic devices[114,121]. Nonetheless, cellular immunotherapy generated from cell squeezing shows promise and has been used in clinical applications involving cellular immunotherapy[122]. Building on these studies, increasing contact between the cells and cargo through mixing and convective flows has been proposed to increase transfection efficiency as internalization of cargo into cells is limited by diffusion once cells are permeabilized. Joo *et al*. demonstrate this by developing a similar squeezing mechanoporation technique in which droplets-in-oil containing cells and cargo is squeezed through constrictions on a PDMS microfluidic device[115] **(Figure 1-7c)**. By optimizing design of the construction (ie. length, size, and number of constrictions) the authors also demonstrated successful delivery of mRNA and plasmids into immortalized and primary T cells similar to that of conventional electroporation and Lipofectamine transfection methods[115].

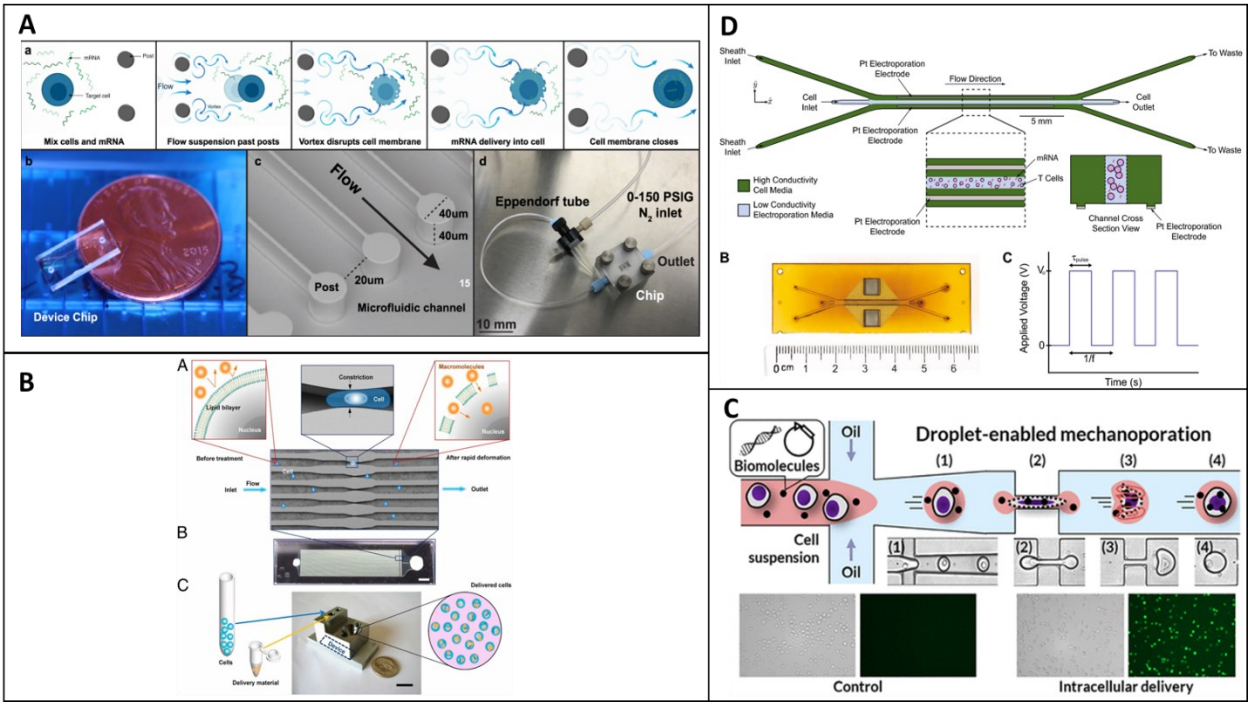

Figure 1-7. Microfluidic platforms focused on transfecting primary human T cells for cellular therapy manufacturing.

These microfluidics platforms use (a) vortex shedding hydrodynamic-poration, (b) channel cell squeezing mechanoporation, (c) droplet-enabled cell squeezing mechanoporation, and (d) electroporation to deliver biological cargo into primary T cells – Reproduced with permission from Springer Nature[117,118], National Academy of Sciences[121], and American Chemical Society[115].

Besides hydrodynamic-poration and mechanoporation transfection approaches, electroporation has also been miniaturized on the microfluidic platform enabling highly localized, concentrated, and uniform electric fields at lower voltages where increased cell viability and uniform transfection efficiency can be expected. This is achieved by minimizing the harmful effects of electroporation, such as large bubble generation, heat fluctuations, and pH changes, by using hydrodynamic focusing in channel microfluidics to make liquid electrodes. Utilizing laminar flow in channel microfluidics, cell suspension streams can be sandwiched by a conductive medium where metal electrodes are in contact with the liquid conductive medium, away from the cells. Zhu *et al*. first demonstrate this by successfully transfecting 70% of yeast cells in a continuous-flow manner[123]. Additionally, by controlling the flow rates of the respective solution, the authors show focusing of cell suspension into a thin stream which reduces the distance

between electrodes generating a higher electric field[123]. Lissandrello *et al*. utilize a similar liquid-liquid electrode interface using trifurcated channels containing high and low conductive buffers for electroporating primary T cells in a continuous-flow manner[118] **(Figure 1-7d)**. In doing so, the authors successfully transfected primary T cells with mRNA with up to 75 to 95% transfection efficiency. Later, the authors improved the device by using acoustophesis to isolate transfected primary T cells into recovery buffer for automating the production of cellular therapy in a high-throughput manner[124]. Despite these advances in microfluidic approaches to intracellular delivery of cargo into primary T cells, these methods are based on channel microfluidics which excels at generating high throughput (> millions) genetically engineered cells with the same genetic edit but are limited in their ability to perform a large number of gene edits in parallel at smaller cell quantities. This is particularly important in situations when genetically engineering rare cell types that face challenges in expansion and cell culture to generate enough cells for each reaction. For instance, cell-based immunotherapies require inactivated primary T-cells[125], natural killer cells, more rare immune cells such as tumor-infiltrating leukocytes[126] (TILs), or gamma-delta T cells[127] which are challenging to recover and to expand[128]. To overcome this limitation in acquiring a high enough cell sample, an initial screening of a large library of gene constructs can be assessed using an immortalized cell line to select high-performing variants for a more focused study in rare cell types. For example, a recent report from Bloemberg *et al.* outlined a method where they selected 5 high performing CARs constructs targeting a solid tumor-specific antigen (EGFRvIII) from a pool of 15 unique CARs by first assessing their efficacy in Jurkats, an immortalized human T cell line[129]. The authors then assessed this smaller library of 5 selected CARs in primary T cells via viral transduction to overcome the cell amount limitation. Currently, optimized electroporation

protocols for working with primary immune cells have shown at least 1-2 million cells per condition is ideal for delivery of biological cargo, and using fewer cells has a detrimental effect on viability and efficiency[28,130]. Hence, if Bloemberg *et al.* wanted to test their entire library using primary T cells using optimized electroporation protocols[130,131], the authors would require 15 to 30 million cells which can be difficult to obtain from a single donor without lengthy ex-vivo expansion protocols. To facilitate rapid screening of large libraries, such as the one developed by Bloemberg *et al*., an alternative approach is needed for effective delivery of target payloads with lower cell numbers and with the potential for parallelization and automation.

1.4.1 DMF and electroporation

To further advance the field of genetic engineering, specifically cellular therapy, researchers need the capability to assess large arrays of genetic perturbations in an automated manner, allowing them to cycle through design iterations in rapid succession and perform a large number of gene edits in parallel with small cell quantities. As previously mentioned, DMF provides a platform for high scalability and automation potential making it an attractive tool for miniaturizing and automating laborious protocols to save time and cost.

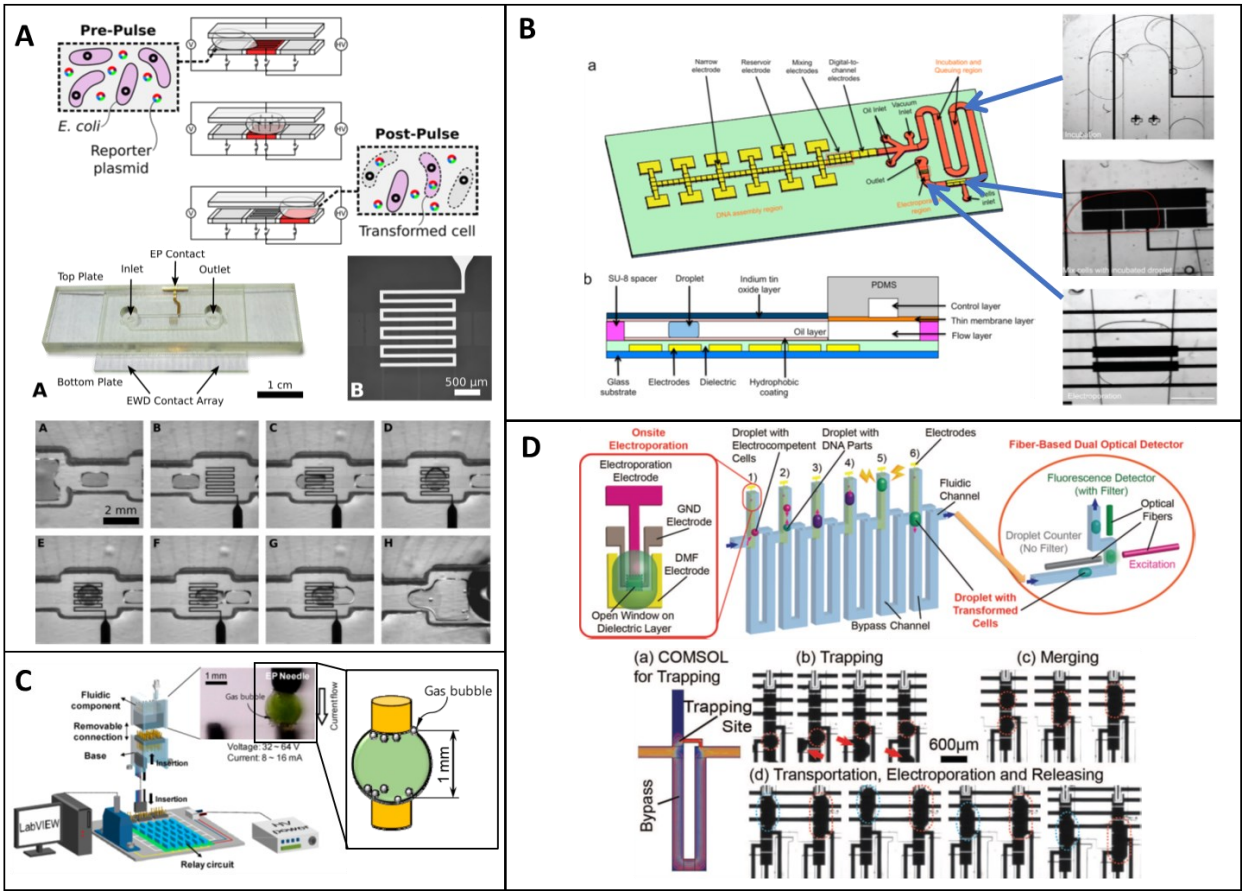

Figure 1-8. Current digital microfluidic electroporation devices.
(a) Two-plate DMF system for electroporating *E. coli.* (b) Hybrid-DMF device for DNA assembly and electroporating *E. coli* and *S. cerevisiae*. (c) Open DMF system for electroporating microalgae in droplets. (d) Hybrid-DMF device for trapping and merging of *E. coli* and DNA containing droplets for in-droplet electroporation -– Reproduced with permission from American Chemical Society[132–134] and IEEE[135].

In recent years, DMF has been used to automate lipid-based[103] and viral transfection[104] into mammalian cells, however, efforts to integrate physical transfection methods such as electroporation into a DMF platform have been limited to only microbial cells[132–136] (**Figure 1-8**) and are not suitable for mammalian cells due to high cell death associated with electroporation systems. As mentioned in previous sections, bulk cuvette electroporation suffers from several limitations including reproducibility and high cell death. This can be attributed to the development harmful electroporation environments generated during application of high voltage to achieve high electric field strengths for electroporation[58]. In cuvette electroporation, for

example, the size of the electrodes is significantly larger than the size of cells which has the potential to create non-uniform electric fields resulting in inconsistent and excessive pore formation and cell death. In addition, following *Ohm's* Law, which states that

Equation 1-5. Ohm's Law

$$\boldsymbol{V = I \times R} \text{ or } \boldsymbol{I = \frac{V}{R}}$$

where $\boldsymbol{V}$ is the voltage potential, $\boldsymbol{I}$ is the current, and $\boldsymbol{R}$ is the resistance of the system which can be further calculated using **Equation 1-6.**

Equation 1-6. Resistance and resistivity formula

$$\boldsymbol{R = \frac{\rho L}{A}}$$

where $\boldsymbol{\rho}$, $\boldsymbol{L}$, and $\boldsymbol{A}$ is the resistivity, length, and cross-sectional area of the material, respectively, we can see that the larger the electroporation electrode cross-sectional area **A**, the smaller the resistance **R** of the system. Because resistance $\boldsymbol{R}$ is inversely proportional current $\boldsymbol{I}$ generated in the system, cuvette electroporation with large electrode size creates a very low resistance system which increases the current generated during electroporation when high voltage is applied. The excessive current generated is then converted to Joule heating, pH changes, and electrode metallic ion discharge which create a harmful environment that negatively impacts the buffer composition of both the cells and biological cargo being delivered[47–53]. This is particularly important in the context of therapeutic applications where electroporation-induced cell toxicity, low long-term viability and impeded recovery is commonly observed amongst electroporated primary cell lines[54–58].

To overcome these limitations, scaling down electroporation has been a favorable approach. To understand why we first must understand two main phenomena that occur during application

of high voltage: (1) joule heating and (2) hydrolysis. Joule heating, also known as Ohmic heating, is the process by which electric current is converted into heat. The formula for joule heating is described **Equation 1-7**.

Equation 1-7. Joule heating

$$\boldsymbol{Energy} = \mathbf{I} \times \mathbf{V} \times \boldsymbol{t} = \frac{\boldsymbol{V^2}}{\boldsymbol{R}} \times \boldsymbol{t}$$

where ***I*** is the current generated, ***V*** is the voltage applied to the system, ***R*** is the resistance of the system and ***t*** is the time the current is allowed to flow. As such, we can see that current ***I*** generated is directly proportional to joule heating which leads to increase in temperature. In the context of cuvette electroporation and biological systems, the increase in temperature is unfavourable above 42°C where cell viability may be affected, and protein coagulation and enzymatic damage occur between 60°C to 100°C[137]. Reducing the current generated in electroporation systems is therefore advantageous in reducing the effects of Joule heating.

On the other hand, due to the high voltage application and excessive current generated during electroporation, electron charge and discharge occurs leading to electrochemical reactions at the metal-liquid interface[48]. The effects of this are twofold. First, metallic electroporation electrodes get discharged into the medium as ions which ultimately contaminates the buffer and can be cytotoxic to cells[53]. Second, harmful hydrogen/hydroxyl species are generated (underlined in **Equation 1-8**) and localized at the metal-liquid interface[48]. The electrochemical reactions are described in **Equation 1-8**.

Equation 1-8. Electrochemical reactions during electroporation

$$\boldsymbol{Cathode}: \mathbf{2}\,\boldsymbol{H_2O} + \mathbf{2}\,\boldsymbol{e^-} \rightarrow \mathbf{2}\,\underline{\boldsymbol{OH^-}} + \boldsymbol{H_2}$$

$$\textbf{Anode}: H_2O - 2e^- \rightarrow 2\underline{H^+} + \frac{1}{2}O_2$$

$$2Cl^- - 2e^- \rightarrow Cl_2$$

$$Cl_2 + H_2O \rightarrow HClO + \underline{H^+} + Cl^-$$

As a result, these hydrogen/hydroxyl species increase the pH of the medium which negatively impacts cell health[48,138]. These factors must be taken into account where there are clear benefits in reducing current generated during electroporation to improve cell viability and efficiencies.

An approach to reduce the generated current is to increase the resistivity of the system. This can typically be done by changing the electroporation buffer in which cells and delivery molecules are suspended from a lower conductivity buffer to a higher conductivity buffer[139,140]. Alternatively, a capillary electroporation system consisting of electroporation samples inside a long and narrow tube with electrodes on either end of the tube could be used in which the cross-sectional area of the electrode is significantly reduced, reducing the overall resistivity[141]. Additionally, the increase in distance between electrodes prevents complete mixing of electrochemical species with the cell. However, higher voltages still need to be applied to achieve similar electric field strengths to accommodate the increase in distance as electric field strength is proportional to voltage applied and inversely proportional to distance. This increases the bubble generation due to higher voltage applied, which can cause insulation of electrode and inhibit complete electroporation pulse treatment.

Owing to its ability to manipulate fluids on a microscale, microfluidics has become an attractive tool for scaling down electroporation as discussed in previous sections. Several channel-based microfluidic studies have tried rectifying these problems by sandwiching

electroporation samples in low conductive buffers between high conductive buffers. Demonstrated by Zhu *et al.* and Lissandrello *et al.* (

d), the utility of this approach is twofold. First by creating a high-resistance electroporation environment to reduce current and, second, to isolate cells away from metallic electrodes to protect cells from electrochemical species[118,123], higher transfection efficiencies and cell viabilities can be achieved. Furthermore, the miniaturized microfluidic system brings forth more uniformity in the electric field, reducing inconsistencies and excessive cell perturbations resulting in more repeatable efficiencies between experiments. Nonetheless, as mentioned earlier, these channel-based microfluidic devices excel at high throughput genetic engineering for manufacturing applications, however, lack the high controllability and parallelization, typically found in DMF, needed for performing large number of gene edits in parallel at smaller cell quantities such as in cellular immunotherapy research[129].

To our knowledge there has only been one mammalian cell electroporation device that uses an array of electrodes, similar to that of DMF, however, droplet manipulation is dependent on electrophoresis of charged droplets with the potential for parallelization and automation. Im *et al.* demonstrated successful delivery of plasmids into Jurkat T cells with 76% cell viability and 66% transfection efficiency (vs 11.4% cuvette electroporation)[142]. Similarly, by significantly scaling down the system, the authors achieved a smaller cross-sectional area which reduced the resistance and overall current of the system. The authors also increased the cell concentration 50 times to reduce the current load per cell which is presumed to favour cell viability and recovery post-electroporation[142]. The authors purpose the potential to carry out arrayed electroporation experiments, however, each unique reaction requires double the cell amount per electroporation reaction in the Neon™ system (200,000 vs 100,000 cells per reaction) making it impractical for

engineering rare cell types or cells that are difficult to culture and expand[125–128]. In addition, despite demonstrating ~5 times higher transfection efficiency than conventional methods and electroporation in other cell types[143], the system has cells in direct contact with the electroporation electrodes, exposing cells to extreme pH change, gas bubble generation, and Joule heating which are detrimental to cell viability[141], which could explain some cell death resulting in only 76% viable cells. To develop a highly controllable and automated DMF platform for electroporating cells for genetic engineering, leveraging the success of these channel-based electroporation systems, a similar design strategy will need to be taken. Additionally, this opens the possibility for integrating an electroporation system with other DMF devices to allow for end-to-end automation of mammalian cell engineering similar to what has been shown previously for microbial cells[144,145].

1.5 Thesis objectives

To overcome the challenges described above and to further advance the field of genetic engineering, specifically cellular immunotherapy, we introduce the first three-droplet structure assembly (triDrop) for facilitating electroporation on a DMF platform. In this work, we report the novelty behind triDrop by transfecting mammalian cell lines with various biological payloads and showing a functional knockout. To show its applicability for cellular immunotherapy research, we also show successful transfection of primary T cells with mRNA and plasmids.

To achieve this goal, my research objectives are divided into the following steps.

1. *Chip design and fabrication*: Numerical simulations were established to understand the electric field and field-focusing effects generated across the droplet upon application of high voltage potential during electroporation. The chip design was hence driven by its ability to consistently form the triDrop structure in a repeated manner.
2. *Platform optimization*: Electroporation on HEK293 cells, an easy-to-transfect cell line, was carried out using fluorescently labelled dextran molecules to validate the numerical simulation and optimize the transfection efficiency of the system to achieve performances similar to that of conventional electroporation systems.
3. *Proof-of-concept*: To show the broad applicability of our system to other cell lines with biologically relevant payloads, electroporation parameters were further optimized for the delivery of mRNA and plasmids into easy-to-transfect (HEK293 and HeLa cells) and hard-to-transfect (Jurkat cells) cells lines. Flow cytometry and fluorescent microscopy were used to quantify the transfection efficiency and optimize the system.
4. *Application*: To confirm the broad applicability of our platform in genetic engineering, we performed a gene knock-out on the Beta 2 Microglobulin (β2M) surface marker in Jurkat

cells using the CRISPR-Cas9 system and validated it using immunostaining and flow cytometry. Additionally, to show the system's potential applicability in cellular immunotherapy, we show successful electroporation and delivery of mRNA and plasmids into human primary T cells with post-permeabilization viabilities similar to that of unelectroporated samples.

These results, to our knowledge, are the first of their kind and serve as examples of what is possible for the future – a new technique for intracellular delivery in an arrayed and automated fashion using small cell quantities. This could potentially serve as a platform for ex vivo applications for the research of personalized medicine and cellular immunotherapy.

Chapter 2 Materials and Methods

In this chapter, the methodology behind the experiments done during the development, characterization, and optimization of the triDrop system on the digital microfluidics platform is described.

2.1 Reagents and materials

Unless specified otherwise, general-use chemicals and kits were purchased from Sigma-Aldrich (St. Louis, MO). Device fabrication reagents and supplies included chromium-coated glass slides, and gold-coated glass slides with AZ1500 photoresist from Telic (Valencia, CA), MF-321 positive photoresist developer from Rohm and Haas (Marlborough, MA), chromium etchant 9051 and gold etchant TFA from Transene (Danvers, MA), AZ-300T photoresist stripper from AZ Electronic Materials (Somerville, NJ), Teflon-AF 1600 from DuPont Fluoroproducts (Wilmington, DE). Transparency masks for device fabrication were printed from ARTNET Pro (San Jose, CA) and polylactic acid (PLA) material for 3D printing were purchased from 3Dshop (Mississauga, ON, Canada). General chemicals for tissue culture were purchased from Wisent Bio Products (Saint-Bruno, QC, Canada). Plasmids and mRNA for this study were acquired from Addgene (catalog: 54767) and TriLink Biotechnologies (catalog: L-7201) (see **Figure 2-1** and **Table 2-4** for details**)**. Electronic components were obtained from DigiKey (Thief River Falls, MI). Electroporation buffers were obtained from Harvard Apparatus Canada (St Laurent, QC), Thermo Fisher Scientific (Burlington, ON), or made in-house (see **Table 2-1**). Neon™ transfection reagents were purchased from Thermo Fisher Scientific (Burlington, ON).

Table 2-1. Recipes for various custom buffers used.

Buffer	**Composition**
1SM-Modified	5mM KCl, 15mM MgCl2.6H2O, 25mM Sodium succinate, 25mM Mannitol, pH 7.2
Very high conductive solution	120mM NaCl, 2.8mM KCl, 2mM MgCl2, 20mM CaCl2, 10mM HEPES, 11mM glucose, pH 7.2 with NaOH, 300 mOsm
FACs Buffer	1x PBS, 1mM EDTA, 25mM HEPES (pH7.0), 1% FBS

Table 2-2. eGFP-mRNA sequence

mRNA sequence	AUGGUGAGCAAGGGCGAGGAGCUGUUCACCGGGGUGGUGCCCAUCCU GGUCGAGCUGGACGGCGACGUAAACGGCCACAAGUUCAGCGUGUCCG GCGAGGGCGAGGGCGAUGCCACCUACGGCAAGCUGACCCUGAAGUUC AUCUGCACCACCGGCAAGCUGCCCGUGCCCUGGCCCACCCUCGUGACC ACCCUGACCUACGGCGUGCAGUGCUUCAGCCGCUACCCCGACCACAUG AAGCAGCACGACUUCUUCAAGUCCGCCAUGCCCGAAGGCUACGUCCA GGAGCGCACCAUCUUCUUCAAGGACGACGGCAACUACAAGACCCGCG CCGAGGUGAAGUUCGAGGGCGACACCCUGGUGAACCGCAUCGAGCUG AAGGGCAUCGACUUCAAGGAGGACGGCAACAUCCUGGGGCACAAGCU GGAGUACAACUACAACAGCCACAACGUCUAUAUCAUGGCCGACAAGC AGAAGAACGGCAUCAAGGUGAACUUCAAGAUCCGCCACAACAUCGAG GACGGCAGCGUGCAGCUCGCCGACCACUACCAGCAGAACACCCCCAUC GGCGACGGCCCCGUGCUGCUGCCCGACAACCACUACCUGAGCACCCAG UCCGCCCUGAGCAAAGACCCCAACGAGAAGCGCGAUCACAUGGUCCU GCUGGAGUUCGUGACCGCCGCCGGGAUCACUCUCGGCAUGGACGAGC UGUACAAGUAA

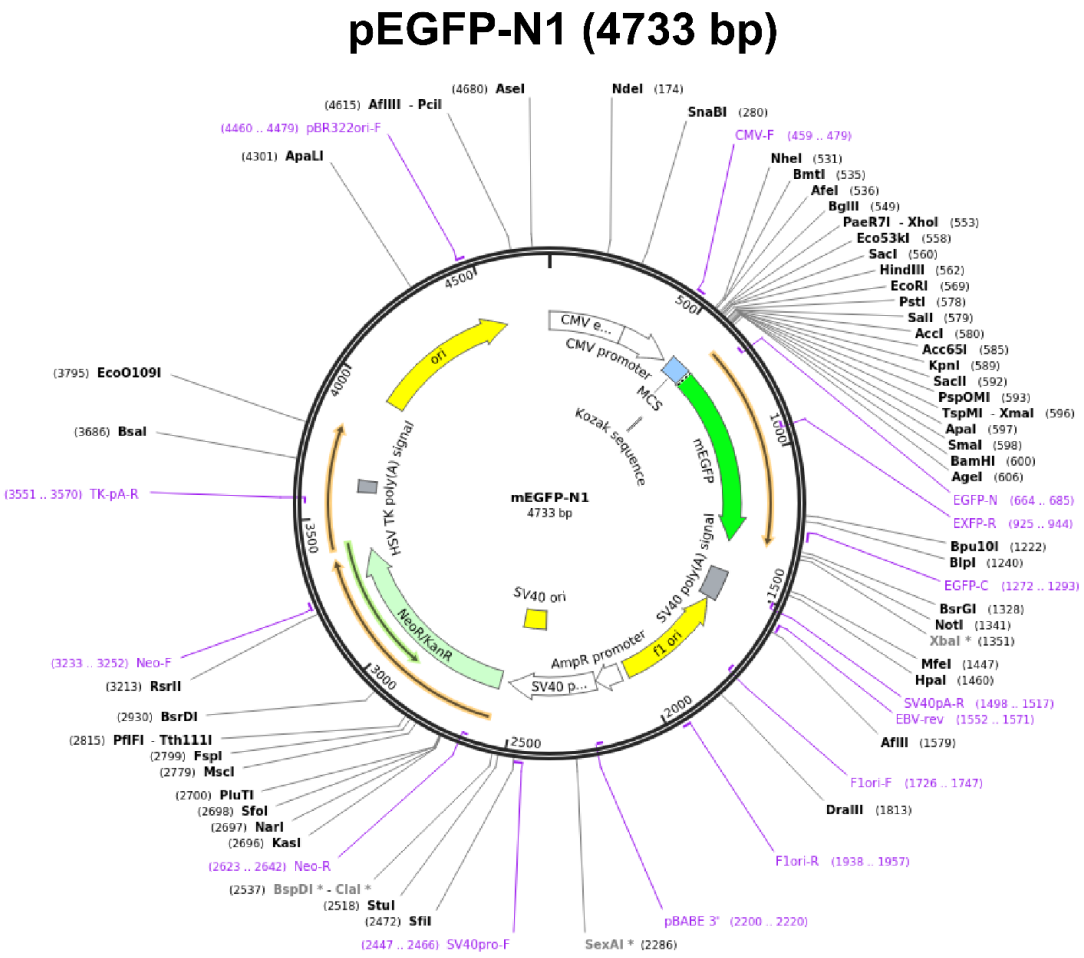

Figure 2-1. eGFP plasmid map.
The plasmid map contains a neomycin or kanamycin resistance marker. The eGFP is driven by a CMV promoter. More information can be found from Addgene (catalog no. 54767).

2.2 TriDrop device fabrication and setup

TriDrop devices, each comprising of a bottom plate with Cr-based electrodes and a top-plate with Au-based electroporation electrodes, were fabricated at Concordia's cleanroom facility using transparent photomasks printed at 25 400 dpi (Artnet Pro, Bandon, OR). An overview of the fabrication process is illustrated in **Figure 2-2**. DMF bottom plates bearing chromium electrodes coated with a SU-8 5 dielectric and Teflon-AF hydrophobic layer were formed using previously outlined methodology[146]. Each bottom plate features an array of 30 actuation electrodes (2 mm by 2 mm), 12 reservoir electrodes (2.9 mm by 5.5 mm) arranged into 3

reservoirs, 6 active dispensing electrodes (2 mm by 2 mm), and 3 splitting electrodes (3.8 mm x 3 mm). The electrode array has inter-electrode gaps of 150 mm and each electrode was connected to a pogo-pin holder.

TriDrop top plates bearing gold electrodes (0.2 mm wide) were formed from a glass substrate coated with 100 nm gold adhered to seed chromium layer (~12 nm). To form the gold electrodes, top plates were spin-coated (10 s 500 rpm, 30 s 3000 rpm, 20 s 5000 rpm) in S1811, exposed through a transparent mask, developed using Microposit MF321 (2 min), washed with DI water, submerged in gold etchant (2 min), washed with DI water, and submerged in AZ stripper to remove the remaining photoresist before being washed with acetone, IPA, and DI water, and dried with nitrogen. To disconnect the chromium from the gold wiring, we followed the above protocol except using CR-4 etchant to remove the chromium. To insulate the gold electroporation electrodes from the Cr-grounding layer, the top plate was surface treated for 45 s in a plasma cleaner (Harrick Plasma PDC-001, Ithaca, NY) before coating a 5 μm dielectric of SU8-5. Briefly, the photoresist was spin-coated (10 s 500 rpm, 30 s 2500 rpm), followed by a soft bake (65 °C 2 min, 95 °C, 10 min), exposed to UV light through a custom mask (5 s), post-exposure baked (65 °C 2 min, 95 °C 10 min), developed in SU8 developer (15 s), rinsed with IPA and DI water, dried with nitrogen, and then hard baked (180 °C, 10 min). Bottom plates were spin-coated with Teflon-AF 1600 in 2 % w/w in Fluorinert FC-40 (10 s 500rpm, 30s 1500rpm). To assemble the completed triDrop device, the top and bottom plates were assembled using two layers of double-sided tape (180 μm total thickness, 3M) and the gold electrode on the top plate were aligned directly above electroporation sites on the bottom plate.

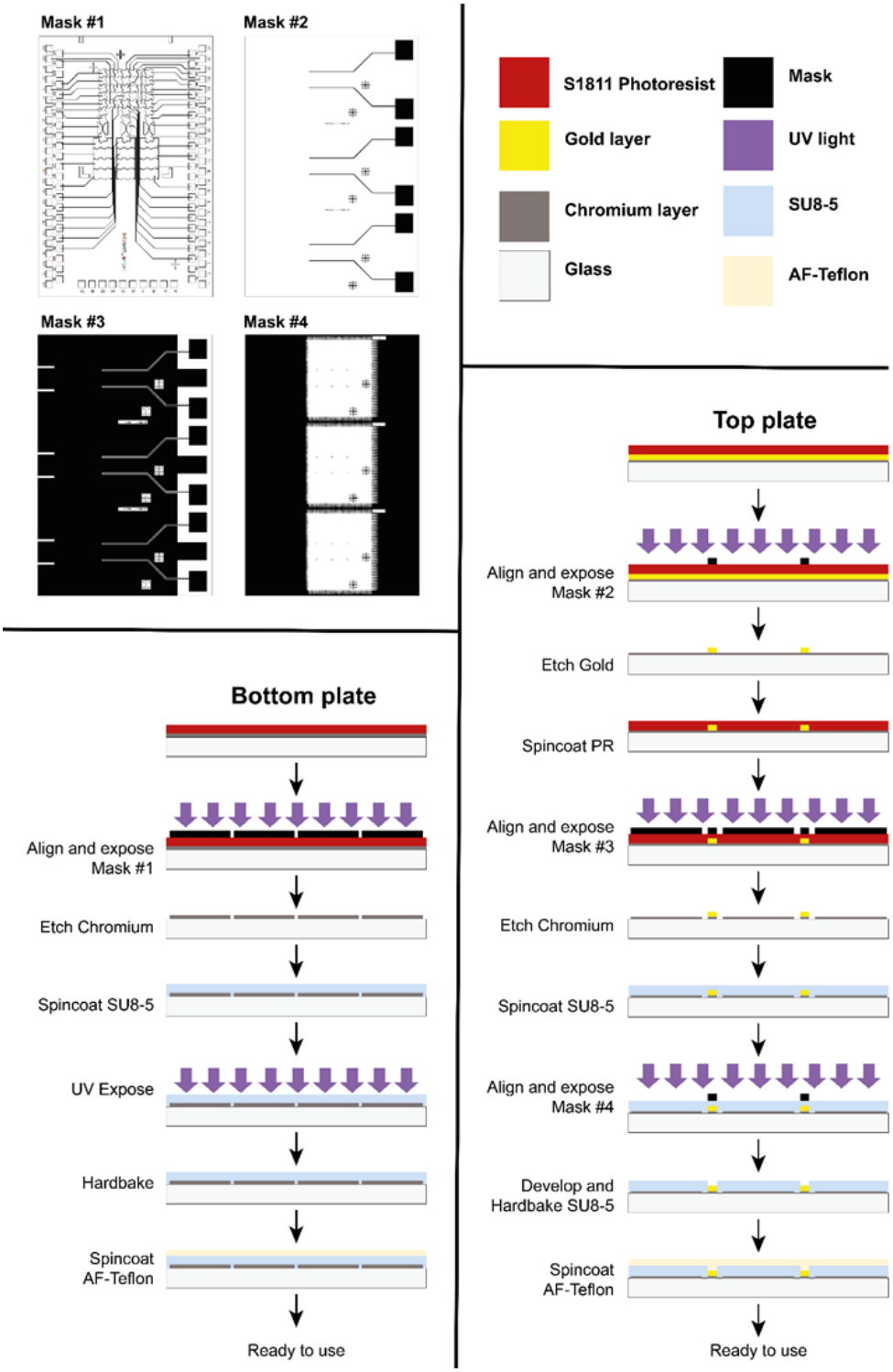

Figure 2-2. Fabrication procedure shown for the triDrop electroporation DMF device.
The bottom plate shows the general procedure for digital microfluidic bottom plate electrode fabrication. The top-plate shows how to fabricate the gold-lines for electroporating the triDrop structure and to create a semi-transparent top-plate to visualize the droplets. After fabrication, the top-plate is aligned with electrodes on the bottom-plate to ensure the flanking (outside) droplets are touching the gold lines (not shown).

2.3 Numerical simulations

Numerical simulations were performed using COMSOL Multiphysics software on a 3D structure. The 3D model of the triDrop structure was generated by taking a video of the triDrop merge sequence using PBS with colored dye as flanking buffers and using a transparent ITO top plate to help visualize the droplets and clearly see the boundaries between the flanking droplets and the sample droplet. The video was analyzed frame by frame and a digital image of the top-down view of the triDrop merge geometry was isolated at 2-seconds post-merge. The image was imported into AutoCAD and the boundaries of the individual droplets were traced to create a model of the triDrop structure. The AutoCAD file was imported into COMSOL Multiphysics and extruded to a final height of 180 μm (the gap between our top and bottom layer).

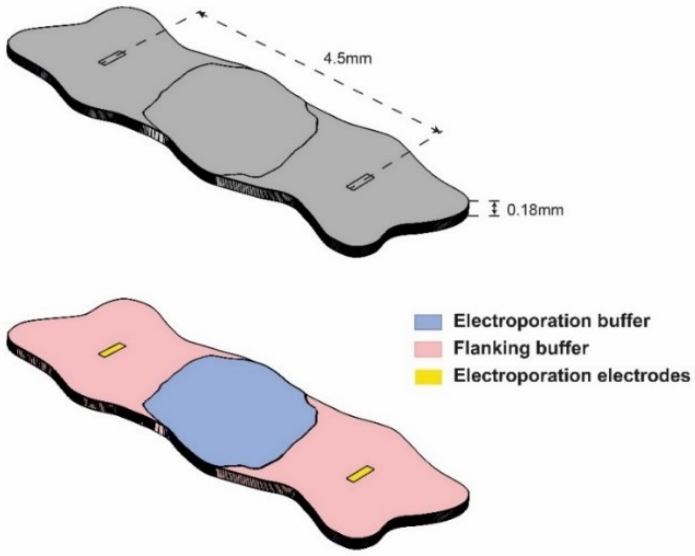

Figure 2-3. 3D COMSOL Model.

The 3D COMSOL model, illustrated in **Figure 2-3**, was used in the simulations using a FINE mesh. Using the electric currents physics module, the following equations were used starting with the point form of *Ohm's* law states in **Equation 2-1.**

Equation 2-1. Vector form of Ohm's law.

$$\boldsymbol{J} = \boldsymbol{\sigma E} + \boldsymbol{J_e}$$

where **J** is the current density (A/m^2), $\mathbf{J_e}$ is the externally generated current density (A/m^2), **σ** is the electrical conductivity (S/m), and **E** is the electric field (V/m). Converting this to its continuity gives us **Equation 2-2.**

Equation 2-2. Ohm's law continuity equation.

$$\boldsymbol{\nabla \cdot J} = -\boldsymbol{\nabla} \cdot (\boldsymbol{\sigma \nabla V} - \boldsymbol{J_e}) = \mathbf{0}$$

As such, we can then solve for the scalar electric potential **V** which can then be used to calculate the electric field **E**. The material characteristics for each droplet is listed in **Table 2-3.** The initial conditions and boundaries used for solving the above model are as follows:

- Temperature = 293.15 K
- High voltage electroporation = 200 V
- Ground potential and initial potential V = 0 V

where the high voltage and ground potential were set to the boundaries highlighted in yellow in the **Figure 2-3**. Using these parameters, a stationary study was used to solve for the electric field **E,** and **Figure 3-5** and **Figure 3-7** and shows the simulated electric field **E** within the triDrop structure of different electroporation buffers with different conductivities.

Table 2-3. Electroporation buffer conductivities and relative permitivity.

Material	Characteristic	
	Electrical conductivity (mS/cm)	Relative permitivity
BTXpress	17.7	80
PBS	16	80
Type R buffer	15.6	80
Type T buffer	8.4	80
ISM(m) buffer	7.5	80
Very high conductive solution	32.0	80

2.4 Cell culture

HeLa and HEK293 cells were cultured in Dulbecco's Modified Eagle Medium (DMEM) and Jurkat cells in RPMI-1640 (kindly provided by Prof. Alisa Piekny, Concordia). All media contained 10 % heat-inactivated fetal bovine serum (FBS) and 100 U/mL penicillin/streptomycin. Cells were passaged every 2-3 days and maintained in a humidified chamber at 37 °C with 5% CO_2. For triDrop experiments, HeLa and HEK293 cells were passaged by first washing with PBS, then trypsinizing with 0.25% trypsin-EDTA followed by washing with DMEM before seeding cells in a fresh flask at 2 x 10^5 cells/mL. Jurkat cells were passaged by centrifuging at 300 g for 5 min to pellet the cells, aspirating the media and resuspending in RPMI before seeding at 1 x 10^5 cells/mL. Prior to electroporation, aliquots of 600,000 cells were prepared and resuspended with target molecules in electroporation buffer to a final volume of either 15 µL or 30 µL.

Frozen Primary human CD4+ T cells were either purchased from BPS bioscience (catalog #79752, San Diego, CA) or separated from fresh primary blood and purified using EasySep

Human CD4 T cell Isolation kit (STEMCELL Technologies, Canada, Catalog # 17952) to a purity of 95 %, tested using anti-human CD4 antibodies and anti-human CD3 antibodies (STEMCELL Technologies, Canada, Catalog # 60016AZ and #60011PS) (**Figure 2-4**). All cells were kept in liquid nitrogen prior to use. Cells were thawed and cultured in complete culture medium consisting of RPMI-1640 with 10 % FBS, 100 U/mL penicillin/streptomycin, and 100 IU/mL recombinant human IL-2 (Fisher Scientific Ottawa, ON). After 24 h, the cells were activated with Human T-Activator CD3/CD28 Dynabeads (Fisher Scientific Ottawa, ON, #11131D) and were incubated up to 48 hours. After incubation, activator beads were removed following manufacturers protocol by first gently pipetting up and down to release cells from the activator beads followed by transferring the cells to a magnetic tube rack for 1-2 minutes to allow for cells and beads separation and the supernatant containing cells was transferred to a fresh tube. Primary T cells were counted using TC20 Automated Cell Counter (BioRad, CA) and maintained at 1 x 10^6 cells/mL by daily addition of complete culture media. Prior to electroporation, cell aliquots of 600,000 cells were prepared and resuspended with target molecules with electroporation buffer to a final volume of 15 µL for each unique condition.

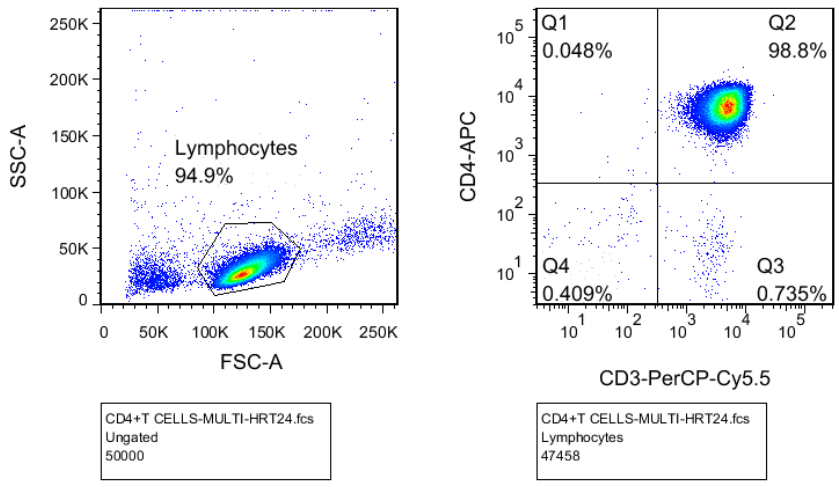

Figure 2-4. Purity of T cell isolation from whole blood.
Isolated cells were stained with tested using anti-human CD4 antibodies and anti-human CD3 antibodies for flow cytometry to analyse its purity for human CD4+ T cells.

2.5 Bulk electroporation

Prior to electroporation, HeLa cells were seeded the day before transfection (day 0) to reach 70-80% confluency by day 1. Immediately before electroporation, adherent cells were trypsinized (using 0.25% trypsin-EDTA), washed, and re-suspended in media, and counted with TC20 Automated Cell Counter (BioRad, CA). The Neon^{TM} transfection system (Thermo Fisher) was then used to electroporate cells using manufacturer's protocol following four steps: (1) cells were centrifuged at 300 g for 3 min and washed with 500 µL PBS before being resuspended 5 x 10^6 cells/mL in the Neon^{TM} electroporation buffer. (2) FITC-tagged dextran molecules were then added to a final concentration of 300 µg/mL. (3) the electroporation sample was mixed (via gentle up-and-down pipetting) and transferred to the Neon^{TM} capillary electroporation tip and were electroporated using the parameters recommended by the manufacturer for HeLa (1005 V, 2 pulse, 35 ms), and (4) immediately after electroporation, cells are placed into a 6 well plate containing 2 mL of pre-warmed culture media for cell recovery. Cells were only maintained in their proprietary electroporation buffer for a maximum duration of 20 min to preserve cell viability.

2.6 TriDrop automation and operation

The bottom plate of the triDrop device was placed on a pogo pin holder that has been propped to a height 20 cm above the benchtop using a chassis constructed from T-slotted aluminum extrusions purchased from McMaster-Carr (catalog #: 47065T101, Aurora, OH) and machined and assembled in-house. The system is connected to a 720 pixel, 30 frames-per-second camera (Skybasic, Houston TX) to visualize droplet movements on the device (**Figure 2-5**). A 12-input card edge connector from Digikey (catalog #: 151-1410-ND, Thief River Falls, MI), was attached to the top plate of the triDrop device and connected via three leads (DMF ground, High

Voltage DC, DC ground). Two DC leads were connected to an electroporation pulse circuit (**Figure 2-5**) and one lead was used to provide the electrical connection for the DMF ground. The electroporation circuit consisted of an 8 pin optocoupler (Model #: AQW216EH) purchased from Digikey was connected to a Z650-0.32-U DC power source (TDK-Lambda) and controlled by an Arduino Uno running a custom pulse generating program, creating custom pulses of varying amplitudes and durations (100 - 450 V_{DC}, 1-10 ms in duration). For automating droplet movement on the device, see our previous published work for circuit and connectivity[104]. The electroporation and DMF actuation circuit were controlled by our in-house software which is available on our bitbucket registry (https://bitbucket.org/shihmicrolab/littleleung_2023). Droplet movements were programmed by application of AC potentials (300 – 400 V_{RMS}) at 15 kHz between the top and bottom plates. The DMF actuation software was also used to initiate the electroporation pulse circuitry to ensure immediate and uniform pulse application after triDrop merging.

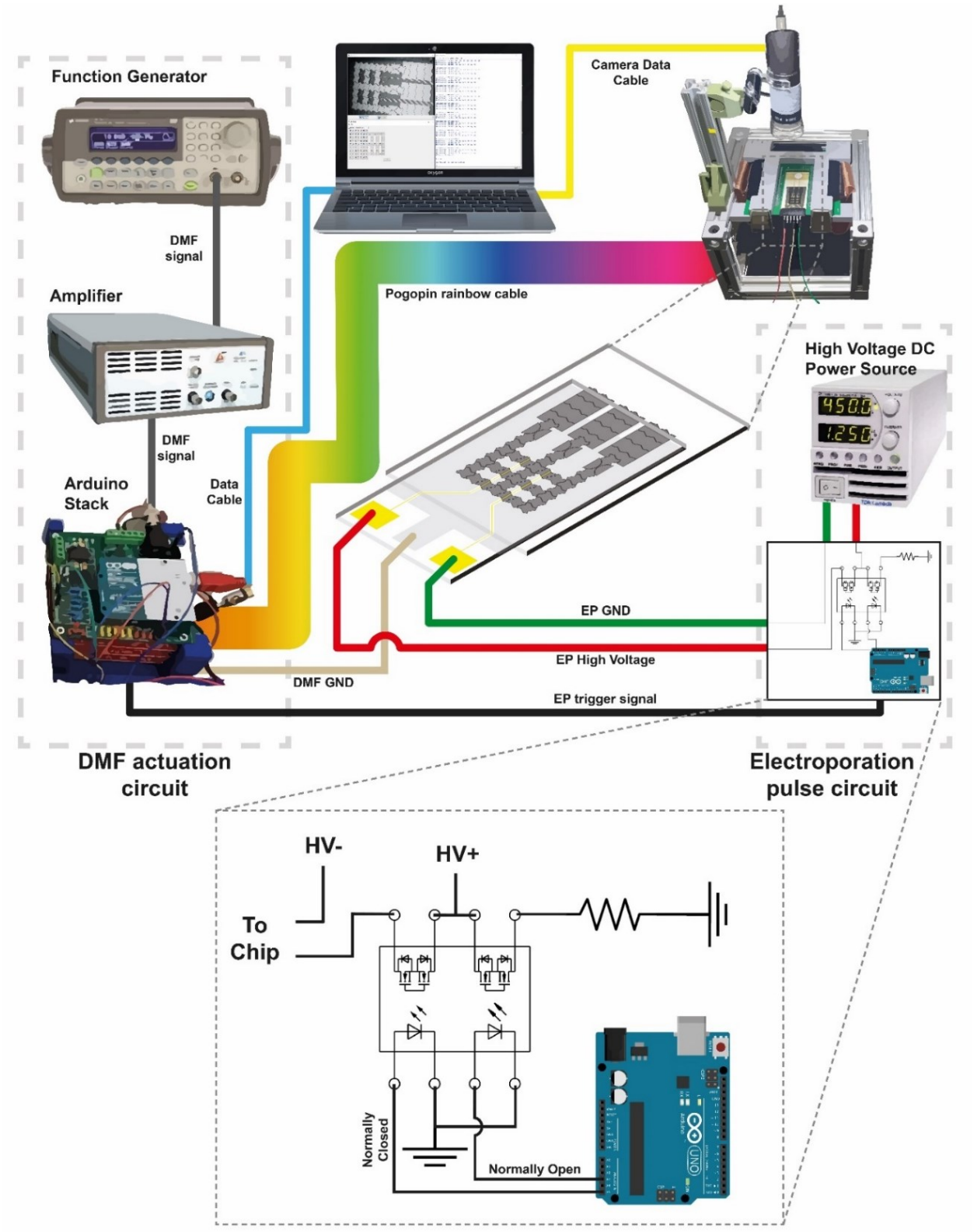

Figure 2-5. DMF System overview.
Schematic overview of the complete triDrop automation setup detailing the DMF actuation hardware, automated electroporation pulse generation circuit, and chip holder.

2.7 TriDrop electroporation

Prior to a triDrop experiment, HEK293, HeLa, Jurkat, and primary T-cells were centrifuged at 300 g for 3 min, washed twice with a custom 1SM buffer, and resuspended in Type T electroporation buffer. For experiments using dextran molecules, cells and dextran molecules were prepared at a final concentration of 2 x 10^7 cells/mL and 0.03 ng/cell respectively. For experiments with eGFP plasmid or mRNA, the payload was added to the cell sample to achieve a concentration of 1.275 pg/cell and 2 pg/cell respectively, with a final cell concentration of 4 x 10^7 cells/mL. For β2M CRISPR knock-out experiments, 60 pmol of sgRNA (targeting sequence: ACTCACGCTGGATAGCCTCC) and 30 pmol of Cas9 was mixed and incubated at room temperature for 10 minutes to allow for the formation of Cas9 RNP. The Cas9 RNP was then immediately used or stored on ice until use, where it was then added to 600,000 cells in electroporation buffer for a final volume of 15 µL.

TriDrop operation included four droplet operations and were implemented using the triDrop automation system described previously. The four steps included: (1) reservoir filling, (2) triDrop dispensing, (3) triDrop merging, and (4) triDrop electroporation. Droplet operation can be visualized in **Figure 3-1b** and **Supplementary Video - link**. The device consisted of three reservoirs: two outer reservoirs were filled with PBS containing 0.05 % Pluronics F-68 (which we refer to as high conductivity buffer, σ ~ 16 mS/cm) and the middle reservoir was filled with cells and the desired payload suspended in electroporation buffer containing 0.05 % Pluronics F68 surfactant. Reservoirs were filled by pipetting 6 µL each onto the bottom plate at the edge of the top plate and applying driving potentials to the three reservoir electrodes to draw the fluids into the reservoir. Next, ~1 µL single droplet was dispensed from each reservoir by pulling and necking the liquid out of the reservoir using a modified droplet dispensing system[147]. The cell

containing droplet was actuated to the center of the electroporation site and the two high conductive droplets dispensed droplets were actuated to the outer edges of the electroporation site. The three droplets were merged by actuating the high conductive droplets towards the cell containing droplet creating a continuous three droplet structure. Immediately upon merging, the electroporation circuit was automatically triggered to deliver a sequence of high voltage DC square-wave pulses to the exposed Au-electrodes (on the top plate) that were in direct contact with the PBS droplets (see **Table 2-4** for triDrop electroporation parameters). For experiments using the uniform electroporation arrangement, all three reservoirs contained the same media with cells and payload suspended in either electroporation buffer or PBS with 0.05 % Pluronics F-68 surfactant. For experiments using the focused electroporation arrangement, all three reservoirs contain the same media (either electroporation buffer or PBS with 0.05 % Pluronics F68 surfactant), however only the middle reservoir contains cells and payload.

Immediately after triDrop electroporation, the top plate is removed, and the electroporated cells (total volume ~ 3 μL) were immediately removed from the chip via pipetting and placed in a well plate that was pre-loaded with warmed culture media. HEK293 and HeLa cells were cultured in flat bottom 48 well plates post electroporation for cell recovery. Jurkat and Primary T cells were cultured in a U-bottom 96 well plate post electroporation for cell recovery. All experiments with cells were incubated at a maximum time of 20 minutes in electroporation buffer to preserve optimal cell health.

Table 2-4. Electroporation parameters, cell densities, and required concentrations used for different cell lines and payloads

Cell type	Payloads	Concentration	Pulse Number	Pulse Duration	Cell density (cells/ml)	Voltage (V)	Electric field (kV/cm)
HEK293	• 70kDa FITC-Dextran • 250kDa FITC-Dextran • 2000kDa FITC-Dextran • 5 kb eGFP-plasmid	1.2 µg / µl 51 ng / µl	3	10 ms	$2x10^7$ $4x10^7$	225	0.57
HeLa	• 70kDa FITC-Dextran • 250kDa FITC-Dextran • 2000kDa FITC-Dextran • 5 kb eGFP-plasmid	1.2 µg / µl 51 ng / µl	3	10 ms	$2x10^7$ $4x10^7$	350	0.88
Jurkat	• 70kDa FITC-Dextran • 250kDa FITC-Dextran • 2000kDa FITC-Dextran • 1 kb eGFP-mRNA • 5 kb eGFP-plasmid • Cas9 RNP	1.2 µg / µl 0.08 µg / µl 51 ng / µl 2 pmol / µl	3	5 ms	$4x10^7$	350	0.88
Primary T cells	• 2000kDa FITC-Dextran • 1 kb eGFP-mRNA • 5 kb eGFP-plasmid	1.2 µg / µl 0.08 µg / µl 51 ng / µl	3	3 ms	$4x10^7$	450	1.13

2.8 pH measurements

Following previously established methods for analyzing pH change in microfluidic electroporators[48], DMF reservoirs were loaded with either high conductivity buffer (flanking reservoirs) or low conductivity media with HEK293 cells at a concentration of 2 x 10^7 cells/mL (middle reservoir) containing either phenolphthalein or Congo red to test the pH changes above 9.0 and between 3 – 5.2, respectively. The triDrop structure was formed following the procedure described above and 3, 200 V pulses 10 ms in duration were applied. Images of the droplets were taken every 1 s for 30 s using a wireless digital microscope (Skybasic, Houston, TX) to monitor colour changes in the middle droplet.

2.9 Current measurements

Electrical current was measured by placing a 100 Ω shunt resistor in series and downstream of the triDrop top plate. An oscilloscope was connected across the shunt resistor and the voltage peak was recorded across the resistor during an application of the electric potential (after forming the triDrop structure). The system current was determined using the Ohm's law relationship ($I_{measured} = V_{peak}/100\ \Omega$).

2.10 Flow cytometry

Viability, transfection efficiency (TE) and mean fluorescent intensity (MFI) were measured using a BD FACS Melody (BD Bioscience, Canada). The FACS was equipped with three excitation lasers (405 nm, 488 nm, 561 nm) in a 2B-2V-4YG configuration. For all experiments with dextran molecules, plasmids, or mRNA, cells were resuspended in 500 µL of culture media, washed by centrifuging (300 g, 5 min), and then resuspending in 1 mL FACS buffer (1x PBS, 1 mM EDTA, 25 mM HEPES, 1 % FBS, pH 7.0), then centrifuged (300 g, 5 min), aspirated, and resuspended in 600 µL of FACS buffer. For all samples, viability was assessed by staining dead

cells using 0.6 µL of DAPI (50 ng/µL) added to the sample immediately prior to FACS and mixed thoroughly with the sample by pipetting. Dextran, plasmids, and mRNA were excited by a 488 nm laser and viewed through a 527/32 filter. DAPI was used as an indicator for dead cells and was excited by a 405 nm laser. Our gating protocol is shown in **Figure 2-6**. Briefly, a non-electroporated control containing payload was prepared using the above method and loaded into the FACS machine. First, the data was analyzed comparing forward scatter and side scatter to identify which data points are cells. Next, the cell population was analyzed comparing side scatter height and side scatter width to identify singlets. Once singlets were identified, a histogram plot was generated for DAPI staining - separating living cells (DAPI negative) from dead cells (DAPI positive). Finally, the living cell population was used to generate a histogram showing FITC expression and this histogram was used to define the lower boundary of transfection with the gate being set to include ~1 % of the control population as transfected to account for endocytosis. For each condition, 15,000 events were collected at a rate of 100 events/s.

For CRISPR gene knockout experiments, cells were maintained in culture for 72 hours post-electroporation. Following maintenance, the cells were centrifuged (300 g, 5 min) and resuspended in 50 µL of culture media. 48 µL of culture media and 2 µL of Human TruStain FcX™ (Fc Receptor Blocking Solution, BioLegend catalog #: 422301) were mixed to prevent non-specific binding followed by 5 minutes of incubation at room temperature. After blocking, cells were spun down at 300 g for 5 minutes with the supernatant removed, resuspended in 98 µL of culture media plus 2 µL of FITC anti-human HLA-A,B,C Antibody (BioLegend catalog #: 311403) and incubated for an additional 20 minutes in the dark at 4 °C. After staining, the cells were then washed twice in 1 mL of FACS buffer, centrifuged (300 g, 5 min) to remove the

supernatant, and resuspended in 600 µL of FACS buffer. Similar to above, FACS gates are determined by running a non-electroporated control to define normal β2M expression and electroporated samples are compared against the control.

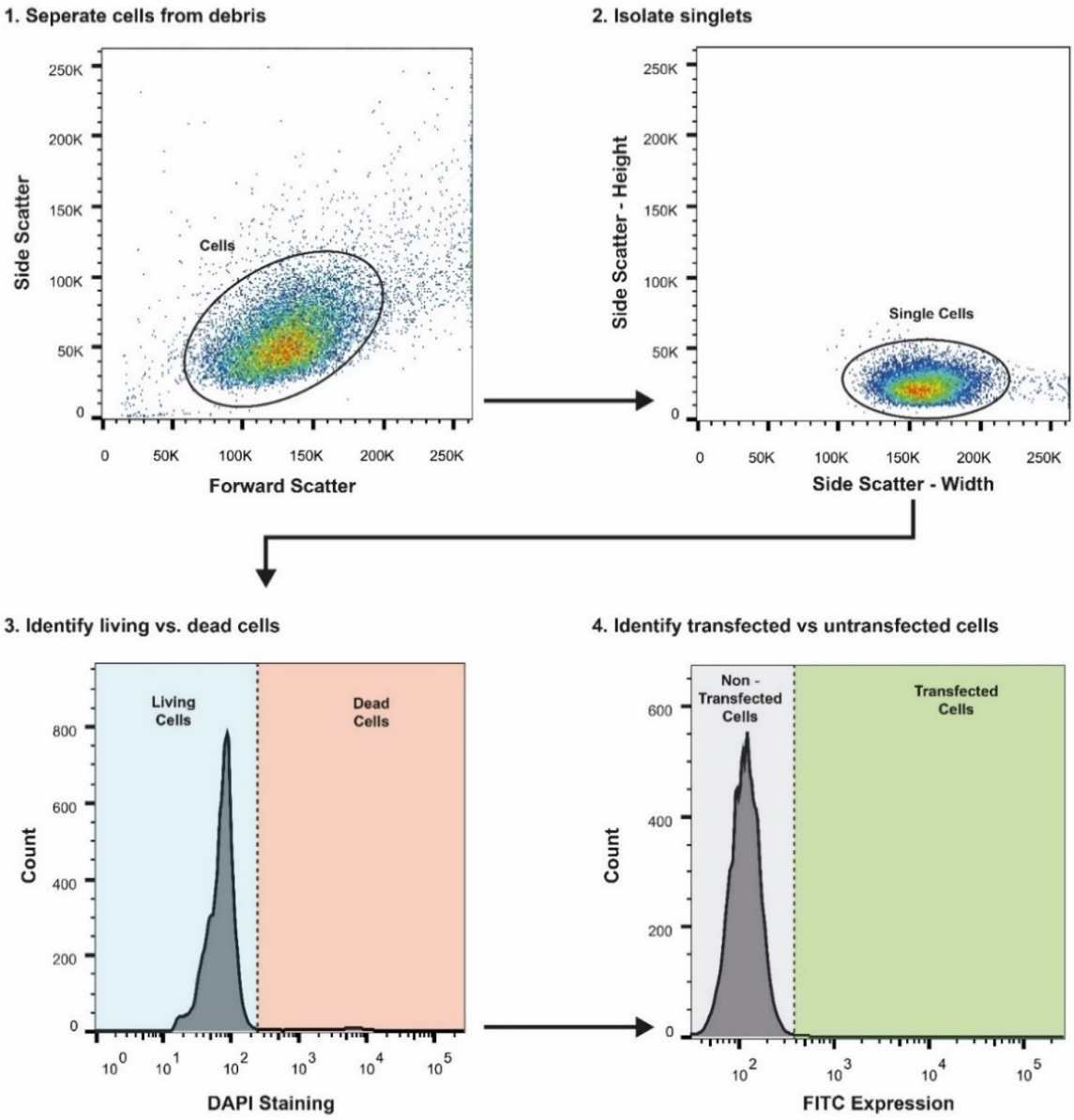

Figure 2-6. Flow cytometry gating workflow.
A non-electroporated sample mixed with the prospective payload is used to define gating. First, cells are separated from debris. Next, single cells are isolated from doublets. This is followed by identifying live/dead cells which are determined with DAPI staining. Finally, successfully electroporated living cells are identified.

2.11 Post-electroporation analysis

FACS data was analyzed using FlowJo (Ashland, OR). After gating out the doublets and cell debris, the viability was measured as the percentage of living cells (DAPI negative) from a sample. The viability ratio (VR) was then calculated as the ratio of the viability of electroporated sample to the non-electroporated cells (i.e., control).

Equation 2-3. Viability Ratio (VR) equation.

$$\boldsymbol{VR = \frac{Viability_{electroporated}}{Viability_{Unelectroporated}}}$$

Transfection efficiency was calculated as the number of fluorescent living cells above the threshold divided by the total number of living cells.

Equation 2-4. Transfection Efficiency (TE) equation.

$$TE = \frac{number\ of\ transfected\ living\ cells}{total\ number\ of\ living\ cells}$$

The background fluorescence of the cells was defined by using samples with cells only with no electroporation.

Mean fluorescence intensity fold-change was calculated by measuring the mean fluorescent intensity for non-transfected control cells as shown previously[115].

Equation 2-5. Mean Fluorescence Intensity (MFI) fold-change equation.

$$MFI\ fold-change = \frac{MFI_{transfected\ cells}}{MFI_{untransfected\ cells}}$$

Relative cell increase was calculated by dividing the cell count on each day post-electroporation by the cell count from day 1 post-electroporation. The cell count was calculated

by measuring the cell centration using T20 Automated Cell Counter (BioRad, CA) and the volume of culture medium in each well.

For visual analysis, 48 hours post electroporation, bright field and fluorescent images were taken a with 20x objective on an Olympus IX73 inverted microscope (Olympus Canada, Mississauga, ON, Canada) and a 100x objective on a Zeiss Axio Observer 7 with an excitation wavelength of 480 nm and a 470/40 nm excitation and 525/50 nm emission filter set (catalog # 49002, Chroma Technology Corporation, Bellows Falls, VT). The brightness and contrast of images were adjusted using ImageJ.

2.12 Statistical Analysis

Statistical analysis was performed using an ordinary one-way ANOVA with Prism V8.4 (Graphpad) with n = 3 replicates for **Figure 3-4** and **Figure 3-6**. For **Figure 3-4**, we obtained a F-value of 13.7, 20.73, and 6.4 for transfection efficiency, viability ratio, and mean fluorescence intensity, respectively with a Dfn of 4 and Dfd of 10. For **Figure 3-6**, we obtained a F-value of 97.23, 4.08, and 11.36 for transfection efficiency, viability ratio, and mean fluorescence intensity, respectively with a Dfn of 3 and Dfd of 8.

Chapter 3 Results and Discussion

This chapter consists of my results and discussion from my experimental data. We introduce the device operation and the workflow followed by the three steps were involved in developing the triDrop system. First, the device was designed and characterized using numerical simulations and validated using delivery of dextran molecules into HEK293 cells. Next, further validation was done by delivering a wide range of target molecules into a range of immortalized cell lines. Lastly, we show a gene knockout experiments into Jurkat cells and successful delivery of large biological cargo into human primary T cells with post-electroporation cell viabilities similar to that of control.

3.1 TriDrop electroporation using digital microfluidics

TriDrop is a method that allows for mammalian cell electroporation on digital microfluidic devices. It is a method that involves merging three equal volume droplets into a sequential chain using DMF actuation. By applying a voltage across the droplet chain, an electric field can be generated throughout the chain that allows for the safe and effective delivery of biological payloads into mammalian cells. Electroporation has been shown previously on DMF platforms for the transformation of microbial cells[132,136], however, we show for the first time the ability to perform electroporation of immortalized and primary mammalian cells on a DMF platform. This opens the possibility for integrating our electroporation system with other DMF devices to allow for end-to-end automation of mammalian cell engineering similar to what has been shown previously for microbial cells[144,145]. Moreover, our platform can work with low quantities of mammalian cells, which has recently become a significant interest in the field of genome editing. For instance, cell-based immunotherapies require inactivated primary T-cells[125] or natural killer cells or more rare immune cells such as tumor infiltrating leukocytes[126] (TILs), or gamma-delta T cells[127] which are challenging to recover and to expand[128]. Currently, commercial platforms

for primary T cell electroporation (e.g., Neon, Lonza, Celetrix) require at least 200,000 cells per condition for efficient insertion, and optimized protocols for working with primary immune cells have shown that using fewer cells has a detrimental effect on viability and efficiency with at least 1-2 million cells per condition being optimal[28,130].

A workflow for electroporating 20,000 - 40,000 mammalian cells using the triDrop system consisted of: sample preparation and collection which includes preparing immortalized cell lines or primary cells extracted from a patient, resuspension of the cells in electroporation buffer to a concentration of at least 2 x 10^7 cells/mL along with the desired payload and then loading them into the reservoirs of the DMF device (**Figure 3-1a**). The triDrop instrument is comprised of multiple components (**Figure 2-5**): the DMF device for the droplet manipulations, our imaging setup for visualizing the droplets on the device, an electroporation pulse circuit, and a DMF actuation circuit with open-source code (see BitBucket registry in Methods). The DMF device is comprised of two plates: the bottom plate, which contains the reservoir and driving electrodes to create the triDrop structure and the top plate, which contains Au-lines for applying the electroporation pulses to the triDrop structure as well as the grounding plane for the DMF driving voltage. The droplets sandwiched between the plates are comprised of either high, or low conductivity buffer containing mammalian cells and various payloads for delivery. Once the samples are loaded, the triDrop structure can be formed easily using our previously shown DMF platform[104,148] which allows for complete automation of all dispensing, actuation, and merging as well as automating the application of programmable high voltage pulses for electroporation.

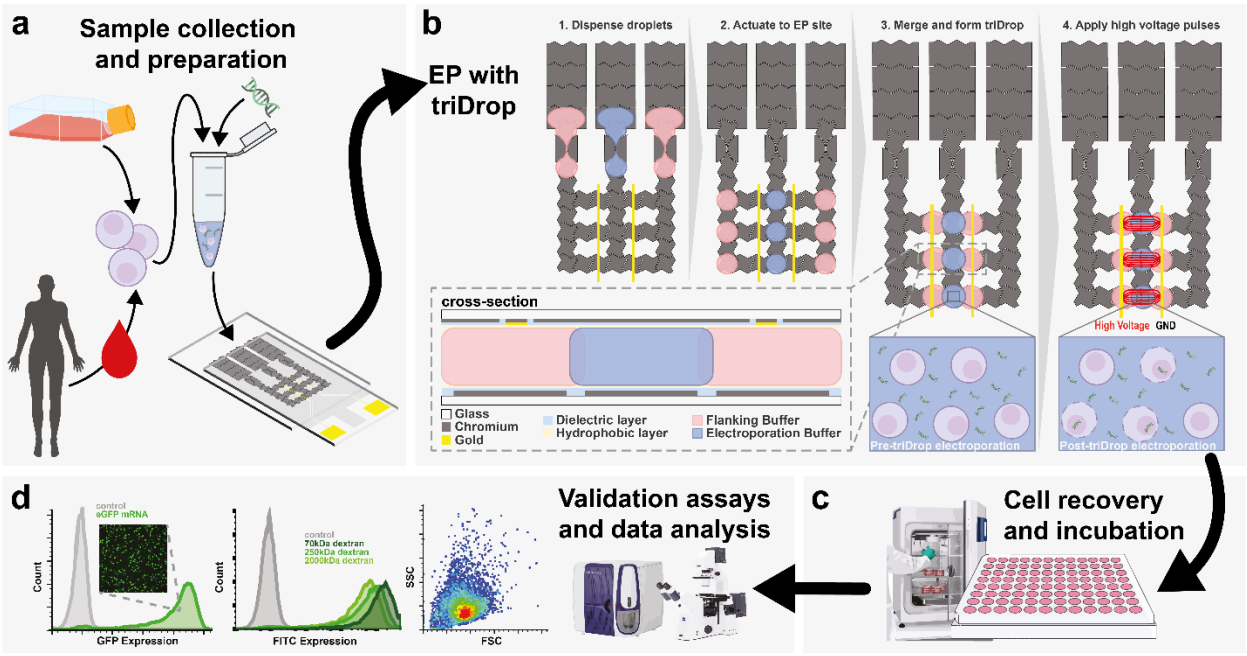

Figure 3-1. TriDrop platform design and overall experimental workflow for genetically engineering cells with the triDrop system.
(a) Cell sample was cultured and prepared by resuspending it in electroporation buffer with target delivery molecules. (b) The schematic illustration shows top-view of the DMF device and the formation of the triDrop through a series of electrode actuations. The red lines (in frame 4) indicate the electric field lines generated during application of high voltage pulses. The inset shows the cross-sectional view of the triDrop. (c) After electroporation, samples were then incubated (> 24 h) for cell recovery and followed by (d) analysis using FACS or with fluorescent microscopy or any analytical method of interest.

The process of triDrop electroporation is shown in **Figure 3-1b**. A key feature of the system is the use of low cell numbers – users can input a low number of cells ranging from 20,000 to 40,000 cells per reaction for efficient transfection. Upon inputting into cells into the reservoirs, three 1 µL droplets were dispensed, actuated to an electroporation site, and merged into a sequential chain as shown in **Figure 3-1b** (hereby referred to as the triDrop structure). Within the triDrop structure, the inner droplet (hereby referred to as the sample droplet) was comprised of low conductivity media ($\sigma \sim 8$ mS/cm) and contained mammalian cells in suspension along with the payload to be delivered into the cells (in our work, the payloads used are dextran molecules of various sizes, mRNA, plasmids, or Cas9 proteins). The outer droplets (hereby referred to as the liquid electrodes) were comprised of high conductive media ($\sigma \sim 16$

mS/cm) and were in contact with gold electrodes fabricated into the device top plate and provide an electrical connection between the metal electrodes and the sample droplet, similar to forming a liquid electroporation cuvette. After merging the three droplets into the triDrop structure, mixing was limited to diffusion and the structure consisted of three discrete regions for over 30 s post merge (**Figure 3-2a**), which allowed time for delivering high voltage pulses to the gold electrodes and electroporating the cells. The electroporation process was complete within 5 s of droplet merging and the total time for triDrop implementation from reservoir loading to electroporation was ~3 minutes for three triDrop structures (**Figure 3-1b** and **Supplementary Video - link**). Immediately after electroporation, cells were loaded off chip for post-electroporation culture for up to 7 days (**Figure 3-1c)** and were analyzed using microscopy, flow cytometry and validated with fluorescent-based assays (**Figure 3-1d**). To our knowledge, the triDrop system is the first technique shown for scalable mammalian cell electroporation on DMF devices and joins a small collection of microfluidic devices capable of transfecting primary human immune cells[56,115–118,120,149–154]. Furthermore, we show state-of-the-art transfection efficiency with exceptional viability throughout.

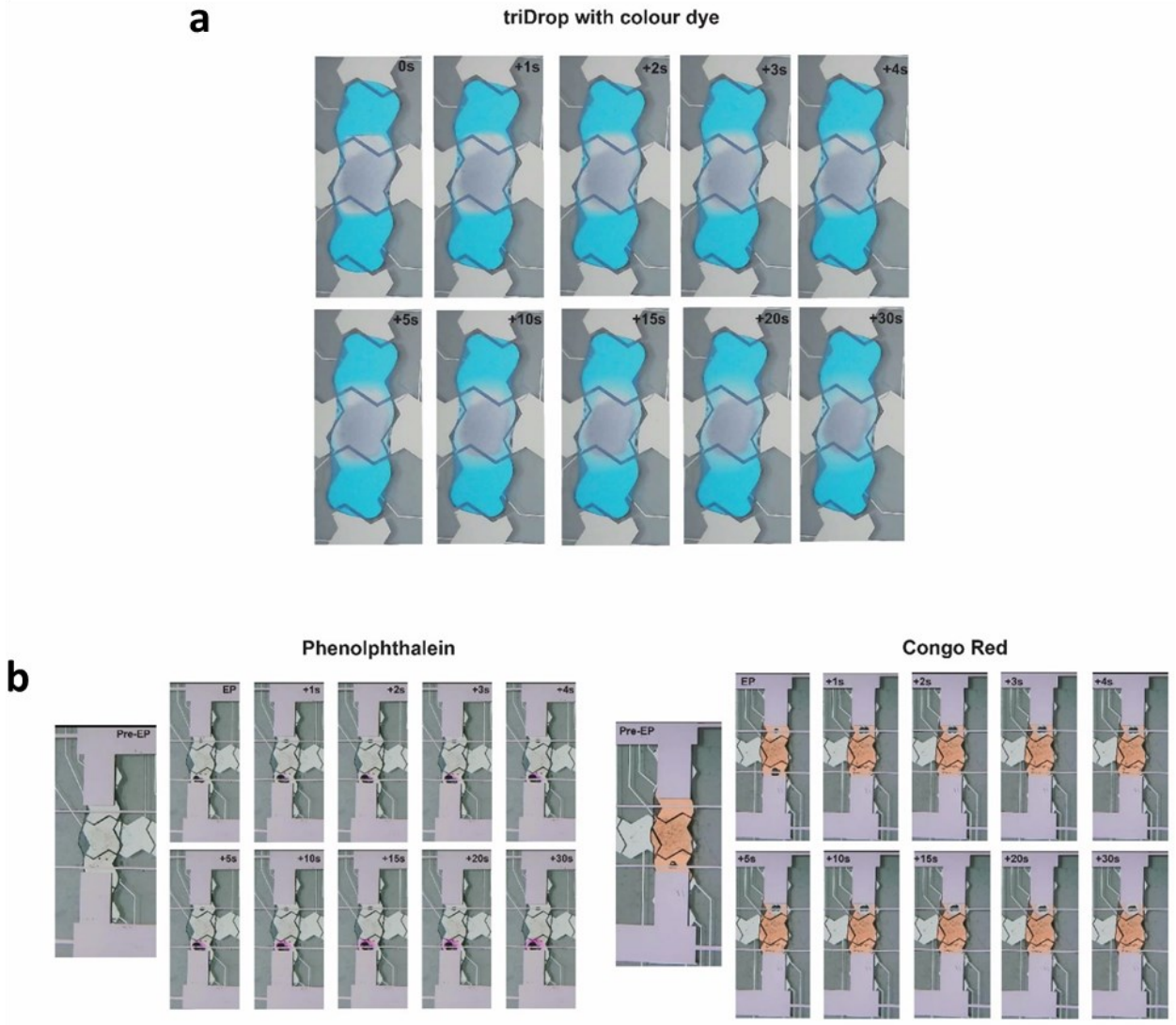

Figure 3-2. triDrop merge and pH change.
(a) A triDrop merge operation performed using a standard bottom plate and a transparent Indium Tin Oxide top plate to help visualize liquid mixing. The outer droplets are comprised of high conductive media with 0.05% Pluronics F68 surfactant along with blue dye. The middle droplet is comprised of low conductive media with 0.05% Pluronics F68 surfactant and 4 x 10^7 cells/mL. Droplets are mixed using standard techniques and left to mix via diffusion for 30 s. (b) A triDrop electroporation procedure using a modified top plate allowing for visualization of the triDrop structure. All three droplets are either doped with phenolphthalein (pH indicator turning purple in the presence of pH above 8.5, left image set), or Congo red (pH indicator turning from red to blue at pH below 5.2, right image set). Three, 200 V_{DC}, 10 ms pulses are applied and the structure was observed for 30 s. The time stamp for each image is shown on the image.

3.2 Characterization of the triDrop system

In initial experiments, we explored the use of co-planar electrodes paired with various droplet structures to generate a sufficient electric field to insert 70 kDa FITC-tagged dextran into the easy to transfect HEK293 cell line. The droplet structures tested here are shown in **Figure 3-4a** and described as follows: (1) a uniform structure – one homogenous 3 μL droplet comprised of either high or low conductivity medium with the cells and payload distributed homogenously throughout, (2) a focused structure – three 1 μL droplets comprised of the same media that are merged together with only the middle droplet containing cells and payload, and (3) a triDrop structure – two droplets of high conductivity buffer flanking a droplet with low conductivity buffer containing cells and payload. Three, 200 V_{DC} pulses, 10 ms in duration (determined via numerical simulation outlined in **section 2.3**) were applied to the droplet structures and the results were analyzed using three metrics, transfection efficiency (TE), viability ratio (VR), and mean fluorescence intensity (MFI) fold change. **Figure 3-4b** shows that the triDrop structure has significantly higher TE (89%) and MFI fold change (79) than any of the other droplet structures while still maintaining a viability ratio of > 90 % ($P < 0.05$, $n = 3$). Additionally, we show that the success of the triDrop structure can be recreated without significant difference when the middle droplet is comprised of another low conductivity electroporation buffer (1SM(m), $\sigma \sim 7.4$ mS/cm) but not when using high conductivity electroporation buffers ($\sigma > 15$ mS/cm) (**Figure 3-6**).

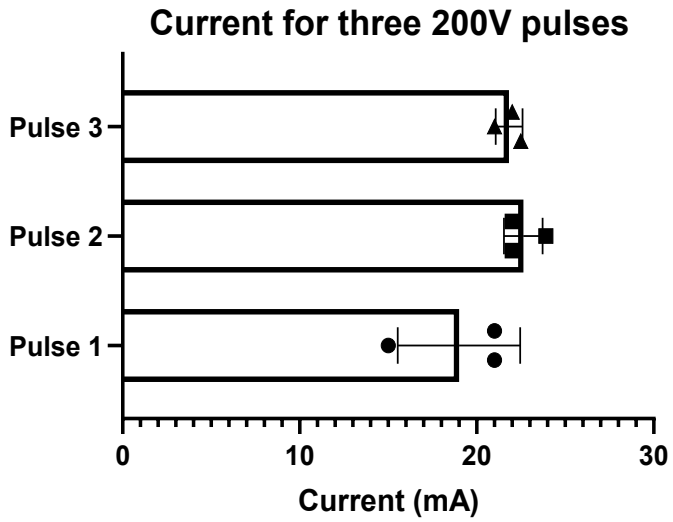

Figure 3-3. Current measurements for all three pulses during a standard triDrop EP process.
Three, 200 V_{DC} pulses, 10 ms in duration were applied to a triDrop structure containing 2 x 10^7 cells/mL. Error bars are based on standard error of the mean for n = 3 replicates.

To understand the experimental results above, we developed a COMSOL simulation of the uniform and triDrop structure described in the Methods section, and the results are shown in **Figure 3-5** and **Figure 3-7**. The simulation of the uniform structure shows the outer regions of the structure experience electric fields that are low for mammalian electroporation (< 0.2 kV/cm)[155], regions close to the gold electrodes have a high but inconsistent electric field (~0.7 kV/cm), and the middle section of the droplet structure has a homogenous electric field that is too low for electroporation (0.35 kV/cm). Comparing this to the simulation of the triDrop structure shown in **Figure 3-4** and **Figure 3-5**, forming the outer droplets using high conductive media and the inner droplet using low conductivity media results in a homogenous electric field (0.55 kV/cm) that focuses across the middle of the structure. In this configuration, all the cells (which are entirely located in the middle droplet) experience a consistent electric field while being exposed to significantly lower current than current benchtop systems (~30 mA vs ~3000 mA)[142] (**Figure 3-3**).

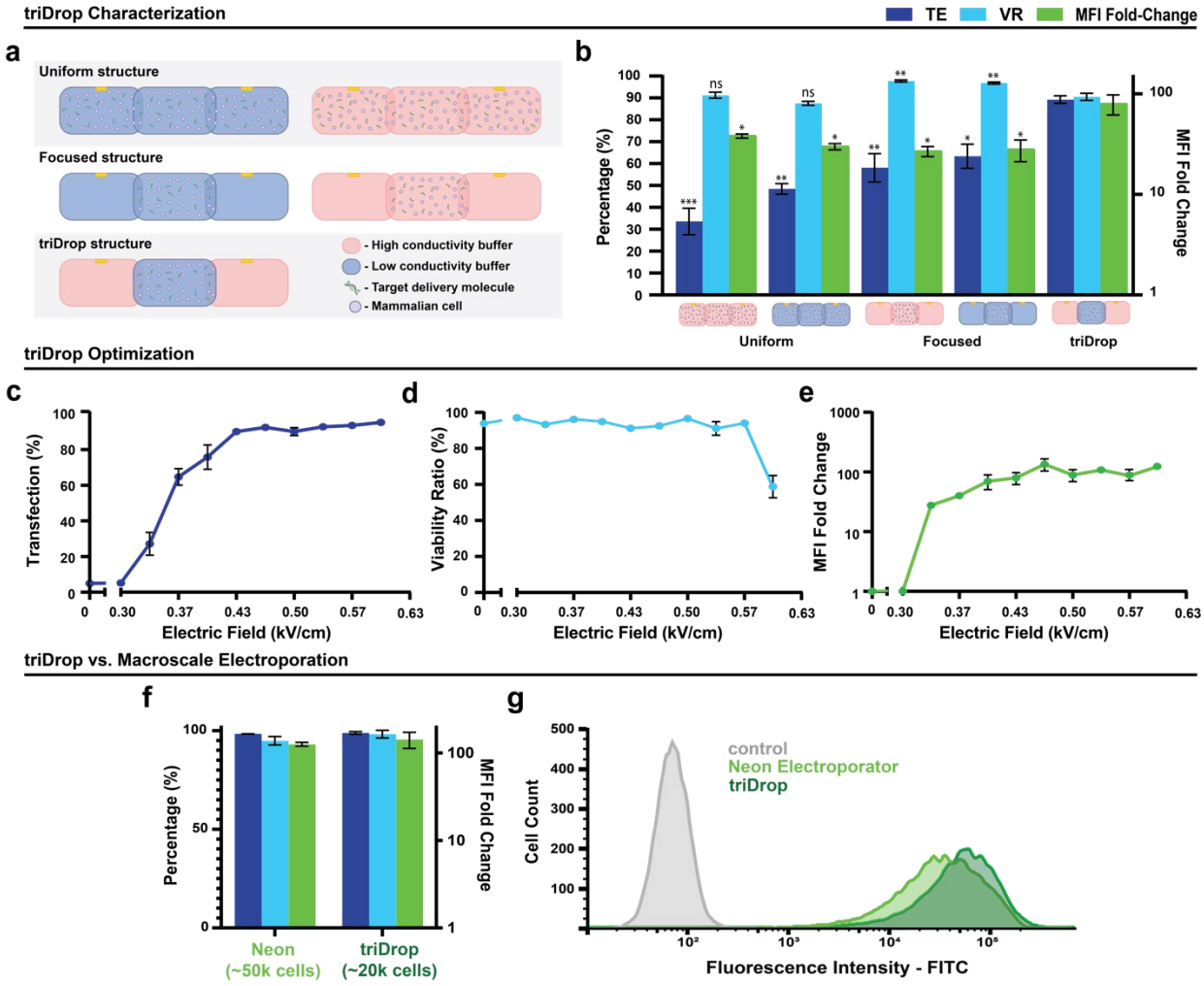

Figure 3-4. System characterization and optimization for triDrop EP with HEK293 cells.
(a) Illustrations showing different droplet liquid structures used for electroporation characterization. Pink droplets represented high conductivity media (σ ~ 16 mS/cm) and blue droplets represent low conductivity media (σ ~ 8 mS/cm). (b) Plots showing transfection efficiency (TE; dark blue), viability ratio (VR; light blue) and mean fluorescence intensity (MFI) fold-change (green) for five different droplet electroporation structures when inserting a 70 kDa FITC-tagged dextran molecule. Significance markers ($P < 0.05$, $n = 3$) are in reference to the triDrop arrangement. Plots showing the (c) transfection efficiency, (d) viability ratio, and (e) MFI fold-change with respect to the applied electric field using the triDrop system for the insertion of 70kDa FITC-tagged dextran molecule into HEK293 cells. The statistical analysis was performed via an ordinary one-way ANOVA ($n = 3$). Graphical representation showing the (f) efficiency, viability ratio, and MFI fold-change for the Neon (standard) versus the triDrop system. These quantitative values were obtained from (g) the cell counts displaying FITC fluorescence from electroporated and non-electroporated samples from the Neon system and the triDrop. SEM are calculated based of $n = 3$. n.s indicated no significant difference, *, **, and *** represents P-values below 0.05, 0.01, and 0.001 respectively. Statistical analysis was performed using an ordinary one-way ANOVA.

This is an important result because isolating the cells in the middle of the droplet structure will prevent harmful electrochemical species (generated at the metal-liquid interface[58,138]) from changing the pH of the cell media and negatively affecting the health of the cells (see images of pH test in **Figure 3-2b**). Given these observations, the triDrop structure offers optimal results compared to the uniform or focused liquid structures when using identical electroporating conditions. The triDrop structure was replicated and used in the remaining electroporation experiments.

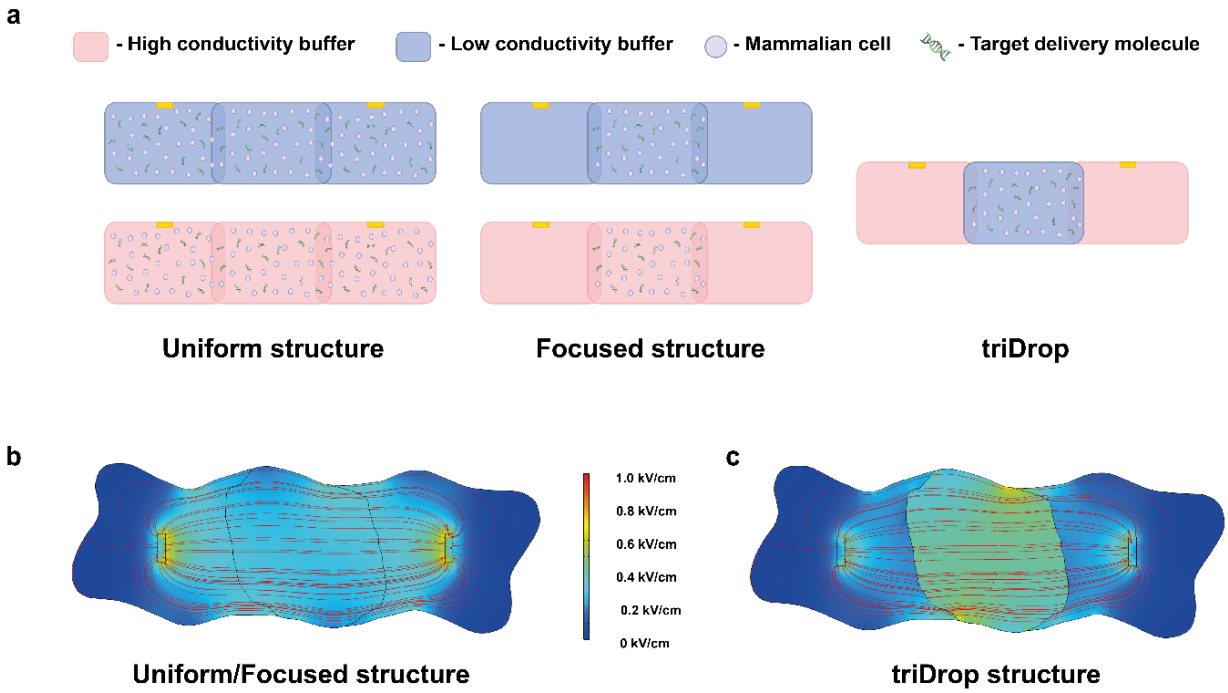

Figure 3-5. Overview of coplanar DMF electroporation designs**.**
(a) Schematic representation of the 3 different electroporation structures investigated for effective DMF electroporation. (b) COMSOL simulations of the droplet structures when applying a 200V pulse.

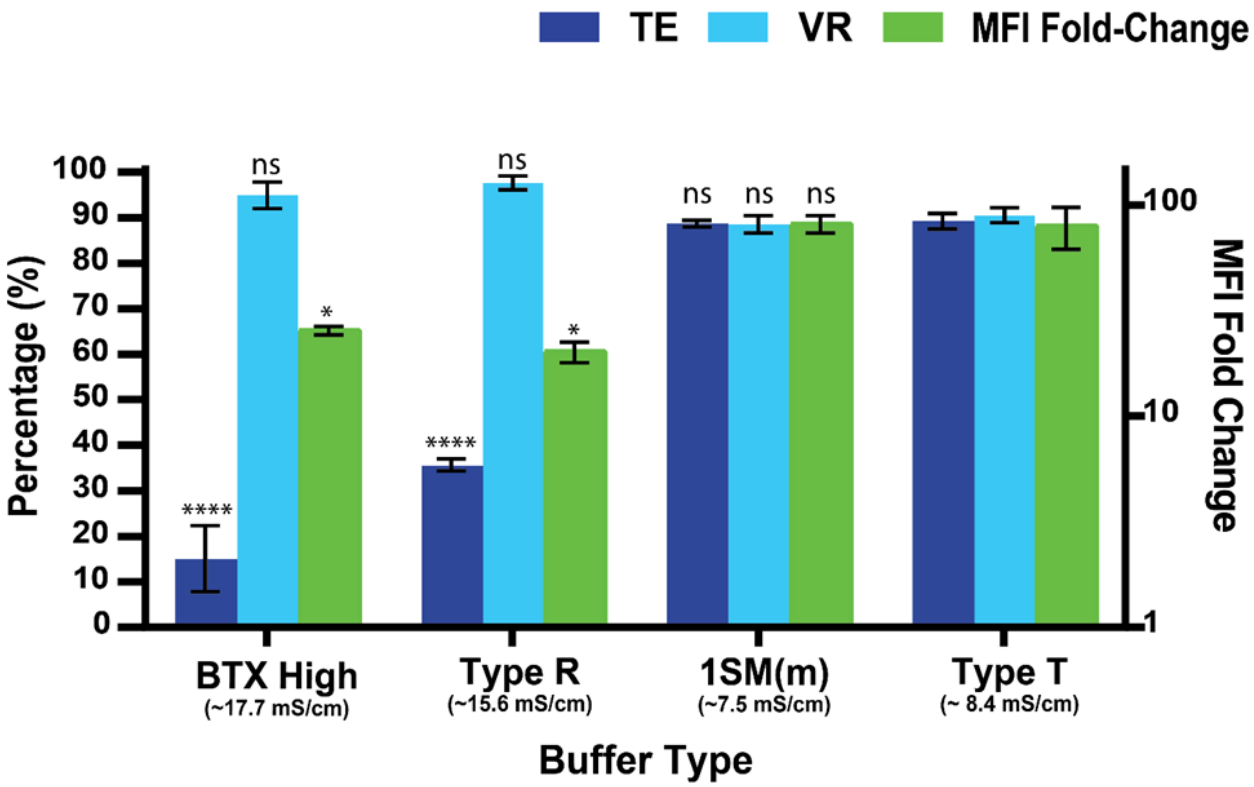

Figure 3-6. Middle droplet buffer vs triDrop electroporation.
Bar graph comparing triDrop electroporation to insert 70kDa FITC-tagged dextran into HEK293 cells using four different electroporation buffers to form the middle droplet. For each condition three 200 V_{DC} pulses, 10 ms in duration were applied. The outer droplets were comprised of high conductivity media and the middle droplets had cells at 2 x 10^7 cells/mL. SEM are calculated based of n = 3. n.s indicated no significant difference, *, **, and *** represents P-values below 0.05, 0.01, and 0.001 respectively. Statistical analysis was performed using an ordinary one-way ANOVA.

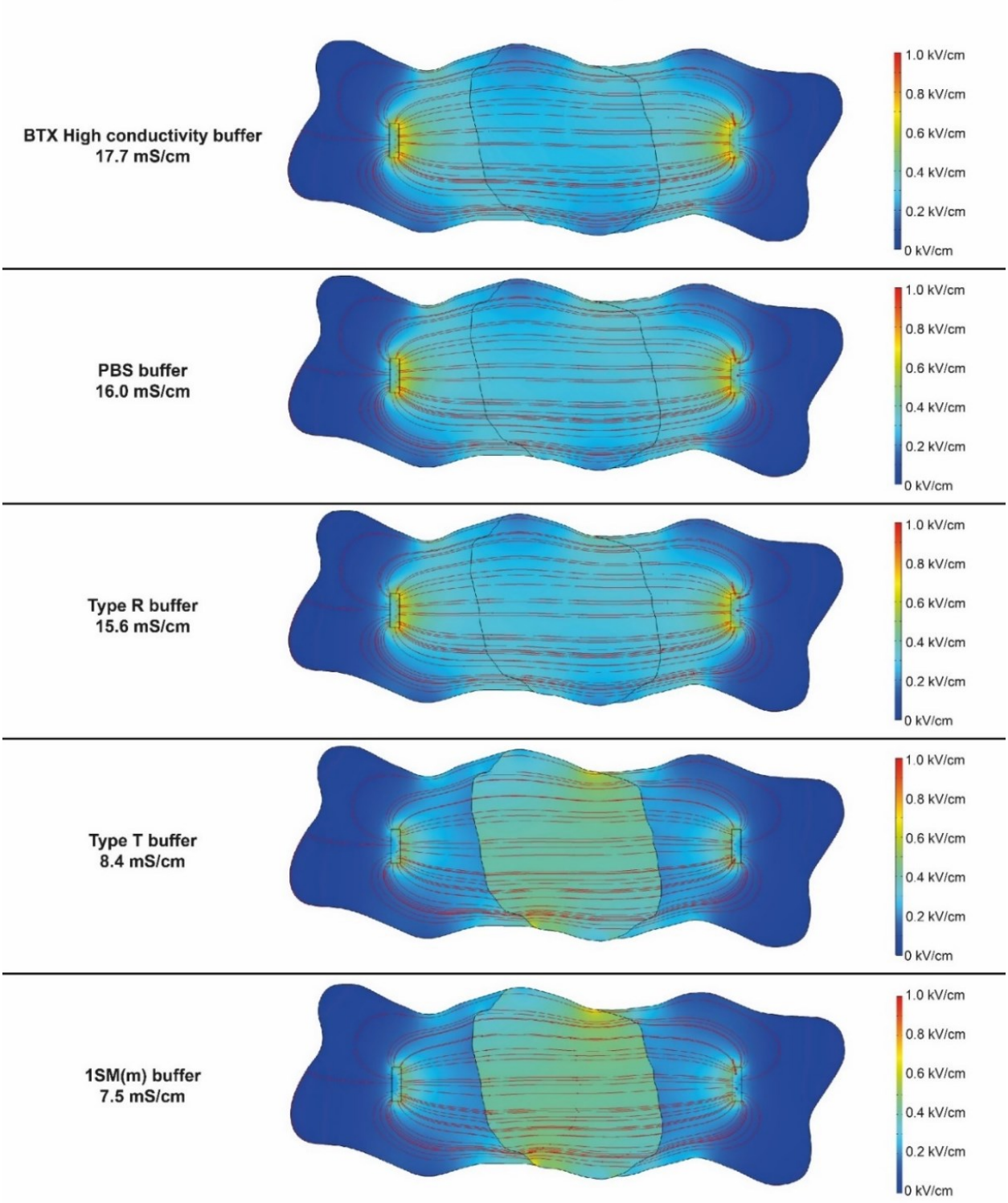

Figure 3-7. Numerical simulations of various electroporation buffers**.**
COMSOL simulations showing the electric field generated inside of a triDrop structure when forming the middle droplet out of buffers with different conductivities.

We hypothesized that the three quantitative metrics (TE, VR, and MFI-fold change) for the triDrop structure might be improved by varying the applied electric field. To test this hypothesis, a range of electric fields were applied to determine the optimal field for inserting 70 kDa FITC tagged dextran molecules into HEK293 cells. These data, shown as line graphs in **Figure 3-4c-e**, confirm that there is range of fields (0.5-0.63 kV/cm) to achieve excellent TE (~ 90 %), VR (~ 90 %), and MFI fold change (> 80). Repeating this optimization for Jurkat and HeLa cells (

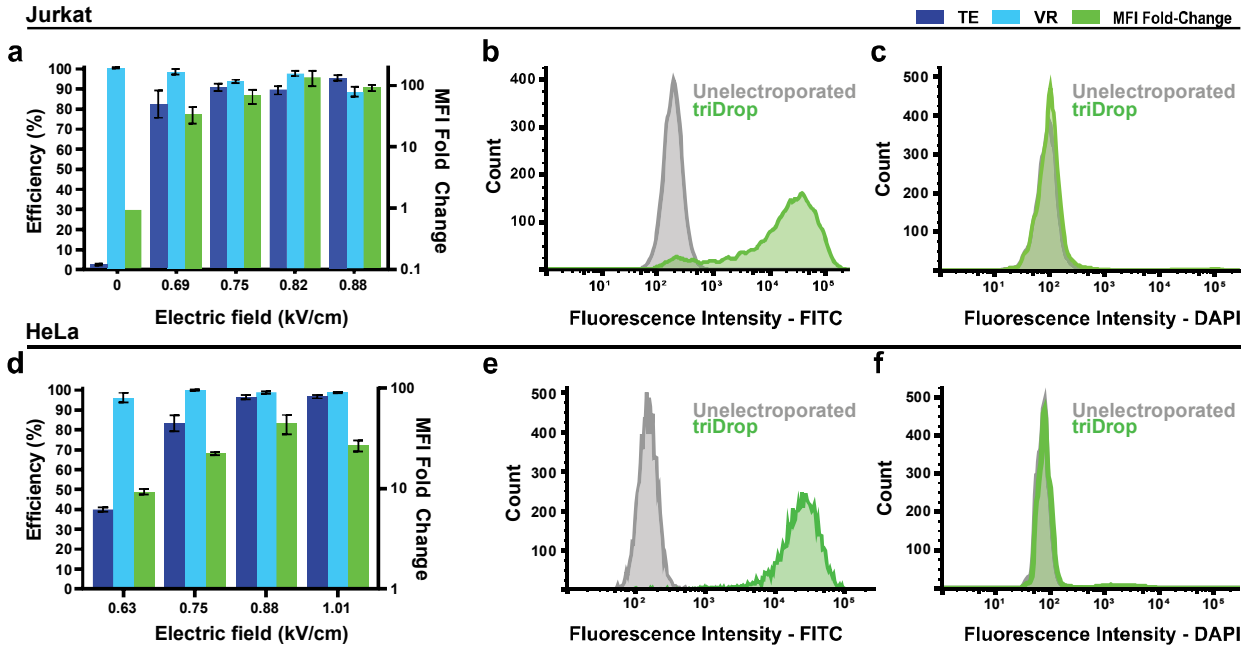

Figure 3-8) reveal a slightly higher effective electric fields range (0.75-0.90 kV/cm) for optimal results. These applied fields place us within the expected range reported by other high performance electroporation devices[118,141]. A list of all electroporation conditions and the corresponding parameters can be found in **Table 2-4**.

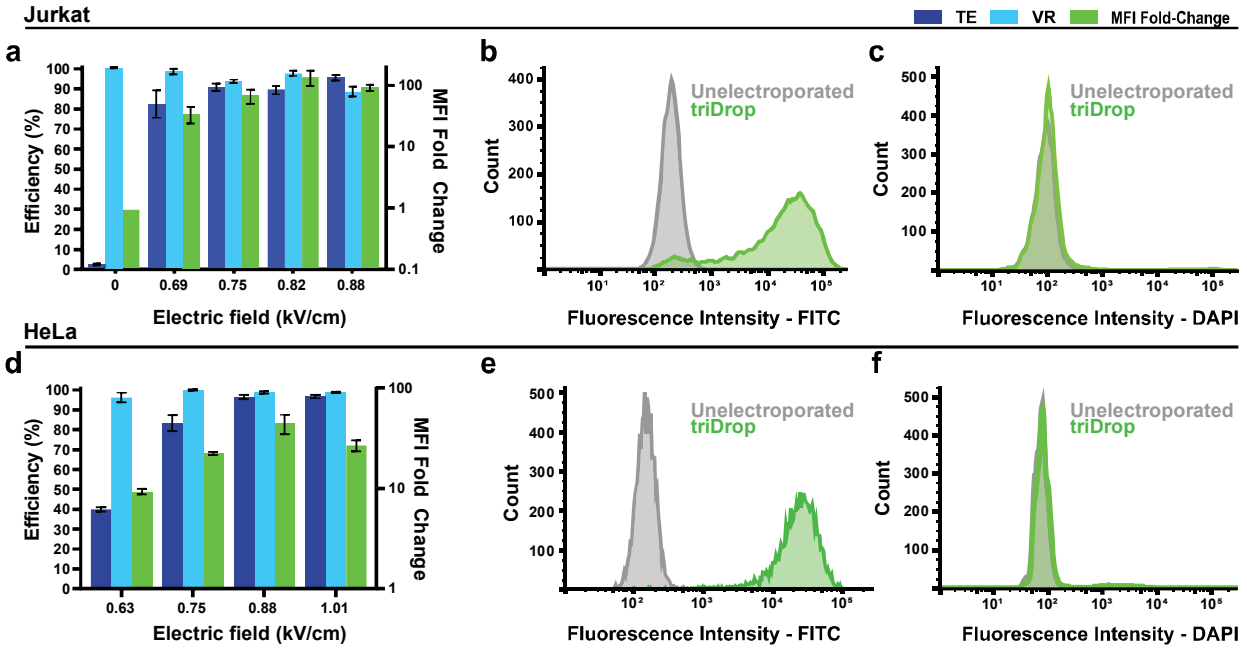

Figure 3-8. TriDrop electroporation parameter optimization for Jurkat and HeLa cells. (a) Voltage optimization using 3, 5 ms pulses on Jurkat cells. (b) FITC fluorescence and (c) DAPI staining comparing an electroporated population (green, 350 V_{DC}) vs an unelectroporated population (grey). (d) Voltage optimization using 3, 10 ms pulses on HeLa cells. (e) FITC fluorescence and (f) DAPI staining comparing an electroporated population (green, 350 V_{DC}) vs an unelectroporated population (grey). All plots with error bars are based on standard error of the mean for n = 3 replicates.

To evaluate the triDrop method relative to gold standard practices (Neon™ transfection system), a series of transfections were performed using HeLa cells and dextran as the payload. All pulse parameters for triDrop are identical to those described above and the Neon™ was operated using the manufacturer recommended settings. The key differences between the systems are that the cell numbers used for the triDrop was lower than the Neon™ (~20,000 vs. ~50,000 cells) and sample volumes for transfection were reduced from 10 mL for the Neon™ to 1 mL for triDrop. As shown in **Figure 3-4f**, cells transfected with the triDrop show very similar high metrics as the Neon™ (TEs > 98 %, VRs > 95 % and MFI fold change > 125). The transfection efficiency was calculated by flow cytometry analysis with the results of the FITC fluorescence counts (for ~15,000 events) to be very similar for both systems (but different than the non-electroporated control cells) (**Figure 3-4g**). These experiments show that our technique

can achieve similar metrics as the standard mammalian-based transfection system with lower cell numbers. As described below, these low cell numbers enabled our work with primary T-cells, which is usually difficult to transfect when cell numbers are below 1 x 10^6 cells since their post-electroporation viability decreases significantly.[28,130,131]

3.3 Immortalized cells

To further evaluate the capacity to transfect mammalian cells, different payloads were delivered to three commonly used immortalized cell types: HEK293, HeLa, and Jurkat T-cells. Each set of cells were prepared and loaded into the DMF platform (as in **Figure 3-1b**) and were transfected with four different payloads: 70 kDa, 250 kDa, and 2000 kDa FITC-tagged dextran, and a 5 kb eGFP plasmid. **Figure 3-9a** and **Figure 3-9b** shows the quantitative metrics for the typical model transfection cell line HEK293 and HeLa cells for the three different dextran sizes (along with a non-electroporated control) respectively. As shown, the metrics are excellent, with a TE > 90 %, VR > 90 %, and > 80 MFI fold-change. In fact, the triDrop system was able to insert the large 2000 kDa FITC-tagged dextran molecule (hydrodynamic diameter ~ 55nm[156]) into both HEK293 and HeLa cell lines with a TE and VR of > 90 %. These results show that the delivery of large molecules into the cytosol of HEK293 and HeLa cells using triDrop is efficient and suggests that the system will be capable of delivering fully formed proteins of similar size or other large molecules[2,149].

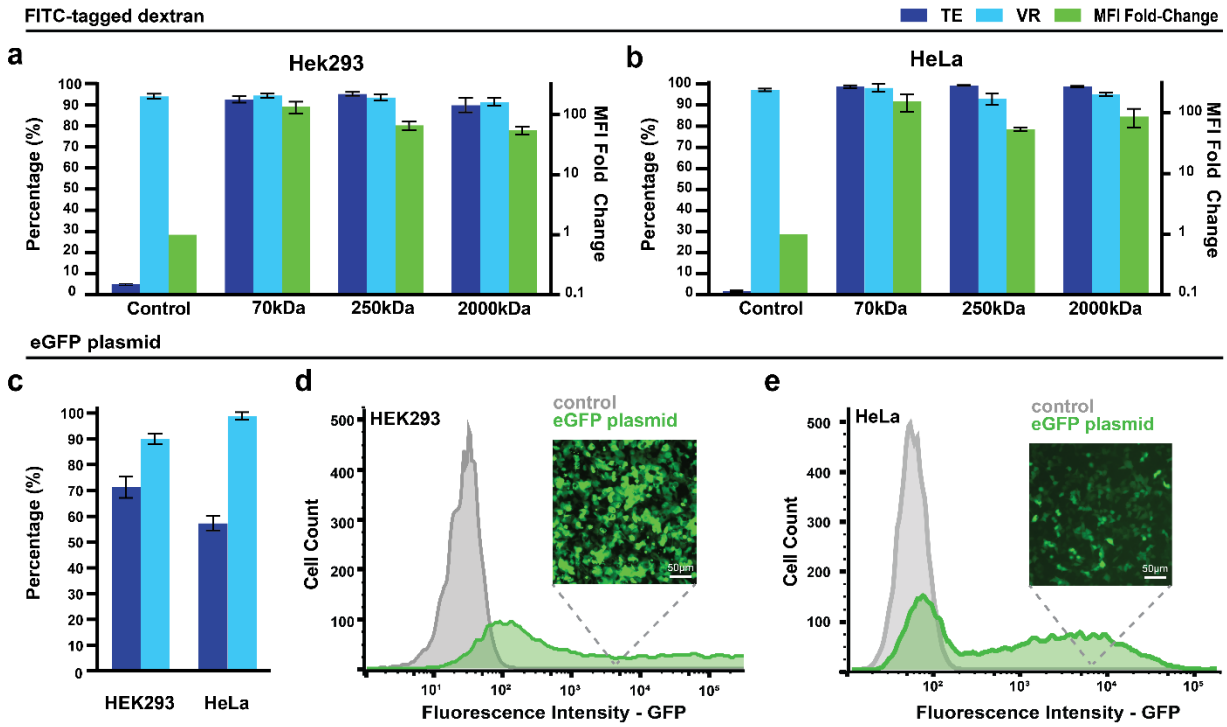

Figure 3-9. Intracellular delivery of diverse payloads in HEK293 and HeLa cells using triDrop. Plots of transfection efficiency, viability ratio, and MFI fold-change comparing an un-electroporated control vs the triDrop system for the insertion of a 70 kDa, 250 kDa, and 2000 kDa FITC-tagged dextran molecules for (a) HEK293 cells and (b) HeLa cells. (c) Plots of transfection efficiency and viability ratio for HEK293 and HeLa when inserting an eGFP plasmid. Fluorescence intensity histograms showing GFP expression for (d) HEK293 cells and (e) HeLa cells vs an unelectroporated control. Inset shows fluorescence images of (d) HEK293 cells and (e) HeLa cells expressing the eGFP plasmid. All plots with error bars are based on standard error of the mean for n = 3 replicates.

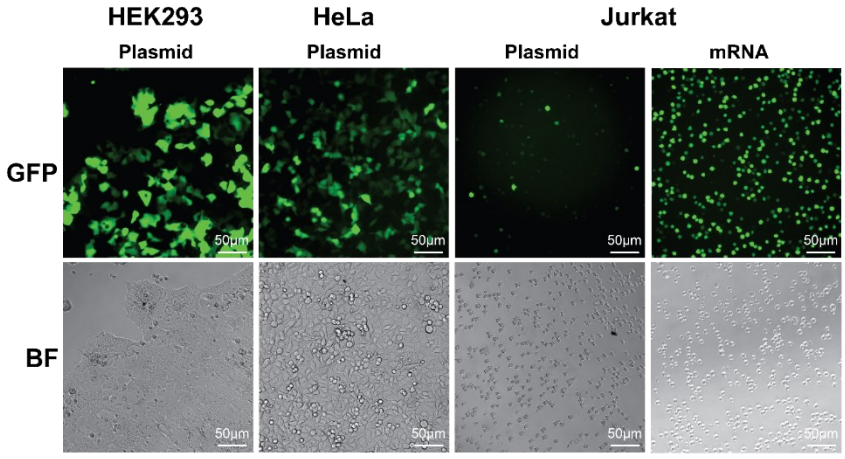

Figure 3-10. Brightfield and GFP images for electroporated HEK293, HeLa, and Jurkat cells.

Moving towards a more biologically relevant payload, we performed the same protocol for delivering plasmids. **Figure 3-9c** shows the TE and VR for HEK293 and HeLa cells, as shown,

we obtained a TE and VR of 71 % and 90 % for HEK293, respectively, and 60 % and 99 %, respectively, for HeLa with both cell types showing healthy morphology after transfection (**Figure 3-10**). These results were obtained via flow cytometry and approximately 15,000 cell events were collected for each sample. The frequency fluorescence histogram is depicted in **Figure 3-9d** (HEK293) and **Figure 3-9e** (HeLa). In both cases, the control population showed very minimal fluorescence (see grey histogram) while the eGFP positive cells (showing successful triDrop electroporation) were shifted towards higher fluorescence than the control (see green plots). These data confirm the triDrop system can be used to insert both large payloads as well as biological payloads which have been challenging to deliver for other microfluidic based mammalian transfection devices[157].

Next, we tested our system with Jurkat T-cells since they have been shown to be a suitable model in immunotherapy research[129] and have a reputation of being a hard-to-transfect cell line[158]. Here, we followed the same protocol as above: electroporating three different dextran molecules (70 kDa, 250 kDa, and 2000 kDa), and eGFP plasmid with the electroporation parameters listed in **Table 2-4**. Additionally, we included an mRNA payload given the increasing interest to use mRNA as an immunotherapeutic molecule[159]. **Figure 3-11a** shows the dextran results for our three metrics and are quantitatively similar to HEK293 and HeLa – both VR and TE > 90 %. The flow cytometry histogram (**Figure 3-11b**) shows a full spectral shift towards higher fluorescence intensities for all three dextran sizes confirming that we can efficiently insert large molecules into Jurkat cells with minimal effect on viability. Furthermore, we transfected a 1 kb eGFP mRNA, and a 5 kb eGFP plasmid. **Figure 3-11**c shows the results 24 hours post-transfection with the mRNA displaying an impressive TE of 95 % (measured via frequency histogram shown in **Figure 3-11**d), a VR of 98 % and an MFI fold-change of > 500

while using only 2 pg of mRNA per cell. Electroporation with both payloads did not negatively influence the morphology of the cells (**Figure 3-10**), however, the plasmid (measured 48-hours post-transfection) showed a modest TE of 40 % (measured via frequency histogram shown in **Figure 3-11**e), and a VR of 96 % and a very modest MFI fold-change of ~12. Increasing plasmid concentration could potentially improve TE in Jurkat cells, however, we wanted to avoid the associated cell toxicity and cell death from high cytosolic DNA concentrations[28]. Taken together, these data suggest that the triDrop technique is suitable for both types of payloads for Jurkat cell transfection, with mRNA having higher TE, similar to previous microfluidic transfection studies[115].

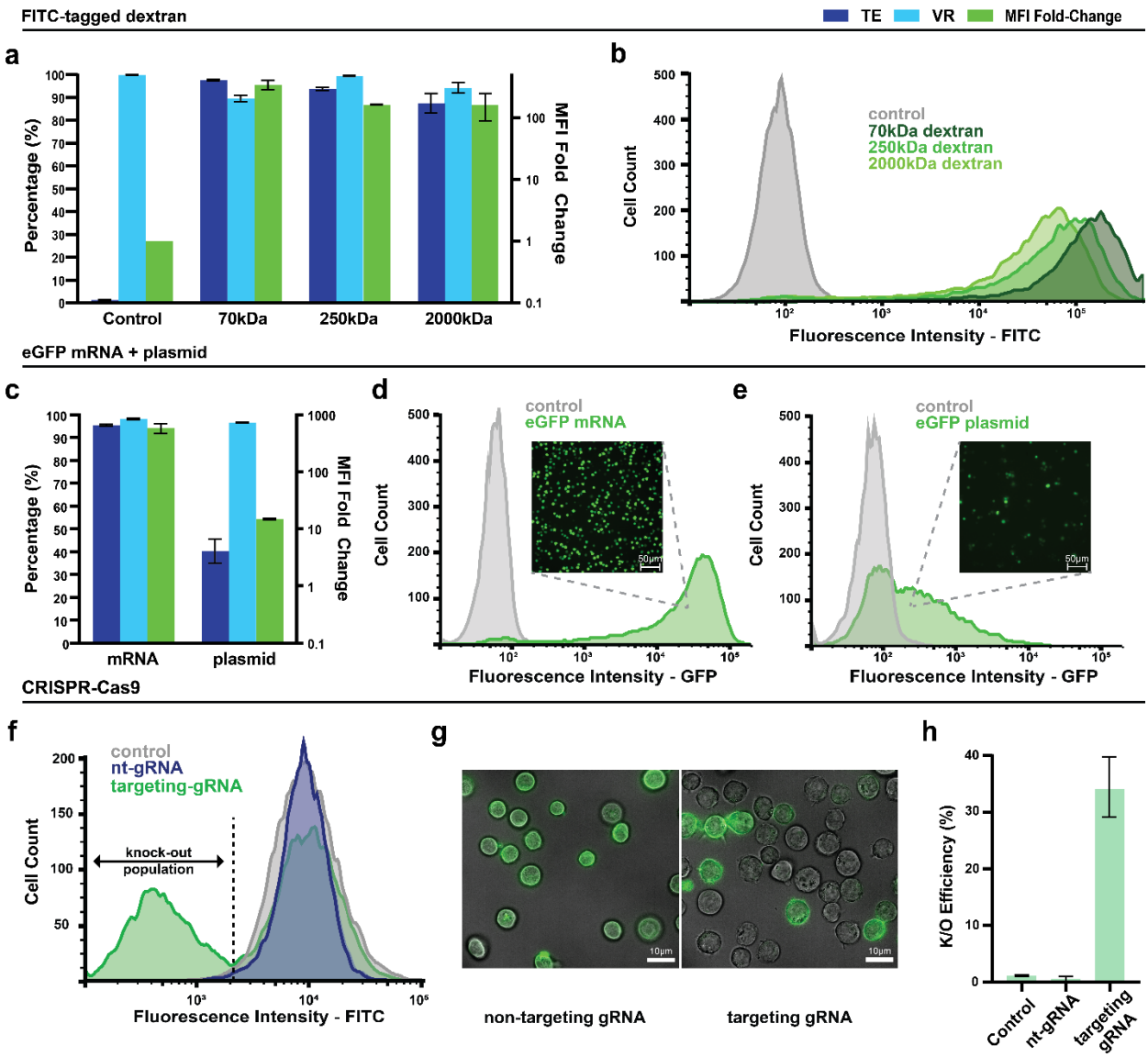

Figure 3-11. Intracellular delivery of diverse payloads into Jurkat cells using triDrop electroporation. (a) Plots of transfection efficiency, viability ratio, and MFI fold-change comparing an un-electroporated control vs the triDrop system for the insertion of a 70kDa, 250kDa, and 2000kDa FITC-tagged dextran molecules. (b) Fluorescence intensity histograms showing the FITC expression comparing the control with the three different dextran molecules inserted using the triDrop system. (c) Plots of transfection efficiency, viability ratio, and MFI fold-change for the insertion of eGFP-mRNA, and eGFP-plasmid using the triDrop system. Fluorescence intensity histograms showing GFP expression for (d) eGFP-mRNA and (e) eGFP-plasmid inserted using triDrop electroporation vs. an unelectroporated control. Inset show fluorescence images for cells expressing (d) eGFP-mRNA and (e) eGFP-plasmid. (f) Fluorescence intensity histograms showing the FITC expression comparing a control vs. non-targeting gRNA vs β2M targeting gRNA populations after staining with a FITC-tagged anti-β2M antibody. (g) Fluorescence images overlaid with bright field images showing (left) cells electroporated with a non-targeting (nt) gRNA and (right) cells electroporated with a gRNA targeting the β2M gene and stained with a FITC-tagged anti-β2M antibody. (h) Plots of β-2-microglobulin knockout efficiency comparing an

unelectroporated control vs. cells electroporated with a Cas9 protein conjugated with a non-targeting gRNA vs. cells electroporated with a Cas9 protein conjugated with a gRNA targeting the β-2-microglobulin gene. All plots with error bars are based on standard error of the mean for n = 3 replicates.

As a final proof-of-principle in Jurkat cells, the triDrop system was used for an on-chip CRISPR knock-out of the β-2-microglobulin (β2M) gene. The β2M gene codes for a protein that serves as a key structural element in all major histocompatibility (MHC) class 1 molecules[160] and when the gene is impaired it can no longer form and be expressed on the cell surface making this an ideal target for an easily detectable proof-of-concept knockout. Jurkat cells were mixed with a Cas9 RNP containing either a scrambled non-targeting gRNA or a gRNA targeting the β2M gene and loaded on to the chip for triDrop electroporation, immediately post electroporation cells were moved off-chip and into recovery buffer and left to incubate for 72 hours. After recovery, cells were blocked for non-specific binding and then stained with a FITC-tagged antibody targeting MHC class 1 molecules (outlined in **section 2.10**). **Figure 3-11f** depicts histogram data for the three different conditions – control (no triDrop electroporation, grey line), non-targeting gRNA (triDrop electroporation with a scrambled gRNA, blue line), and β2M targeting gRNA (triDrop electroporation with a β2M specific gRNA, green line). All three populations had high viabilities (~95%), however, only cells that were electroporated with the β2M specific gRNA show a knockout population, represented by cells with a lower fluorescence intensity (i.e., a peak is shown on the left of the dotted line). As illustrated in representative images after staining, cells remain healthy after 72 hours (~ 95% viability) and only those with knocked out β2M shows cells with no fluorescence (**Figure 3-11g)**. The knockout efficiency is summarized in **Figure 3-11h** and show an average knockout efficiency of 35 % for the cells electroporated with the β2M targeting gRNA whereas the two control populations both have < 2 % knockout. In sum, the gene-editing application here shows that the triDrop platform can deliver complex

payloads into difficult-to-transfect mammalian cells and potentially serve as a future platform for arrayed multiplexed gene editing.

3.4 Primary T cells

With the rise of immunotherapy showing promise for cancer patients, much research has been put into transfecting primary T cells[30]. While Jurkat cells can provide promising initial indicators for immunotherapies, final tests must be done in primary human immune cells[129]. Currently, there is no technology that is capable of generating libraries of engineered primary T cells in an automated and arrayed fashion without requiring millions of cells. To demonstrate the high-impact applicability of the triDrop system, we complete this work by demonstrating the transfection process for primary human CD4+ T cells.

We first applied the triDrop electroporation protocol for the insertion of the 2000 kDa dextran payload. Given the sensitive nature of these cells, we explored reducing the pulse duration as this parameter is known to have a significant effect on cell viability[155]. For each condition three, 450 V pulses were applied with a duration of 1 ms, 3 ms, or 10 ms, shown in **Figure 3-12**. As illustrated in **Figure 3-13a**, reducing the pulse duration (1 and 3 ms) was found to have the optimal metrics with 3 ms producing the best VR > 90 %, TE > 70 %, and an 80 MFI-fold change. The fluorescent signals from the electroporated cells with dextran shows a clear right-shift with a mean fluorescence (FITC) peak around 15, which is 80 times higher than the control (**Figure 3-13b**) and clear gated flow cytometry plots (**Figure 3-12a**) for the 1 ms and 3 ms cases respectively.

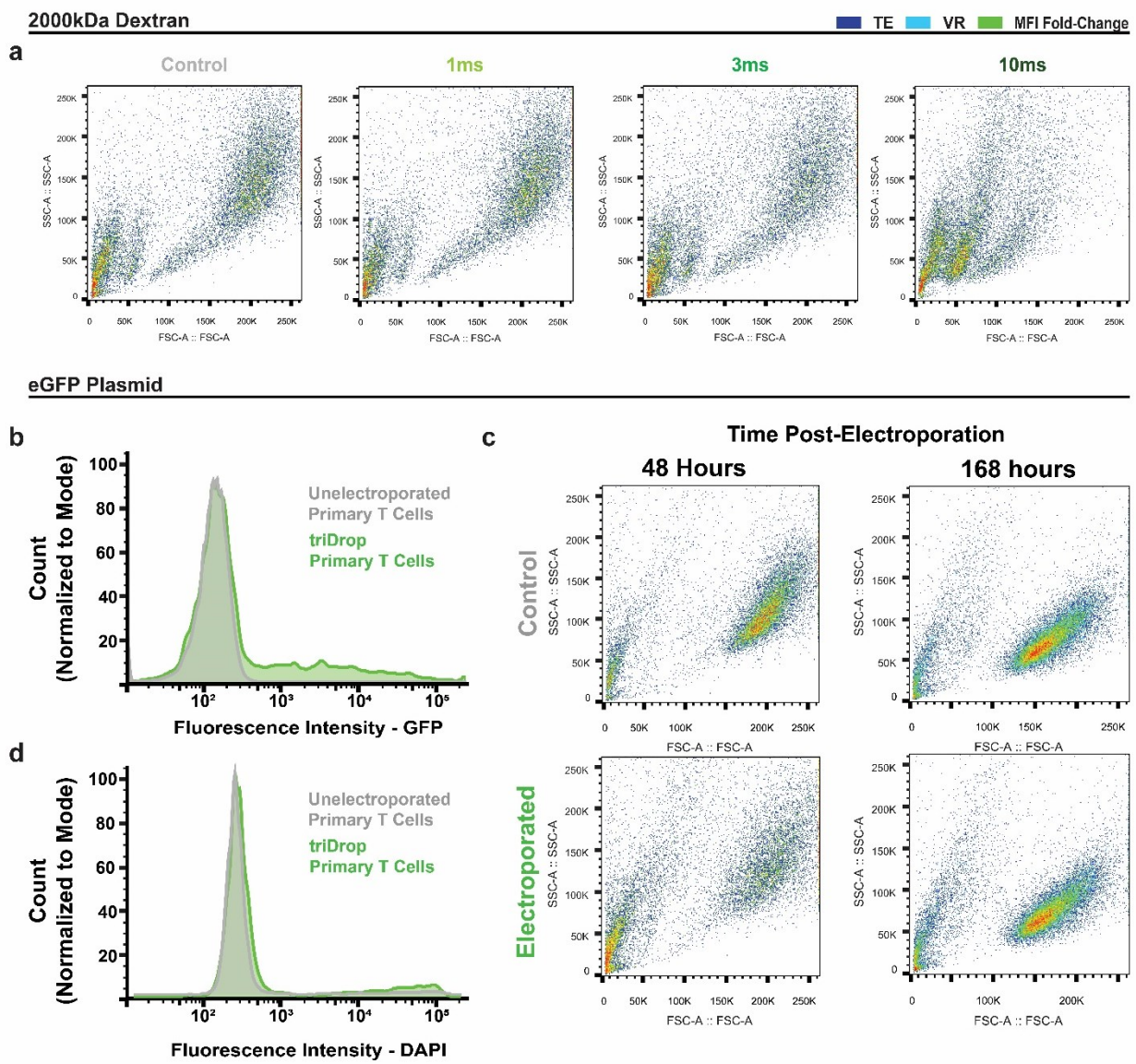

Figure 3-12. Primary T optimization and additional information.
(a) Side scatter vs. forward scatter plots for a control population and populations electroporated with 3 pulses with a duration of 1 ms, 3 ms, and 10 ms. (b) GFP expression histogram and (c) DAPI staining histogram for primary T cells electroporated with an eGFP plasmid (green) vs a control (grey) 48-hours post electroporation. (d) Side scatter vs. forward scatter for a control population and an electroporated population and control population 48 hours and 168 hours post-electroporation.

However, the absence of a shifted peak using a pulse width of 10 ms suggests that very few cells have been transfected. The most likely cause for this significant reduction is that more cells are experiencing detrimental electroporation-induced effects[54–58] on the cell structure from the longer pulse, which may prevent permanent uptake of the dextran molecules. In fact, the

histogram for the 10 ms condition for DAPI staining shows a clear peak at the higher fluorescence levels compared to the control (**Figure 3-13c**) and with the forward/side scatter plots showing very little discrimination between healthy and non-healthy cells (**Figure 3-12a**) suggesting that cell death is playing a role in lower TE and MFI values.

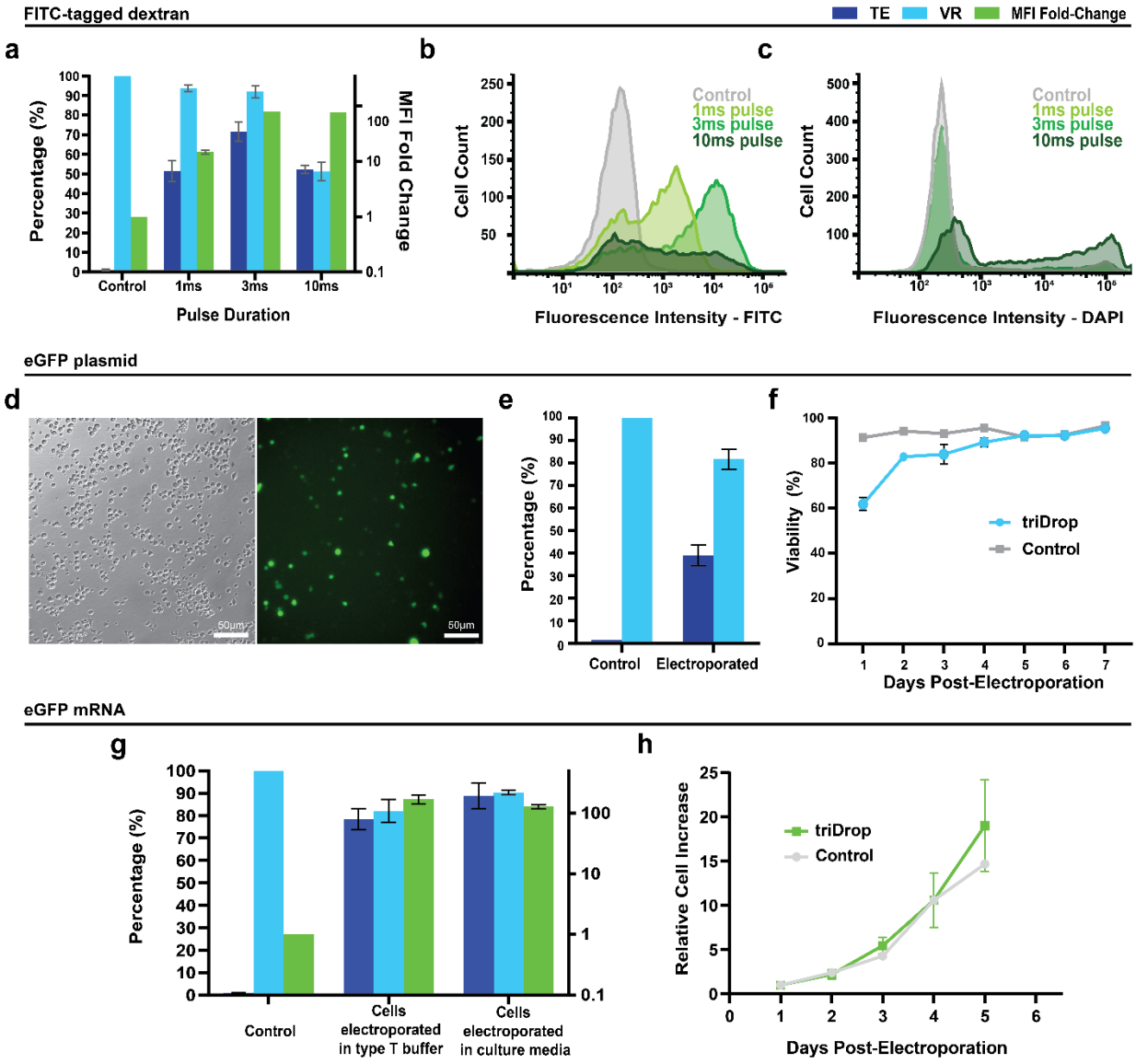

Figure 3-13. Intracellular delivery of large payloads into human primary CD4+ T cells using triDrop. (a) Plots of transfection efficiency, viability ratio, and MFI fold-change comparing an unelectroporated control vs the triDrop system for the insertion of a 2000 kDa FITC-tagged dextran molecule. Fluorescence intensity histograms showing (b) FITC expression and (c) DAPI staining comparing an un-electroporated control vs the triDrop system for the insertion of the dextran molecule. (d) bright-field (left) and fluorescence (right) images showing GFP expression 48-hours post electroporation with the

triDrop system. (e) Plots of transfection efficiency and viability ratio comparing an un-electroporated control vs the triDrop system for the insertion of a 5kb eGFP plasmid 48-hours post transfection. (f) Viability measurements for 7-days of post electroporation culture comparing an unelectroporated control vs. the triDrop system. (g) Plots of transfection efficiency, viability ratio, and MFI fold-change comparing samples electroporated with different electroporation buffers. (h) The cell increase of samples relative to day 1 for 7-days of post electroporation for samples electroporated vs. unelectroporated control. All plots with error bars are based on standard error of the mean for n = 3 replicates.

The primary T cells transfected with the triDrop was further assessed with a plasmid payload. The representative images of the cells after 48 h post-transfection with an eGFP plasmid shows healthy morphology and cells are producing eGFP (**Figure 3-13d**). The electroporated cells were compared to cells that were not electroporated via flow cytometry histograms (**Figure 3-12b and c**). We quantified the VR as well as the TE, and as shown in **Figure 3-13e**, the triDrop electroporated cells shows a VR of 81 % and a TE > 38 %. These are excellent metrics for primary cells outperforming other optimized protocols using commercially available systems[130]. The viability of electroporated cells were monitored daily for the remainder of the week and compared against a non-electroporated control. It was observed that the health of the electroporated cells is comparable to that of non-electroporated cells by day 5 (**Figure 3-13f**) and, 7 days post electroporation, both the control population and the electroporated population had viabilities > 95% (as shown by the forward and side scatter plots – **Figure 3-12d**).

As a final step of optimization using the triDrop system for primary T cells, we show the delivery of eGFP mRNA using cell culture media as our electroporation buffer. The deleterious effects of long term exposure to electroporation buffer on mammalian cells are well-documented[124] and many buffer manufacturers recommend minimizing the time cells spend in the buffer. Additionally, proprietary electroporation buffers can be prohibitively expensive[140,161]. A unique feature of our triDrop system is the ability to generate the electric field focusing effect

on a wide variety of different media if the flanking droplets are comprised of a higher conductivity solution. We created a very high conductive solution ($\sigma \sim 32$ mS/cm, recipe in **Table 2-1** and **Table 2-3)** to use as a flanking buffer for primary T cells suspended in RPMI ($\sigma \sim$ 15 ms/cm) to maintain the high-low-high buffer conductivity triDrop structure (**Figure 3-5**). **Figure 3-13g** shows a comparison between cells electroporated in low conductivity buffer with the original triDrop configuration compared to cells electroporated in culture media using the very high conductive flanks. Both conditions show impressive results, however, as predicted, the cells electroporated in the culture media had superior VR (90 % vs 82 %) and had higher TE (89 % vs 78 %). The electroporated cells were allowed to grow out for 5-days post electroporation and were found to proliferate at a rate comparable to that of unelectroporated cells. After 5 days of culture electroporated cells and control cells show a similar fold increase with a ~19 and ~15-fold population increase respectively (**Figure 3-13h)**. Compared to other works the triDrop system performs exceptionally, **Figure 3-14** shows a side-by-side comparison of the triDrop system against four recent high-performance microfluidic transfection systems for the insertion of mRNA into primary human T cells, demonstrating that triDrop can achieve the best percentage of cells that are both living and transfected while using the least amount of mRNA per cell.

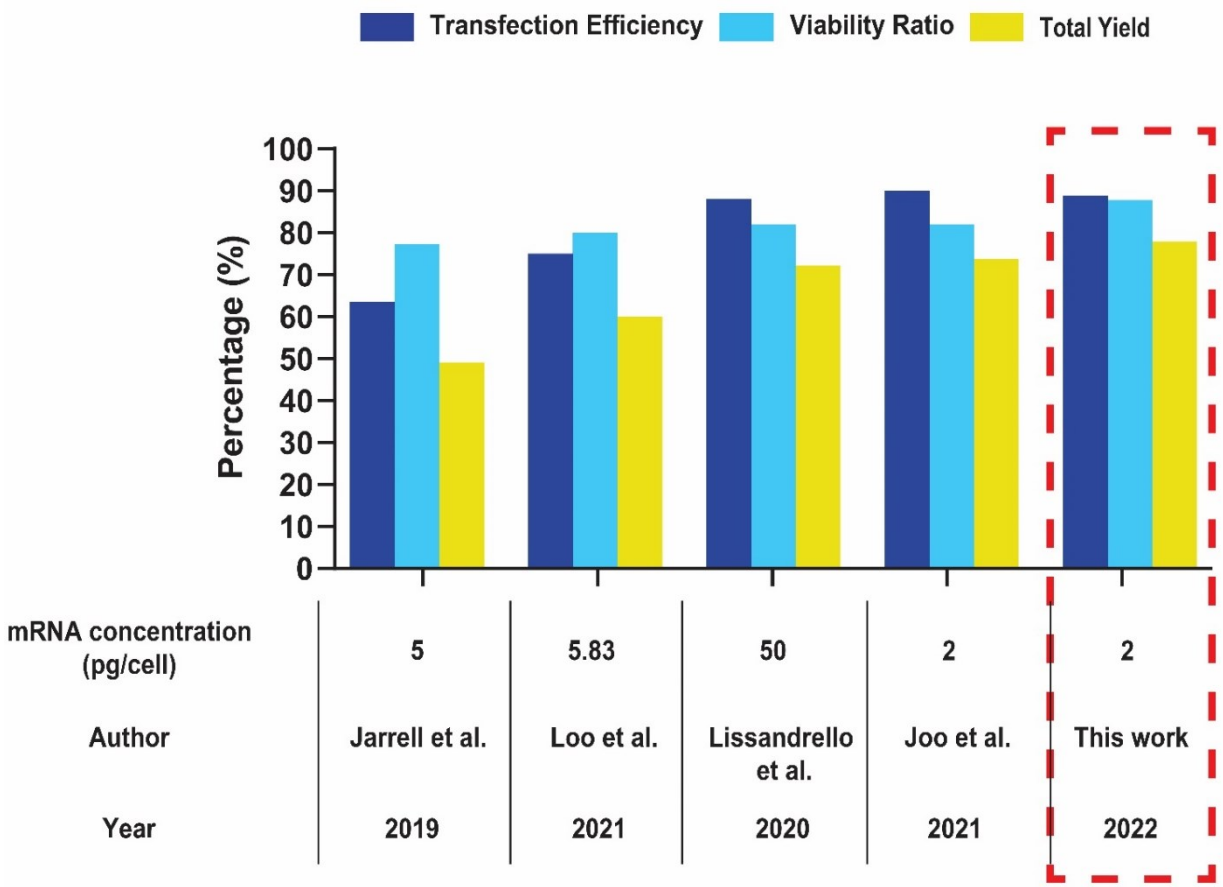

Figure 3-14. Comparison with other recent work[115–118] – Primary T cell mRNA transfection

Chapter 4 Concluding Remarks

In this section, we summarize the features of the triDrop system and describe the advantages of the system in automating genetic engineering, especially in cellular immunotherapy. In addition, we assess the future work related to an electroporation module on DMF.

4.1 Conclusion

TriDrop is an efficient and effective technique for electroporating mammalian cells on a DMF platform with its electroporation parameters (voltage, pulse duration, number of pulses) easily programmable through our automation system and the capability to electroporate very minimal number of cells. In this project, we have shown successful deliveries of a range of dextran molecules, Cas9 RNP, mRNA, and plasmid with high viabilities and transfection efficiencies (>90 %) for HEK293, HeLa, Jurkat, and primary T cells. Additionally, we show that we can perform these electroporation reactions with lower cell numbers that are difficult with current commercially available techniques which typically requires at least 200,000 cells with optimized concentrations at 1-2 million cells per condition.

These results, to our knowledge, are the first of their kind and serve as examples of what is possible for the future. In the future, integrating the triDrop system with high throughput DMF capabilities will allow for large libraries of novel constructs to be tested on rare cells derived from a single patient. This could potentially serve as a platform for ex vivo applications for the research of personalized medicine and cellular immunotherapy. This capability will both accelerate the pace of immune cell engineering, requiring less time to grow and culture cells during research and development stages, while also making it more affordable due to less reagent consumption. We believe the triDrop system will help lift barriers in immune cell engineering

and open the door to discovering new therapeutic breakthroughs via high throughput arrayed screening in an automated manner.

4.2 Future outlook

Since its discovery, microfluidics has proven to be a useful tool in several biomedical applications, and I hope the triDrop electroporation digital microfluidic device can contribute to that growing arsenal of microfluidic tools for biologists and researchers. To achieve that, more optimization needs to be done, specifically on the electroporation parameters, to obtain better transfection efficiencies and potentially reduce the negative electroporation-induced side effects, such as irreversible cell death or increased cell stress[56]. For example, parameters contributing to the electroporation pulse delivered to the cells have been reported to play key roles in different electroporation systems with some studies reporting using a high voltage pulse followed by several low voltage pulses or an exponential decay being benefitial[137,162]. This effort is motivated based on the idea that subsequence low voltage or exponential decay, after an initial high voltage pulse, is used to assist and drive more delivery cargo into the cell[163]. Potentially, this would help reduce the electroporation-induced effects while maintaining high transfection efficiency, or at the very least, increase transfection efficiency without compromising cell viability. Other than pulse type and pulse combinations, other electroporation pulse parameters that we can manipulate and optimize include voltage, pulse duration, and number of pulses delivered. Additionally, to better understand these parameters and their impact on transfection efficiency and viability, additional quantitative methods such as RNAseq can be used to evaluate the effects of different pulse parameters on cellular function on a transcriptomic level[56]. Understanding and minimizing electroporation-induced effects on cellular functions would be

very helpful, especially, in cellular immunotherapy where cellular functions of engineered cells should be similar to that of healthy cells[164].

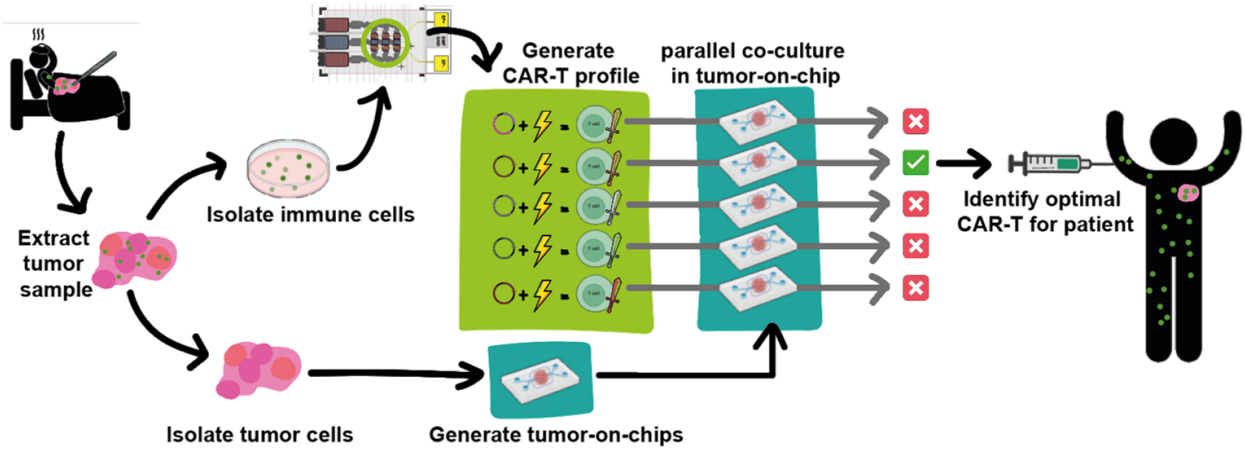

Figure 4-1. TriDrop CAR-T generation for CAR profiling and screening
Potential pipeline for cellular immunotherapy profiling and screening using the microfluidic platform comprising of the triDrop system and organ-on-chips.

Besides that, generation of CAR-T cells using unactivated primary T cells has been a recent clinical interest owing to its improved proliferation, longer persistence, and tumor killing ability with lower doses of CAR-T cells compared to conventional CAR-T cells[165,166]. It is hypothesized that T cells undergo considerable differentiation once activated, limiting its naivety or "stemness" which has been reported to be crucial in engraftment and persistence of T cells following adoptive transfer[167]. More importantly, this removes the need for cell expansion as activation is not required, significantly reducing the time, cost and operation complexitiy involved in CAR-T generation[166]. Genetic engineering of unactivated T cells, however, is challenging owing to the low transfection efficiencies and relatively long doubling time of approx. 3-4 days[168], making cell expansion prone to contamination and time consuming to acquire the high amounts of cells required for its protocol[169]. Only a select few has shown successful generation of CAR-T cells using unactivated T cells, however, optimized protocols is yet to be realised for efficient generation of engineered cells to be able to cycle through large

libraries[165,167,170]. For example, if we were to cycle through a large library of edits, such as Bloemberg *et al*., current methods would require large amounts of unactivated T cells, which can be demanding for patients[129]. To overcome this, researchers need a way to cycle through a large library of genetic edits and clones, and we believe the triDrop system is a promising solution. Preliminary results (data not shown) has shown promising data that reflects successful delivery of mRNA into unactivated primary T cells electroporated with the triDrop system. The triDrop system can be further optimized for highly efficient and effective delivery of biological cargo into unactivated primary T cells for genetic engineering and research in cellular immunotherapy.

Another potential application could include developing a pipeline for screening of CAR construct profiles using tumor-on-chip models developed from patients own immune and cancer cells. It has been seen that patient to patient variability in intracellular delivery and gene expression exists[171]. Hence, potency of a unique CAR construct in one patient may not be as effective in another patient even with the same cancer type. A potential way to understand why this happens and to be able to identify the optimal CAR construct for each individual patient would be to generate a library of CAR-Ts using a single patient sample in an arrayed format and screen them using organ-on-chips[172] (which could also be developed using patients primary cancer cells). In doing so, the potency and efficacy of each CAR construct can be evaluated based on how effective it is using multiple organ-on-chips in parallel. Current technologies would require large cell inputs, however, cancer patients would already have limited number of these immune cells due to an already compromised immune system. TriDrop would be able to reduce the number of cells required to develop a library of CAR-T to be tested one by one without the demand for large numbers of cell input from patients. This would effectively make a pipeline for generating a CAR library and screening for the best CAR construct based on its

efficacy and potency against its target cells. This would be achieved using the primary immune and cancer cells of patients in hopes of improving patient outcomes and recovery. This approach would enable obtaining a patient profile showing which CAR construct is optimal against their cancer type, making the treatment more personalized and potentially more effective.

References

1. Cohen, S. N., Chang, A. C. Y., Boyer, H. W. & Helling, R. B. Construction of biologically functional bacterial plasmids in vitro. *Proceedings of the National Academy of Sciences of the United States of America* **70**, 3240–3244 (1973).

2. Stewart, M. P., Langer, R. & Jensen, K. F. Intracellular delivery by membrane disruption: Mechanisms, strategies, and concepts. *Chemical Reviews* **118**, 7409–7531 (2018).

3. Shi, Y., Inoue, H., Wu, J. C. & Yamanaka, S. Induced pluripotent stem cell technology: A decade of progress. *Nature Reviews Drug Discovery* **16**, 115–130 (2017).

4. Robinton, D. A. & Daley, G. Q. The promise of induced pluripotent stem cells in research and therapy. *Nature* **481**, 295–305 (2012).

5. Sterner, R. C. & Sterner, R. M. CAR-T cell therapy: current limitations and potential strategies. *Blood Cancer Journal* **11**, (2021).

6. Newick, K., O'Brien, S., Moon, E. & Albelda, S. M. CAR T Cell Therapy for Solid Tumors. *Annual Review of Medicine* **68**, 139–152 (2017).

7. Rafiq, S., Hackett, C. S. & Brentjens, R. J. Engineering strategies to overcome the current roadblocks in CAR T cell therapy. *Nature Reviews Clinical Oncology* **17**, 147–167 (2020).

8. Kankeu Fonkoua, L. A., Sirpilla, O., Sakemura, R., Siegler, E. L. & Kenderian, S. S. CAR T cell therapy and the tumor microenvironment: Current challenges and opportunities. *Molecular Therapy - Oncolytics* **25**, 69–77 (2022).

9. Porter, D. L. *et al.* Chimeric antigen receptor T cells persist and induce sustained remissions in relapsed refractory chronic lymphocytic leukemia. *Science Translational Medicine* **7**, (2015).

10. Bouchkouj, N. *et al.* FDA approval summary: Axicabtagene Ciloleucel for Relapsed or Refractory Large B-cell Lymphoma. *Clinical Cancer Research* **25**, 1702–1708 (2019).

11. Locke, F. L. *et al.* Phase 1 Results of ZUMA-1: A Multicenter Study of KTE-C19 Anti-CD19 CAR T Cell Therapy in Refractory Aggressive Lymphoma. *Molecular Therapy* **25**, 285–295 (2017).

12. Neelapu, S. S. *et al.* Axicabtagene Ciloleucel CAR T-Cell Therapy in Refractory Large B-Cell Lymphoma. *New England Journal of Medicine* **377**, 2531–2544 (2017).

13. Munshi, N. C. *et al.* Idecabtagene Vicleucel in Relapsed and Refractory Multiple Myeloma. *New England Journal of Medicine* **384**, 705–716 (2021).

14. Anagnostou, T., Riaz, I. B., Hashmi, S. K., Murad, M. H. & Kenderian, S. S. Anti-CD19 chimeric antigen receptor T-cell therapy in acute lymphocytic leukaemia: a systematic review and meta-analysis. *The Lancet Haematology* **7**, e816–e826 (2020).

15. Bhardwaj, A. & Nain, V. TALENs—an indispensable tool in the era of CRISPR: a mini review. *Journal of Genetic Engineering and Biotechnology* **19**, 1–10 (2021).

16. Gaj, T., Gersbach, C. A. & Barbas, C. F. ZFN, TALEN, and CRISPR/Cas-based methods for genome engineering. *Trends in Biotechnology* **31**, 397–405 (2013).

17. Carroll, D. Progress and prospects: Zinc-finger nucleases as gene therapy agents. *Gene Therapy* **15**, 1463–1468 (2008).

18. Katti, A., Diaz, B. J., Caragine, C. M., Sanjana, N. E. & Dow, L. E. CRISPR in cancer biology and therapy. *Nature reviews cancer* **13**, 259–279 (2022).

19. Simeonov, D. R. & Marson, A. CRISPR-Based Tools in Immunity. *Annual Review of Immunology* **37**, 571–597 (2019).

20. Lee, C. S. *et al.* Adenovirus-mediated gene delivery: Potential applications for gene and cell-based therapies in the new era of personalized medicine. *Genes and Diseases* **4**, 43–63 (2017).

21. Brunner, S. *et al.* Cell cycle dependence of gene transfer by lipoplex, polyplex and recombinant adenovirus. *Gene Therapy* **7**, 401–407 (2000).

22. Mesika, A., Grigoreva, I., Zohar, M. & Reich, Z. A regulated, NFκB-assisted import of plasmid DNA into mammalian cell nuclei. *Molecular Therapy* **3**, 653–657 (2001).

23. Mingozzi, F. & High, K. A. Therapeutic in vivo gene transfer for genetic disease using AAV: Progress and challenges. *Nature Reviews Genetics* **12**, 341–355 (2011).

24. Moretti, A. *et al.* The Past, Present, and Future of Non-Viral CAR T Cells. *Frontiers in immunology* **13**, 867013 (2022).

25. Sun, S., Rao, V. B. & Rossmann, M. G. Genome packaging in viruses. *Current Opinion in Structural Biology* **20**, 114–120 (2010).

26. Roth, T. L. *et al.* Pooled Knockin Targeting for Genome Engineering of Cellular Immunotherapies. *Cell* **181**, 728-744.e21 (2020).

27. Sido, J. M. *et al.* Electro-mechanical transfection for non-viral primary immune cell engineering. *bioRxiv* 2021.10.26.465897 (2021).

28. Roth, T. L. *et al.* Reprogramming human T cell function and specificity with non-viral genome targeting. *Nature* **559**, 405–409 (2018).

29. Harris, E., Zimmerman, D., Warga, E., Bamezai, A. & Elmer, J. Nonviral gene delivery to T cells with Lipofectamine LTX. *Biotechnology and Bioengineering* **118**, 1693–1706 (2021).

30. Raes, L., De Smedt, S. C., Raemdonck, K. & Braeckmans, K. Non-viral transfection technologies for next-generation therapeutic T cell engineering. *Biotechnology Advances* **49**, 107760 (2021).

31. Sahay, G., Alakhova, D. Y. & Kabanov, A. V. Endocytosis of nanomedicines. *Journal of Controlled Release* **145**, 182–195 (2010).

32. Gilleron, J. *et al.* Image-based analysis of lipid nanoparticle-mediated siRNA delivery, intracellular trafficking and endosomal escape. *Nature biotechnology* **31**, 638–46 (2013).

33. Wiethoff, C. M. & Middaugh, C. R. Barriers to Nonviral Gene Delivery. *Journal of Pharmaceutical Sciences* **92**, 203–217 (2003).

34. Schaffer, D. V., Fidelman, N. A., Dan, N. & Lauffenburger, D. A. Vector unpacking as a potential barrier for receptor-mediated polyplex gene delivery. *Biotechnology and Bioengineering* **67**, 598–606 (2000).

35. Tsoi, M. *et al.* Characterization of condensed plasmid DNA models for studying the direct effect of ionizing radiation. *Biophysical Chemistry* **147**, 104–110 (2010).

36. Kunath, K. *et al.* Low-molecular-weight polyethylenimine as a non-viral vector for DNA delivery: Comparison of physicochemical properties, transfection efficiency and in vivo distribution with high-molecular-weight polyethylenimine. *Journal of Controlled Release* **89**, 113–125 (2003).

37. Moghimi, S. M. *et al.* A two-stage poly(ethylenimine)-mediated cytotoxicity: Implications for gene transfer/therapy. *Molecular Therapy* **11**, 990–995 (2005).

38. Choi, Y. J., Kang, S. J., Kim, Y. J., Lim, Y. B. & Chung, H. W. Comparative studies on the genotoxicity and cytotoxicity of polymeric gene carriers polyethylenimine (PEI) and polyamidoamine (PAMAM) dendrimer in Jurkat T-cells. *Drug and Chemical Toxicology* **33**, 357–366 (2010).

39. Yu, X. *et al.* Improved delivery of Cas9 protein/gRNA complexes using lipofectamine CRISPRMAX. *Biotechnology Letters* **38**, 919–929 (2016).

40. Koley, D. & Bard, A. J. Triton X-100 concentration effects on membrane permeability of a single HeLa cell by scanning electrochemical microscopy (SECM). *Proceedings of the National Academy of Sciences of the United States of America* **107**, 16783–16787 (2010).

41. Frenkel, N., Makky, A., Sudji, I. R., Wink, M. & Tanaka, M. Mechanistic investigation of interactions between steroidal saponin digitonin and cell membrane models. *Journal of Physical Chemistry B* **118**, 14632–14639 (2014).

42. Chong, Z. X., Yeap, S. K. & Ho, W. Y. Transfection types, methods and strategies: A technical review. *PeerJ* **9**, 1–37 (2021).

43. BioRad. BioRad Electroporation. Available at: https://www.bio-rad.com/en-ca/category/electroporation?ID=c1ae4cd3-ef42-4734-8d6c-7fce69992ccb. (Accessed: 20th December 2022)

44. ThermoFisher Scientific. Neon Electroporation. Available at: https://www.thermofisher.com/ca/en/home/life-science/cell-culture/transfection/neon-transfection-system.html. (Accessed: 20th December 2022)

45. Lonza BioScience. Lonza Electroporation. Available at: https://bioscience.lonza.com/lonza_bs/CA/en/nucleofector-technology. (Accessed: 20th December 2022)

46. Morshedi Rad, D. *et al.* A Comprehensive Review on Intracellular Delivery. *Advanced Materials* **33**, 1–36 (2021).

47. Hur, J. & Chung, A. J. Microfluidic and Nanofluidic Intracellular Delivery. *Advanced Science* **8**, 15094–15106 (2021).

48. Li, Y. *et al.* Electroporation on microchips: The harmful effects of pH changes and scaling down. *Scientific Reports* **5**, 1–11 (2015).

49. Kooijmans, S. A. A. *et al.* Electroporation-induced siRNA precipitation obscures the efficiency of siRNA loading into extracellular vesicles. *Journal of Controlled Release* **172**, 229–238 (2013).

50. Breslow, R. & Huang, D. L. Effects of metal ions, including Mg2+ and lanthanides, on the cleavage of ribonucleotides and RNA model compounds. *Proceedings of the National Academy of Sciences of the United States of America* **88**, 4080–4083 (1991).

51. Derfus, A. M., Chan, W. C. W. & Bhatia, S. N. Intracellular Delivery of Quantum Dots for Live Cell Labeling and Organelle Tracking. *Advanced Materials* **16**, 961–966 (2004).

52. Stapulionis, R. Electric pulse-induced precipitation of biological macromolecules in electroporation. *Bioelectrochemistry and Bioenergetics* **48**, 249–254 (1999).

53. Loomis-Husselbee, J. W., Cullen, P. J., Irvine, R. F. & Dawson, A. P. Electroporation can cause artefacts due to solubilization of cations from the electrode plates: Aluminium ions enhance conversion of inositol 1,3,4, 5-tetrakisphosphate into inositol 1,4,5-triphosphate in electroporated L1210 cells. *Biochemical Journal* **277**, 883–885 (1991).

54. Lenz, P., Bacot, S. M., Frazier-Jessen, M. R. & Feldman, G. M. Nucleoporation of dendritic cells: efficient gene transfer by electroporation into human monocyte-derived dendritic cells. *FEBS letters* **538**, 149–54 (2003).

55. Schmiderer, L. *et al.* Efficient and nontoxic biomolecule delivery to primary human hematopoietic stem cells using nanostraws. *Proceedings of the National Academy of Sciences of the United States of America* **117**, 21267–21273 (2020).

56. DiTommaso, T. *et al.* Cell engineering with microfluidic squeezing preserves functionality of primary immune cells in vivo. *Proceedings of the National Academy of Sciences of the United States of America* **115**, E10907–E10914 (2018).

57. Zhang, M. *et al.* The impact of Nucleofection® on the activation state of primary human CD4 T cells. *Journal of Immunological Methods* **408**, 123–131 (2014).

58. Grys, M., Madeja, Z. & Korohoda, W. Avoiding the side effects of electric current pulse application to electroporated cells in disposable small volume cuvettes assures good cell survival. *Cellular and Molecular Biology Letters* **22**, 1–13 (2017).

59. Piñero, J., López-Baena, M., Ortiz, T. & Cortés, F. Apoptotic and necrotic cell death are both induced by electroporation in HL60 human promyeloid leukaemia cells. *Apoptosis* **2**, 330–336 (1997).

60. Kim, T. K. & Eberwine, J. H. Mammalian cell transfection: The present and the future. *Analytical and Bioanalytical Chemistry* **397**, 3173–3178 (2010).

61. Mali, S. Delivery systems for gene therapy. *Indian Journal of Human Genetics* **19**, 3–8

(2013).

62. Castillo-León, J. Microfluidics and Lab-on-a-Chip Devices: History and Challenges. in *Lab-on-a-Chip Devices and Micro-Total Analysis Systems* (eds. Castillo-León, J. & Svendsen, W. E.) 1–15 (Springer International Publishing, 2015). doi:10.1007/978-3-319-08687-3_1

63. Whitesides, G. M. The origins and the future of microfluidics. *Nature* **442**, 368–373 (2006).

64. Convery, N. & Gadegaard, N. 30 Years of Microfluidics. *Micro and Nano Engineering* **2**, 76–91 (2019).

65. Sun, M. & Duan, X. Recent advances in micro / nanoscale intracellular delivery. *Nanotechnology and Precision Engineering* **18**, 18–31 (2021).

66. Englert, D. L., Manson, M. D. & Jayaraman, A. Flow-based microfluidic device for quantifying bacterial chemotaxis in stable, competing gradients. *Applied and Environmental Microbiology* **75**, 4557–4564 (2009).

67. Pan, J. *et al.* Quantitative tracking of the growth of individual algal cells in microdroplet compartments. *Integrative Biology* **3**, 1043–1051 (2011).

68. Choi, K., Ng, A. H. C., Fobel, R. & Wheeler, A. R. Digital microfluidics. *Annual Review of Analytical Chemistry* **5**, 413–440 (2012).

69. Novotný, J. & Foret, F. Fluid manipulation on the micro-scale: Basics of fluid behavior in microfluidics. *Journal of Separation Science* **40**, 383–394 (2017).

70. Nguyen, N. T., Hejazian, M., Ooi, C. H. & Kashaninejad, N. Recent advances and future perspectives on microfluidic liquid handling. *Micromachines* **8**, 186 (2017).

71. Lee, C. Y., Chang, C. L., Wang, Y. N. & Fu, L. M. Microfluidic mixing: A review. *International Journal of Molecular Sciences* **12**, 3263–3287 (2011).

72. He, B., Burke, B. J., Zhang, X., Zhang, R. & Regnier, F. E. A picoliter-volume mixer for microfluidic analytical systems. *Analytical Chemistry* **73**, 1942–1947 (2001).

73. Mengeaud, V., Josserand, J. & Girault, H. H. Mixing processes in a zigzag microchannel: Finite element simulations and optical study. *Analytical Chemistry* **74**, 4279–4286 (2002).

74. Stroock, A. D. *et al.* Chaotic mixer for microchannels. *Science* **295**, 647–651 (2002).

75. Karthikeyan, K. & Sujatha, L. Study of permissible flow rate and mixing efficiency of the micromixer devices. *International Journal of Chemical Reactor Engineering* **17**, (2019).

76. Zilz, J. *et al.* Serpentine channels: Micro-rheometers for fluid relaxation times. *Lab on a Chip* **14**, 351–358 (2014).

77. Hansen, C. L., Sommer, M. O. A. & Quake, S. R. Systematic investigation of protein phase behavior with a microfluidic formulator. *Proceedings of the National Academy of Sciences of the United States of America* **101**, 14431–14436 (2004).

78. Cooksey, G. A., Sip, C. G. & Folch, A. A multi-purpose microfluidic perfusion system with combinatorial choice of inputs, mixtures, gradient patterns, and flow rates. *Lab on a*

chip **9**, 417–26 (2009).

79. Kong, D. S. *et al.* Open-source, community-driven microfluidics with Metafluidics. *Nature Biotechnology* **35**, 523–529 (2017).

80. Ahmed, D., Mao, X., Juluri, B. K. & Huang, T. J. A fast microfluidic mixer based on acoustically driven sidewall-trapped microbubbles. *Microfluidics and Nanofluidics* **7**, 727–731 (2009).

81. Tsai, J. H. & Lin, L. Active microfluidic mixer and gas bubble filter driven by thermal bubble micropump. *Sensors and Actuators, A: Physical* **97**–**98**, 665–671 (2002).

82. Campisi, M., Accoto, D., Damiani, F. & Dario, P. A soft-lithographed chaotic electrokinetic micromixer for efficient chemical reactions in lab-on-chips. *Journal of Micro-Nano Mechatronics* **5**, 69–76 (2009).

83. Toh, A. G. G., Wang, Z. P., Yang, C. & Nguyen, N. T. Engineering microfluidic concentration gradient generators for biological applications. *Microfluidics and Nanofluidics* **16**, 1–18 (2014).

84. Tan, S. Y. *et al.* Transcriptomic analysis of 3D vasculature-on-a-chip reveals paracrine factors affecting vasculature growth and maturation. *Lab on a Chip* **22**, 3885–3897 (2022).

85. Tenje, M., Fornell, A., Ohlin, M. & Nilsson, J. Particle Manipulation Methods in Droplet Microfluidics. *Analytical chemistry* **90**, 1434–1443 (2018).

86. Sohrabi, S., Kassir, N. & Keshavarz Moraveji, M. Droplet microfluidics: fundamentals and its advanced applications. *RSC Advances* **10**, 27560–27574 (2020).

87. Mazutis, L. *et al.* Single-cell analysis and sorting using droplet-based microfluidics. *Nature Protocols* **8**, 870–891 (2013).

88. Klein, A. M. *et al.* Droplet barcoding for single-cell transcriptomics applied to embryonic stem cells. *Cell* **161**, 1187–1201 (2015).

89. Farrell, J. A. *et al.* Single-cell reconstruction of developmental trajectories during zebrafish embryogenesis. *Science (New York, N.Y.)* **360**, (2018).

90. Zheng, G. X. Y. *et al.* Massively parallel digital transcriptional profiling of single cells. *Nature Communications* **8**, 1–12 (2017).

91. Zhu, Y. & Fang, Q. Analytical detection techniques for droplet microfluidics-A review. *Analytica Chimica Acta* **787**, 24–35 (2013).

92. Tice, J. D., Song, H., Lyon, A. D. & Ismagilov, R. F. Formation of Droplets and Mixing in Multiphase Microfluidics at Low Values of the Reynolds and the Capillary Numbers. *Langmuir* **19**, 9127–9133 (2003).

93. Baret, J. C. *et al.* Fluorescence-activated droplet sorting (FADS): Efficient microfluidic cell sorting based on enzymatic activity. *Lab on a Chip* **9**, 1850–1858 (2009).

94. Sciambi, A. & Abate, A. R. Accurate microfluidic sorting of droplets at 30 kHz. *Lab on a Chip* **15**, 47–51 (2015).

95. Bremond, N., Thiam, A. R. & Bibette, J. Decompressing Emulsion Droplets Favors Coalescence. *Physical Review Letters* **100**, 024501 (2008).

96. Niu, X., Gulati, S., Edel, J. B. & Demello, A. J. Pillar-induced droplet merging in microfluidic circuits. *Lab on a Chip* **8**, 1837–1841 (2008).

97. Li, Z., Li, L., Liao, M., He, L. & Wu, P. Multiple splitting of droplets using multi-furcating microfluidic channels. *Biomicrofluidics* **13**, 024112 (2019).

98. Link, D. R., Anna, S. L., Weitz, D. A. & Stone, H. A. Geometrically Mediated Breakup of Drops in Microfluidic Devices. *Physical Review Letters* **92**, 4 (2004).

99. Ahmadi, F., Samlali, K., Vo, P. Q. N. & Shih, S. C. C. An integrated droplet-digital microfluidic system for on-demand droplet creation, mixing, incubation, and sorting. *Lab on a Chip* **19**, 524–535 (2019).

100. Iwai, K. *et al.* Hybrid droplet/digital microfluidic platform with integrated optical detection system for high-throughput genetic engineering. *20th International Conference on Miniaturized Systems for Chemistry and Life Sciences, MicroTAS 2016* 134–135 (2016).

101. Samiei, E., Tabrizian, M. & Hoorfar, M. A review of digital microfluidics as portable platforms for lab-on a-chip applications. *Lab on a Chip* **16**, 2376–2396 (2016).

102. Li, J. & Kim, C.-J. "CJ". Current commercialization status of electrowetting-on-dielectric (EWOD) digital microfluidics. *Lab on a Chip* **20**, 1705–1712 (2020).

103. Sinha, H., Quach, A. B. V., Vo, P. Q. N. & Shih, S. C. C. An automated microfluidic gene-editing platform for deciphering cancer genes. *Lab on a Chip* **18**, 2300–2312 (2018).

104. Quach, A. B. V., Little, S. R. & Shih, S. C. C. Viral Generation, Packaging, and Transduction on a Digital Microfluidic Platform. *Analytical Chemistry* **94**, 4039–4047 (2022).

105. G, L. Relations entre les phenom ´ enes ` electriques et capillaires. *Ann. Chim. Phys.* **5**, 494 (1875).

106. Berge, B. Electrocapillarity and wetting of insulator films by water. *Comptes Rendus de l'Académie des Sciences* **317**, 157–163 (1993).

107. Quilliet, C. & Berge, B. Electrowetting: a recent outbreak. *Current Opinion in Colloid & Interface Science* **6**, 34–39 (2001).

108. Pollack, M. G., Shenderov, A. D. & Fair, R. B. Electrowetting-based actuation of droplets for integrated microfluidicsElectronic supplementary information (ESI) available: six videos showing droplet flow, droplet dispensing and electrowetting. See http://www.rsc.org/suppdata/lc/b1/b110474h/. *Lab on a Chip* **2**, 96 (2002).

109. Cho, S. K., Moon, H. & Kim, C. J. Creating, transporting, cutting, and merging liquid droplets by electrowetting-based actuation for digital microfluidic circuits. *Journal of Microelectromechanical Systems* **12**, 70–80 (2003).

110. Berthier, J. *et al.* Actuation potentials and capillary forces in electrowetting based microsystems. *Sensors and Actuators, A: Physical* **134**, 471–479 (2007).

111. Chatterjee, D., Hetayothin, B., Wheeler, A. R., King, D. J. & Garrell, R. L. Droplet-based microfluidics with nonaqueous solvents and solutions. *Lab on a Chip* **6**, 199–206 (2006).

112. Chatterjee, D., Shepherd, H. & Garrell, R. L. Electromechanical model for actuating liquids in a two-plate droplet microfluidic device. *Lab on a Chip* **9**, 1219–1229 (2009).

113. Jones, T. B. On the relationship of dielectrophoresis and electrowetting. *Langmuir* **18**, 4437–4443 (2002).

114. Sharei, A. *et al.* Cell Squeezing as a Robust, Microfluidic Intracellular Delivery Platform. *Journal of Visualized Experiments* e50980 (2013). doi:10.3791/50980

115. Joo, B., Hur, J., Kim, G. B., Yun, S. G. & Chung, A. J. Highly Efficient Transfection of Human Primary T Lymphocytes Using Droplet-Enabled Mechanoporation. *ACS Nano* **15**, 12888–12898 (2021).

116. Loo, J. *et al.* Microfluidic transfection of mRNA into human primary lymphocytes and hematopoietic stem and progenitor cells using ultra-fast physical deformations. *Scientific Reports* **11**, 1–11 (2021).

117. Jarrell, J. A. *et al.* Intracellular delivery of mRNA to human primary T cells with microfluidic vortex shedding. *Scientific Reports* **9**, 1–11 (2019).

118. Lissandrello, C. A. *et al.* High-throughput continuous-flow microfluidic electroporation of mRNA into primary human T cells for applications in cellular therapy manufacturing. *Scientific Reports* **10**, 1–16 (2020).

119. Jarrell, J. A. *et al.* Genome editing human primary T cells with microfluidic vortex shedding & CRISPR Cas9. *bioRxiv* **3**, 6 (2021).

120. Jarrell, J. A. *et al.* Numerical optimization of microfluidic vortex shedding for genome editing T cells with Cas9. *Scientific Reports* **11**, 6 (2021).

121. Sharei, A. *et al.* A vector-free microfluidic platform for intracellular delivery. *Proceedings of the National Academy of Sciences of the United States of America* **110**, 2082–2087 (2013).

122. Study of SQZ-PBMC-HPV in Patients With HPV16+ Recurrent, Locally Advanced or Metastatic Solid Tumors - Full Text View - ClinicalTrials.gov. Available at: https://clinicaltrials.gov/ct2/show/NCT04084951. (Accessed: 20th December 2022)

123. Zhu, T. *et al.* Electroporation based on hydrodynamic focusing of microfluidics with low dc voltage. *Biomedical Microdevices* **12**, 35–40 (2010).

124. Hsi, P. *et al.* Acoustophoretic rapid media exchange and continuous-flow electrotransfection of primary human T cells for applications in automated cellular therapy manufacturing. *Lab on a Chip* **19**, 2978–2992 (2019).

125. Ghassemi, S. *et al.* Rapid manufacturing of non-activated potent CAR T cells. *Nature Biomedical Engineering* **6**, 118–128 (2022).

126. Chamberlain, C. A. *et al.* Highly efficient PD-1-targeted CRISPR-Cas9 for tumor-infiltrating lymphocyte-based adoptive T cell therapy. *Molecular Therapy - Oncolytics* **24**,

417–428 (2022).

127. Rozenbaum, M. *et al.* Gamma-Delta CAR-T Cells Show CAR-Directed and Independent Activity Against Leukemia. *Frontiers in Immunology* **11**, 1–8 (2020).

128. Hulen, T. M., Chamberlain, C. A., Svane, I. M. & Met, Ö. ACT Up TIL Now: The Evolution of Tumor-Infiltrating Lymphocytes in Adoptive Cell Therapy for the Treatment of Solid Tumors. *Immuno* **1**, 194–211 (2021).

129. Bloemberg, D. *et al.* A High-Throughput Method for Characterizing Novel Chimeric Antigen Receptors in Jurkat Cells. *Molecular Therapy - Methods and Clinical Development* **16**, 238–254 (2020).

130. Zhang, Z., Qiu, S., Zhang, X. & Chen, W. Optimized DNA electroporation for primary human T cell engineering. *BMC Biotechnology* **18**, 1–9 (2018).

131. Aksoy, B. A., Aksoy, P., Wyatt, M., Paulos, C. & Hammerbacher, J. Human primary T cells: A practical guide. *PeerJ Preprints* **28**, 1–31 (2018).

132. Madison, A. C. *et al.* Scalable Device for Automated Microbial Electroporation in a Digital Microfluidic Platform. *ACS Synthetic Biology* **6**, 1701–1709 (2017).

133. Shih, S. C. C. *et al.* A Versatile Microfluidic Device for Automating Synthetic Biology. *ACS Synthetic Biology* **4**, 1151–1164 (2015).

134. Im, D. J. *et al.* Digital Microfluidic Approach for Efficient Electroporation with High Productivity: Transgene Expression of Microalgae without Cell Wall Removal. *Analytical Chemistry* **87**, 6592–6599 (2015).

135. Iwai, K. *et al.* Automated flow-based/digital microfluidic platform integrated with onsite electroporation process for multiplex genetic engineering applications. in *2018 IEEE Micro Electro Mechanical Systems (MEMS)* 1229–1232 (IEEE, 2018). doi:10.1109/MEMSYS.2018.8346785

136. Moore, J. A. *et al.* Automated electrotransformation of Escherichia coli on a digital microfluidic platform using bioactivated magnetic beads. *Biomicrofluidics* **11**, 014110 (2017).

137. Miklavčič, D. Handbook of Electroporation. *Handbook of Electroporation* **1**–**4**, 1–2998 (2017).

138. Saulis, G., Lape, R., Pranevičiute, R. & Mickevičius, D. Changes of the solution pH due to exposure by high-voltage electric pulses. *Bioelectrochemistry* **67**, 101–108 (2005).

139. Chicaybam, L. *et al.* An Efficient Electroporation Protocol for the Genetic Modification of Mammalian Cells. *Frontiers in Bioengineering and Biotechnology* **4**, 1–13 (2017).

140. Sherba, J. J. *et al.* The effects of electroporation buffer composition on cell viability and electro-transfection efficiency. *Scientific Reports* **10**, 1–9 (2020).

141. Kim, J. A. *et al.* A novel electroporation method using a capillary and wire-type electrode. *Biosensors and Bioelectronics* **23**, 1353–1360 (2008).

142. Im, D. J. & Jeong, S. N. Transfection of Jurkat T cells by droplet electroporation. *Biochemical Engineering Journal* **122**, 133–140 (2017).

143. Bae, S. J. & Im, D. J. Safe and efficient RNA and DNA introduction into cells using digital electroporation system. *Bioelectrochemistry* **148**, (2022).

144. Gach, P. C. *et al.* A Droplet Microfluidic Platform for Automating Genetic Engineering. *ACS Synthetic Biology* **5**, 426–433 (2016).

145. Gach, P. C., Iwai, K., Kim, P. W., Hillson, N. J. & Singh, A. K. Droplet microfluidics for synthetic biology. *Lab on a Chip* **17**, 3388–3400 (2017).

146. Moazami, E., Perry, J. M., Soffer, G., Husser, M. C. & Shih, S. C. C. Integration of World-to-Chip Interfaces with Digital Microfluidics for Bacterial Transformation and Enzymatic Assays. *Analytical Chemistry* **91**, 5159–5168 (2019).

147. Wang, H. & Chen, L. Novel electrodes for precise and accurate droplet dispensing and splitting in digital microfluidics. *Nanotechnology Reviews* **10**, 857–869 (2021).

148. Perry, J. M., Soffer, G., Jain, R. & Shih, S. C. C. Expanding the limits towards 'one-pot' DNA assembly and transformation on a rapid-prototype microfluidic device. *Lab on a Chip* **21**, 3730–3741 (2021).

149. Sharei, A. *et al.* Ex vivo cytosolic delivery of functional macromolecules to immune cells. *PLoS ONE* **10**, 1–12 (2015).

150. Han, X., Liu, Z., Ma, Y., Zhang, K. & Qin, L. Cas9 Ribonucleoprotein Delivery via Microfluidic Cell-Deformation Chip for Human T-Cell Genome Editing and Immunotherapy. *Advanced Biosystems* **1**, 1–6 (2017).

151. Hur, J. *et al.* Microfluidic cell stretching for highly effective gene delivery into hard-to-transfect primary cells. *ACS Nano* **14**, 15094–15106 (2020).

152. Jayasooriya, V., Ringwelski, B., Dorsam, G. & Nawarathna, D. mRNA-based CAR T-cells manufactured by miniaturized two-step electroporation produce selective cytotoxicity toward target cancer cells. *Lab on a Chip* **21**, 3748–3761 (2021).

153. Szeto, G. L. *et al.* Microfluidic squeezing for intracellular antigen loading in polyclonal B-cells as cellular vaccines. *Scientific Reports* **5**, 1–13 (2015).

154. Li, J. *et al.* Microfluidic-Enabled Intracellular Delivery of Membrane Impermeable Inhibitors to Study Target Engagement in Human Primary Cells. *ACS Chemical Biology* **12**, 2970–2974 (2017).

155. Pollard, J. W., Luqmani, Y., Bateson, A. & Chotai, K. DNA Transformation of Mammalian Cells. *Nucleic Acids* **130**, 321–332 (2003).

156. Lebrun, L. & Junter, G. A. Diffusion of dextran through microporous membrane filters. *Journal of Membrane Science* **88**, 253–261 (1994).

157. Ding, X. *et al.* High-throughput nuclear delivery and rapid expression of DNA via mechanical and electrical cell-membrane disruption. *Nature Biomedical Engineering* **1**, 1–7 (2017).

158. Ayyadevara, V. S. S. A. & Roh, K. H. Calcium enhances polyplex-mediated transfection efficiency of plasmid DNA in Jurkat cells. *Drug Delivery* **27**, 805–815 (2020).

159. Schlake, T., Thess, A., Thran, M. & Jordan, I. mRNA as novel technology for passive immunotherapy. *Cellular and Molecular Life Sciences* **76**, 301–328 (2019).

160. Wang, H., Liu, B. & Wei, J. Beta2-microglobulin(B2M) in cancer immunotherapies: Biological function, resistance and remedy. *Cancer Letters* **517**, 96–104 (2021).

161. Chicaybam, L., Sodre, A. L., Curzio, B. A. & Bonamino, M. H. An Efficient Low Cost Method for Gene Transfer to T Lymphocytes. *PLoS ONE* **8**, 1–11 (2013).

162. Reberšek, M. & Miklavčič, D. Advantages and disadvantages of different concepts of electroporation pulse generation. *Automatika* **52**, 12–19 (2011).

163. Pavlin, M., Flisar, K. & Kandušer, M. The role of electrophoresis in gene electrotransfer. *Journal of Membrane Biology* **236**, 75–79 (2010).

164. Fraietta, J. A. *et al.* Determinants of response and resistance to CD19 chimeric antigen receptor (CAR) T cell therapy of chronic lymphocytic leukemia. *Nature Medicine* **24**, 563–571 (2018).

165. de Macedo Abdo, L. *et al.* Development of CAR-T cell therapy for B-ALL using a point-of-care approach. *OncoImmunology* **9**, (2020).

166. Liu, Y. *et al.* Strategies to enhance CAR-T persistence. *Biomarker Research* **10**, 1–18 (2022).

167. Ghassemi, S. *et al.* Reducing ex vivo culture improves the antileukemic activity of chimeric antigen receptor (CAR) T cells. *Cancer Immunology Research* **6**, 1100–1109 (2018).

168. Min, B., Yamane, H., Hu-Li, J. & Paul, W. E. Spontaneous and Homeostatic Proliferation of CD4 T Cells Are Regulated by Different Mechanisms. *The Journal of Immunology* **174**, 6039–6044 (2005).

169. Ghassemi, S. *et al.* Chimeric Antigen Receptor (CAR) T cells on demand: developing potent CAR T cells in less than 24 hr for adoptive immunotherapy. *Cytotherapy* **22**, S34–S35 (2020).

170. Tu, S. *et al.* Shortening the ex vivo culture of CD19-specific CAR T-cells retains potent efficacy against acute lymphoblastic leukemia without CAR T-cell-related encephalopathy syndrome or severe cytokine release syndrome. *American Journal of Hematology* **94**, E322–E325 (2019).

171. Aftab, B. T. *et al.* Toward "off-the-shelf" allogeneic CAR T cells. *ADVANCES IN CELL AND GENE THERAPY* **3**, e86 (2020).

172. Del Piccolo, N. *et al.* Tumor-on-chip modeling of organ-specific cancer and metastasis. *Advanced Drug Delivery Reviews* **175**, 113798 (2021).